UNIVERSITÀ DEGLI STUDI
DI MODENA E REGGIO EMILIA

PhD Models and methods for material and environmental sciences (M3ES)

Dipartimento di Scienze Chimiche e Geologiche

CYCLE XXXII

CONFINEMENT OF GUEST MOLECULES IN ZEOLITES FOR ADVANCED APPLICATIONS

Tutor
Prof. Maria Giovanna Vezzalini

PhD student
Michelangelo Polisi

Co-tutor
Prof. Rossella Arletti

M3ES Coordinator
Prof. Maria Giovanna Vezzalini

Academic Year 2018-2019

INDEX

ABSTRACT

Ever since the properties of zeolites began to be studied, the scientific research progressively explored new possible application fields for these materials. From the second half of the last century, zeolites have been largely used in petrochemistry and fine chemistry catalysis, natural zeolites have been also used in agronomy or as sorbent for wastewater purification and soil remediation. However, in the last years, thanks to the continuous development of synthesis methods and characterization techniques, the use of zeolites moved toward the so called "advanced applications".

Advanced applications range from the field of energetic to the environmental sciences and biomedical sciences, addressing problems of different nature for which the unique properties of zeolites can be exploited to find new solutions. The particular ability of zeolites to adsorb small molecules inside their cavities, keeping them protected in a confined environment, is the main property which outlines this thesis project, together with the non-ambient conditions characterizing the experimental methodology. The aim of this research is the characterization of hybrid materials formed by zeolites hosting guest molecules within their cavities. In particular the thesis is divided in two main subjects:

- *CO_2 adsorption in Na-X and Na-Y nanosized zeolites*.

This work concerns the *in situ* study of CO_2 adsorption inside FAU zeolite pores. The gas adsorption and storage in porous materials for environmental purposes has been deeply studied in the last years. Many research projects explored the possibility of using zeolites and other porous materials for the CO_2 entrapment, with the aim to reduce the emission of greenhouse gases, which is one of the biggest problems that humanity is facing.

The aim of this work is to shed light on the adsorption properties of nanosized zeolites, exploiting their particular properties for this target. The larger surface area and the higher diffusion capacity exhibited by zeolite nano-crystals motivated the investigation on the CO_2 adsorption mechanism in two nanosized zeolites with faujasite structure, Na-X and Na-Y. The results provided by structural characterization and spectroscopic monitoring indicate a dependence of the physisorption and chemisorption processes on the extraframework (cations and H_2O molecules) amount and distribution in the zeolites porosities.

- *Confinement and condensation of amino acid molecules in Na-mordenite.* The adsorption of amino acids inside the mono-dimensional channel system of a sodium mordenite and the compression of the so-obtained hybrid is the subject of this work. The target is to induce the condensation (polymerization by water elimination) of the amino acids, forming a peptide chain, exploiting the geometrical constraints imposed by the zeolite framework and the mechanical effect of the compression. The hypothesis that in a prebiotic Earth environment, mineral surface had a role in assembly the first organic molecules has been largely studied from the half of the last century. However, the idea that zeolites may catalyze the formation of peptide bonds in abiotic conditions, formulated by J.V. Smith at the end of 90s, was never experimentally tested.

The results obtained by the spectroscopic techniques on the analyzed sample show the formation of peptide bond between amino acid molecules.

In both the topics faced in the thesis, the interaction between the zeolite framework and the guest species is a key factor to understand how these materials are in relation with the environment, from the possibility to form a peptide chain in the very distant past to the storage of greenhouse gases in the future.

To shed light on these processes, a multi-technique approach was adopted to study "*in situ*" the behavior of these materials, mainly using synchrotron X-ray powder diffraction (XRPD) at non-ambient conditions in order to explore their crystal structure and properties. The structural information obtained by X-ray diffraction was coupled with that provided by a number of other spectroscopic and chemical techniques (infrared (IR) spectroscopy, thermal gravimetric analysis (TG), elemental analysis, scanning electron microscopy (SEM), transmission electron microscopy (TEM) and Raman spectroscopy) with the aim to deeply characterize the studied materials and to obtain a wide range of information on them.

RIASSUNTO

Sin da quando le proprietà delle zeoliti hanno iniziato a essere studiate, la ricerca scientifica ha progressivamente esplorato nuovi possibili campi di applicazione per questi materiali. Dalla seconda metà del secolo scorso, le zeoliti sono state ampiamente utilizzate nell'industria petrolchimica e nella catalisi, le zeoliti naturali sono state utilizzate anche in agronomia o come adsorbenti per la depurazione delle acque reflue e la bonifica del suolo. Tuttavia, negli ultimi anni, grazie al continuo sviluppo di metodi di sintesi e tecniche di caratterizzazione, l'uso delle zeoliti si è spostato verso le cosiddette "applicazioni avanzate".

Le applicazioni avanzate spaziano dal campo delle energie a quello ambientale e biomedico, affrontando problemi di diversa natura ai quali è possibile trovare nuove soluzioni sfruttando le proprietà uniche delle zeoliti. La particolare capacità delle zeoliti di adsorbire piccole molecole all'interno delle loro cavità, e mantenerle protette in un ambiente confinato, è la proprietà principale che è alla base di questo progetto di tesi, insieme allo studio in condizioni non ambientali che caratterizzano la metodologia sperimentale utilizzata. Lo scopo di questa ricerca è la sintesi e caratterizzazione di materiali ibridi costituiti da zeoliti che ospitano molecole all'interno delle loro cavità. In particolare, la tesi è divisa in due argomenti principali:

- *Adsorbimento di CO_2 nelle zeoliti nano-fasiche Na-X e Na-Y*. Questo lavoro riguarda lo studio in situ dell'adsorbimento di CO_2 all'interno dei pori zeolitici. L'adsorbimento e lo stoccaggio di gas in materiali porosi a scopo ambientale sono stati ampiamente studiati negli ultimi anni. Molti progetti di ricerca hanno esplorato la possibilità di utilizzare zeoliti e altri materiali porosi per l'intrappolamento di CO_2, con l'obiettivo di ridurre i gas serra, uno dei maggiori problemi che l'umanità sta affrontando. Lo scopo di questo lavoro è far luce sulle proprietà di adsorbimento delle zeoliti nano-fasiche sfruttando le loro particolari proprietà. La più elevata superficie e la maggiore capacità di diffusione mostrata dai nano-cristalli di zeolite hanno motivato lo studio del meccanismo di adsorbimento di CO_2 in due nano-fasi zeolitiche con struttura tipo faujasite, Na-X e Na-Y. I risultati forniti dalla caratterizzazione strutturale e dal monitoraggio spettroscopico indicano una dipendenza dei processi di adsorbimento fisico e chimico dalla quantità e distribuzione delle specie extraframework (cationi e molecole d'acqua).
- *Confinamento e condensazione di molecole di amminoacidi nella Na-mordenite*. L'adsorbimento degli amminoacidi all'interno del sistema di canali monodimensionale di una

mordenite di sodio, e la compressione dell'ibrido così ottenuto, sono l’oggetto di questo studio. L'obiettivo è quello di indurre la condensazione (polimerizzazione per eliminazione d’acqua) degli amminoacidi, formando una catena peptidica, sfruttando i vincoli geometrici imposti dalla struttura della zeolite e l'effetto meccanico indotto dalla pressione. L'ipotesi che in un ambiente prebiotico terrestre, la superficie dei minerali abbia avuto un ruolo nell'assemblaggio delle prime molecole organiche è stata ampiamente studiata dalla metà del secolo scorso. Tuttavia, l'idea che le zeoliti possano catalizzare la formazione di legami peptidici in condizioni abiotiche, formulata da J.V. Smith alla fine degli anni '90, non è mai stata testata sperimentalmente. I risultati ottenuti da studi spettroscopici sui campioni ibridi mostrano la formazione del legame peptidico tra molecole di amminoacidi.

In entrambi gli argomenti affrontati in questa tesi, l'interazione tra la struttura della zeolite e le specie ospiti è un fattore chiave per comprendere come questi materiali siano in relazione con l'ambiente, dalla possibilità di formare una catena peptidica in un passato lontano allo stoccaggio di gas serra nel futuro.

Per far luce su questi processi, è stato adottato un approccio multi-analitico per studiare "in situ" il comportamento di questi materiali, principalmente utilizzando la diffrazione di raggi X da polvere (XRPD), usando luce di sincrotrone in condizioni non ambientali, al fine di indagare la loro struttura cristallina e le loro proprietà. Le informazioni strutturali ottenute dalla diffrazione di raggi X sono state implementate da quelle fornite da una serie di tecniche spettroscopiche e chimiche (spettroscopia infrarossa (IR), analisi termo-gravimetrica (TG), analisi elementare, microscopia elettronica a scansione (SEM), microscopia elettronica a trasmissione (TEM) e spettroscopia Raman) con l'obiettivo di caratterizzare in modo completo i materiali studiati e ottenere una vasta gamma di informazioni su di essi.

1 INTRODUCTION

1.1 Zeolites

In 1756, the mineralogist A. F. Cronstedt observed a particular behavior of a mineral, which released vapor when heated. Based on this, he coined the term "zeolite" (from the Greek words ζέω = to boil and λίθος = rock; that is, boiling stones). From that moment, zeolites remained a curiosity for scientists and collectors until the first half of 20th century, when their unique physicochemical properties attracted the attention of many researcher (Gottardi and Galli, 1985). Several authors have contributed over time to give a definition of zeolite (Meier and Olson, 1978; Liebau, 1983; Smith, 1984), as long as the International Mineral Association, Commission on New Minerals and Mineral Names (IMA CNMMN) (Coombs *et al.*, 1997) gave the following one: *"A zeolite mineral is a crystalline substance with a structure characterized by a framework of linked tetrahedra, each consisting of four O atoms surrounding a cation. This framework contains open cavities in the form of channels and cages. These are usually occupied by H_2O molecules and extra-framework cations that are commonly exchangeable. The channels are large enough to allow the passage of guest species. In the hydrated phases, dehydration occurs at temperatures mostly below 400 °C and is largely reversible. The framework may be interrupted by (OH, F) groups; these occupy a tetrahedron apex that is not shared with adjacent tetrahedra".*

This definition does not put constraints on the chemical composition of these materials and allows to consider zeolites both natural and synthetic phases as long as they are characterized by an open three-dimensional scaffold (framework) formed by tetrahedra TO_4, called PBU (primary building units).

Generally, in 3D framework silicates, the tetrahedral cations are mainly Si, and these SiO_4 units are linked together so that oxygens are shared by two tetrahedra, resulting in a sharing coefficient of 2. The number of theoretical nets achievable combining the tetrahedral PBU's is infinite. However, in all the silicate frameworks, the tetrahedra form quite a small number of complex structural units (rings, cages, chains) of low potential energy, called secondary building units (SBU's, fig.1). These SBU's contain up to 16 T-atoms, are invariably non-chiral and a unit cell always contains an integer number of them (Baerlocher *et al.*, 2007).

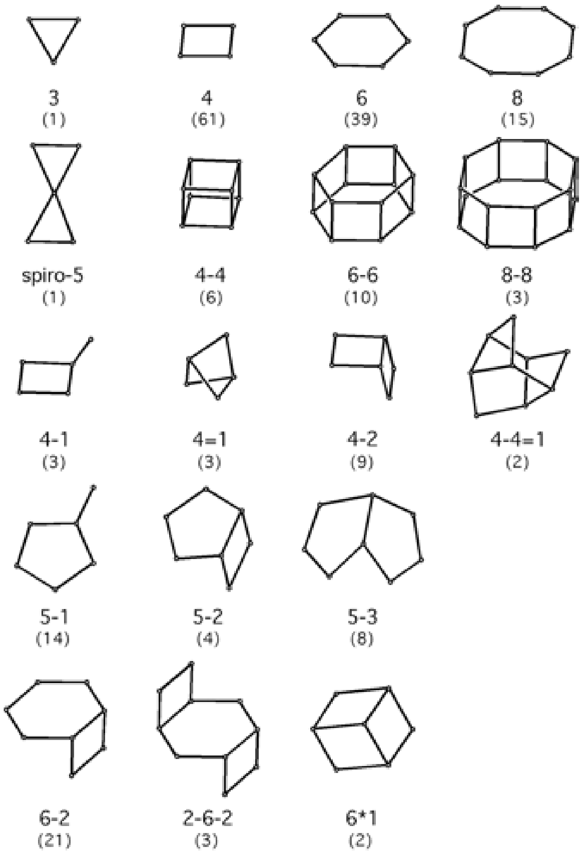

Figure 1: Secondary building units and their symbols. Number in parenthesis = frequency of occurrence (image from: Baerlocher *et al.*, 2007).

All zeolite frameworks may be described as different ways of connecting these SBU's. All the existing combinations give rise to different structural types, called framework types.

The framework types are, at present, 234 and represent the highest possible symmetry (topological symmetry) assumed by a zeolite. Each framework type is distinguished by a code of three capital letters and are all listed in the Atlas of Zeolite structure type (Baerlocher *et al.*, 2007). Beyond the cited SBU's, it is noteworthy to mention the composite building units (CBU's), as double 6-ring, cancrinite cage, alpha cavity, beta cage, double crankshaft chain, etc. present in several zeolites, that can be useful in identifying the relationships between different framework types.

As underlined in the previous definition, the main feature of zeolites is the presence, inside the framework, of large cavities interconnected. These can be ideally infinite (channels) or closed (cages). Based on this, the simplest criterion that distinguishes the zeolites (and zeolite-like materials) from denser tectosilicates is the framework density (FD), which is defined as the number of tetrahedrally coordinated framework atoms (T-atoms) per 1000 Å^3. The maximum FD for a zeolite ranges from 19 to over 21 T-atoms per 1000 Å^3, depending on the type of smallest ring present, whereas the minimum for denser structures ranges from 20 to 22 (Brunner and Meier, 1989).

The zeolite structures can be described and classified on the basis of their channel systems, which can be one-, two- or three-dimensional, depending if the channels develop in one or more crystallographic directions. Different channels may be interconnected or not. The number of tetrahedra forming the channel apertures controls the molecule diffusion along the channels and defines their crystallographic free diameters.

1.2 Crystal-chemistry of zeolites

The following idealized general formula has been proposed by Smith (1963) for natural zeolites:

$$(M_x, D_y)\ [Al_{(x+2y)}\ Si_{n-(x+2y)}\ O_{2n}] * mH_2O$$

M represents monovalent cations with stoichiometry x, and D represent divalent cations with stoichiometry y. Cations inside the first parentheses are the exchangeable cations. Those within the square brackets are the tetrahedral cations, forming the framework structure with the oxygens. The value of m gives the number of H_2O molecules adsorbed within the pores.

The general formula of a zeolite permits a large chemical variability, the only constraint being the Löwenstein’s rule. This rule imposes a lower limit on the Si/Al ratio, which is 1, due to the forbidden Al-O-Al bond in the framework. However, a work of Fletcher *et al.* (2017) provides evidence for non-Löwensteinian ordering in protonated zeolite frameworks in rare cases. Very few zeolites have the minimum Si/Al ratio of 1 allowed by Löwenstein’s rule (i.e. gismondine, willhendersonite, partheite). The highest Si/Al ratio discovered in a natural zeolite is 7.6 in mutinaite, while pure silica synthetic phases can be produced in lab. In addition to the Löwenstein’s rule, also the Dempsey’s rule defines the Si and Al ordering (Dempsey *et al.,* 1969; Melchior *et al.,* 1981) suggesting that the presence of Al-O-Si-O-Al bonds in the framework should be minimized, since Al atoms should be far as possible each other.

The framework negative charge due to the Si/Al substitution is compensated by the extraframework cations (Ca^{2+}, Mg^{2+}, Ba^{2+}, K^+, Na^+ most common cations in natural zeolites), which can be bonded to the framework oxygens and/or to the H_2O molecules. Concerning the water content, it can vary for each zeolite species. The average H_2O content is known to be related to both structural and chemical parameters because it increases with the increasing void volume/total volume, Si/Al, and divalent/monovalent cation ratios (Passaglia and Sheppard, 2001), but also environmental conditions can influence this value.

1.3 Genesis of natural zeolites

Natural zeolites can originate from different precursor materials, including volcanic and impact glasses, aluminosilicate minerals including other zeolites, feldspar, feldspathoid, kaolinite and smectite. Among these, volcanic glass is the major precursor, it reacts to form zeolites by a dissolution-precipitation process in which a gel-like material is an intermediate phase (Hay and Sheppard, 2001). Generally, zeolites may have diagenetic or hydrothermal genesis.

Diagenesis is the crystallization of a mineral by alteration (secondary transformation) of the preexisting components of a sediment; diagenesis is generally thought as a low-temperature process, where "low" means "less than 200 °C" (Gottardi, 1989). Two kinds of diagenesis must be distinguished: above the water table (may occur in soils, in hydrologically open systems or closed systems, and in geo-autoclaves), and below the water table (may occur in marine sediments and as burial diagenesis with a continuous transition to very low-grade metamorphism).

In hydrothermal genesis, the crystallization occurs from hot aqueous solutions of magmatic origin. Crystals are formed in fractures and cavities of igneous rocks by these liquids when, going up toward the surface, the pressure and temperature conditions allow the crystal nucleation.

1.4 Zeolites synthesis

The two scientists who can be regarded as the founders of zeolites synthesis science and practice are Richard M. Barrer and Robert M. Milton. After the first synthesis of zeolite in 1948, in few years they produced more than 20 lab-made zeolites. The 1950s decade saw many significant developments, both as new discoveries (i.e. introduction of quaternary ammonium cations as templating agents) and also in the research aimed at understanding the synthesis process (Cundy and Cox, 2003). These studies have continued up to the present day, devoted at the discoveries of new materials, advance in synthesis techniques, innovation in theoretical modelling methods and development of new strategies for investigation of reaction mechanisms and characterization of the products (Cundy and Cox, 2005).

The synthesis of zeolites is performed in batch systems, where silicate and aluminate (or phosphate) solutions are mixed and then exposed to hydrothermal conditions with temperature between 30 and 200 °C, for times varying from minutes to days. The zeolite synthesis involves mixing of raw materials in order to obtain a precursor mixture (colloidal suspension or dense gel) that may be aged before hydrothermal treatment to produce the crystalline zeolite. The silicate and alumina suspension can be completely or partially dissolved during this process. The reaction composition used to express the precursor mixture is usually written as the molar ratios of the oxide components: $M_2O:R_2O:TO_2:H_2O$. In which T represent the framework atoms: Si, Al, P, B, Fe, Ga, Ti etc.; M is alkali metal (Na, K, Li, Rb, Cs etc.); R is the organic structure directing agent (or template) used to stabilize the zeolite framework and to determine the size and morphology of zeolites (quaternary ammonium compounds are typically used); H_2O represents the solvent, generally water is used, but other solvents such as alcohols, diols, and ammonia are used too. Water is also used as a space filler, accelerator of chemical reactions, hydrolyser of chemical reagents. The crystallization of zeolites generally proceeds via two steps: the first one is the nucleation of discrete particles, “crystal nuclei”, having the identity of the new crystalline phase, are formed. The second step is the growth of zeolite crystals. Even when the reaction mixture is stable, a large number of variables can influence the zeolite crystallization, most important are the synthesis temperature and the crystallization time. Type of raw materials (purities, reactivity), agitation, order of mixing, and aging have a significant effect too (Cundy, 2005; Grand *et al.,* 2016).

1.5 Properties of the zeolites

Because of their peculiar crystal-chemistry features, the zeolites have the following chemical-physical properties:

- cation exchange
- reversible dehydration

- adsorption capacity and molecular sieving
- catalytic properties

1.5.1 Cation exchange

As discussed in chapter 1.2 *(crystal-chemistry of zeolites)*, the negative charged framework of zeolites is compensated by the presence of cations within the cavities. These monovalent or divalent cations are only loosely held in the anionic framework and, to a first approximation, can be exchanged or removed easily by washing the zeolite with a concentrated solution of other cations (Pabalan and Bertetti, 2001). Generally, the ion-exchange behavior of a particular zeolite depends on different factors, including: 1) the framework topology, which determines the channels dimension and configuration; 2) ion size and shape (polarizability); 3) ion charge; 4) charge density of the anionic framework; 5) concentration of the ion solution (Barrer, 1978). Many zeolites contain more crystallographic distinct sets of sites that can be occupied by exchangeable cations, and each site may exhibit different selectivity and ion-exchange behavior.

Although every zeolite has its own thermodynamic affinity for particular metal ions, overall, zeolites have particular affinity for cations with low solvation energy: alkaline, alkaline-heart elements and NH_4^+. Figure 1.1 shows the cation exchange concept.

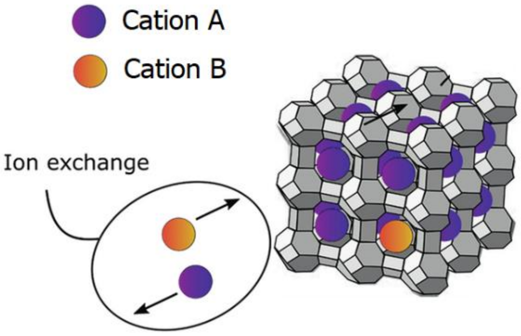

Figure 1.1: Ion exchange in zeolite (image modified from: https://www.researchgate.net/figure/Ion-exchange-mechanism-in-antimicrobial-zeolites-loaded-with-silver-ions_fig13_318156604).

1.5.2 Reversible dehydration

The open framework exhibited by zeolites hosts variable amounts of extraframework cations and H_2O molecules. The H_2O content can be very different depending on the crystal-chemistry features of the zeolite; hydrophobic samples as pure-silica zeolites may contain 3-4% of water, while hydrophilic zeolites may also contain more than 20% of water.

Normally, at ambient conditions, the zeolites (framework, exchangeable cations and H_2O) are in equilibrium with the external environment, but several coupled changes occur in H_2O content and structure whenever a zeolite is subjected to a change in environment (Bish and Carey, 2001; Cruciani, 2006). H_2O molecules physisorbed within the pores can be completely removed increasing the temperature or decreasing the pressure. The temperature range in which the complete dehydration occurs changes depending on the zeolite, generally, the water adsorbed on the external surface of crystals is released below 150 °C, while the H_2O within channels is removed at higher temperature. The rehydration process occurs once the dehydrated zeolite is exposed to environmental conditions, adsorbing H_2O from ambient humidity. During rehydration, in many cases appears a distinct hysteresis effect and, depending on the zeolite species and the temperature reached, it may take a significant time before rehydration reaches a maximum. Complete rehydration typically occurs when heating has not exceeded moderate temperature as 250 °C (Van Reeuwijk, 1974). Higher temperature may cause reduced rehydration capability as reported by Pécsi-Donáth (1968).

1.5.3 Adsorption capacity and molecular sieving

As reported in the previous paragraph, zeolites can adsorb molecules like H_2O within their pores. The term “adsorption” is used to indicate a surface process, in which atoms and molecules can interact in different ways and different strength to a substrate. The walls of zeolite channels and cages act as an internal surface, in which small molecules can be captured and weakly bonded to the framework. The adsorption capacity is strongly influenced by the chemical composition and in particular by the Si/Al ratio which determines the hydrophobicity (high Si/Al ratio) or the hydrophilicity (low Si/Al ratio) of the zeolite. As reported in literature (Anderson, 2000; Martucci *et al.*, 2012) hydrophobic zeolites show an organophilic behavior. Among parameters influencing adsorption capacity, the acidity of the zeolite and the type of exchangeable cations are important, but this phenomenon is particularly dependent on the pore systems dimension. The size of the channels and cages can discriminate which molecules can enter within the pores on the basis of the dimension. In this way zeolites can perform selective adsorption from a mixture or can act as “molecular sieves” and let transit through the channel only molecules with the right shape and dimension.

1.5.4 Catalytic properties

Synthetic zeolites are largely used as catalysts in oil refining and petrochemical industry thanks to the presence of catalytic sites, in particular acid sites, within their cavities (Vermeiren and Gilson, 2009). The negative charge induced by the tetrahedral Al^{3+} in the zeolite framework, can be balanced also by H^+ or by the lack of oxygen atoms.

In the case of a proton compensating the charge, this hydroxyl group is called Brønsted acid site, while the lack of the oxygen atom give rise to a Lewis acid site (Fig.1.2).

Brønsted acid sites are fundamental for the fluid cracking of gas oil, acting via protolytic cracking. (Corma *et al.,* 1985; Rajagopalan *et al.,* 1986). Although the number of acid sites could be related to the Si/Al ratio, the higher aluminum content does not correspond to the higher cracking activity, since the catalytic cracking not only needs acid sites, but acid sites strong enough to produce the adequate C-C bond polarization (Corma, 1989). The strength of the acid sites is generally related to the Si/Al ratio and to the chemical composition and structure of the surroundings of a given Al atom.

The cracking occurs also by initiation via carbenium ions, which has been related to the presence of Lewis acid sites, inducing β-scission mechanism, generally with a higher activation energy compared to the protolytic cracking (Corma, 1989).

In order to prepare catalytically active zeolites, it is necessary to exchange the zeolite with NH_4^+ and to thermally treat it at 550 °C. In this way ammonia is removed from the structure leaving protons inside.

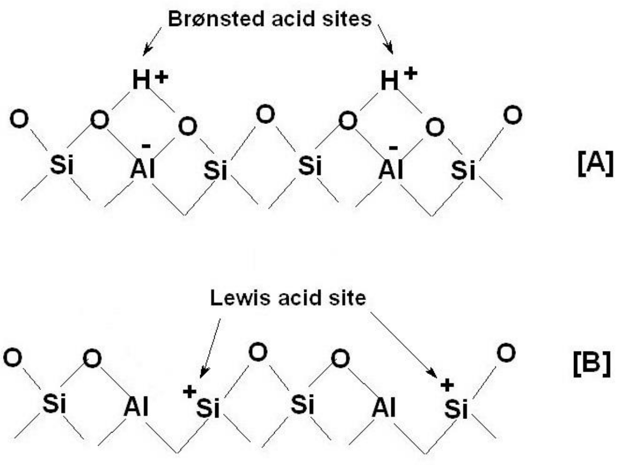

Figure 1.2: Schematic representation of the surface of a zeolite channel with Brønsted (A) and Lewis (B) acid sites.

1.6 Applications of zeolites

Because of their particular properties, thanks to the geographically widespread abundance of natural zeolites and the possibility to tune and optimize the features of synthetic zeolites, these materials have generated strong interest for use in a broad range of applications. In this chapter the applications of zeolites are divided in two groups: "traditional applications" - fields in which zeolites have been widely and commonly used from the second half of the last century- and "advanced application" - in the energetic, biological, medical, environmental areas, in which the possible use of zeolite has been explored in the last years.

1.6.1 "Traditional" applications

The different applications of natural and synthetic phases drive the world market of zeolites. Starting from the natural zeolites, the worldwide mine production of natural zeolites (mainly chabazite and clinoptilolite) in 2018 is estimated to be $1.1 \cdot 10^6$ metric tons (Flanagan, 2019). Natural zeolites are largely employed, in terms of tonnage, in the construction industry where zeolitic tuffs are used for preparation of dimension stones, or as additive in pozzolanic material and cements (Colella *et al.*, 2001). Other applications concern the agriculture, where the properties of zeolites are used as soil amendments, in soil management, horticulture, aquaculture, storage pest management, environmental control, animal feeding etc. (Di Renzo and Fajula, 2005; Eroglu *et al.,* 2017).

Both natural and synthetic zeolites are used as effective adsorbents in water and wastewater treatment. In fact, with the fast development of industries, a huge quantity of wastewater has been produced from industrial processes and has been discharged into soils and water systems. Wastewater usually contains pollutants such as cationic and anionic ions, oil and volatile organic compounds, which have poisonous and toxic effects on ecosystems. Adsorption capacity and cation exchange properties of zeolites make these materials suitable for contaminants removal from water (Kalló, 2001; Meteš *et al.,* 2004; Wang and Peng, 2010). Moreover, zeolites have been used for nuclear waste treatment, thanks to the high selectivity, exhibited by various zeolites, toward several key radionuclide as ^{137}Cs, ^{60}Co, ^{90}Sr, ^{110m}Ag (Dyer and Keir, 1984; Osmanlioglu, 2006).

Cation exchange property of zeolites has been exploited in detergent industry, where synthetic zeolites are used as water softeners, preventing carbonate precipitation from wash water by extracting Ca^{2+} and Mg^{2+} cations and releasing Na^+ (Townsend and Coker, 2001).

Most of the current large-scale commercial processes involving synthetic zeolites is linked to the exploiting of their catalytic properties in the petrochemical industry for petroleum refining. The catalytic properties of zeolites gave to these materials a huge technological and economic impact on this sector of activity (Lercher and Jentys, 2002; Corma and Martínez, 2002). Zeolite catalyst consumption is dominated by far by zeolite Y for fluid catalytic cracking (FCC) application (Blauwhoff *et al.*, 1999; Di Renzo and Fajula, 2005). In the field of fine chemicals and organic industrial syntheses the catalytic properties of zeolites are deeply exploited (Čejka, 2012). Separation and purification of gas mixtures by selective adsorption is a very common practice in different industrial fields. Zeolitic adsorbents, thanks to their “molecular sieves” character, played a major role in the development of adsorption technology. The major areas of applications are: removal of trace or dilute impurities from a gas, separation of bulk gas mixtures and gas chromatography analysis (Sircar and Myers, 2003).

1.6.2 "Advanced" applications

The new applications of zeolites, listed in this paragraph, often exploit the unique spatial structuring of the zeolite channel system for novel concepts, such as the stabilization of nanoscale forms of matter, separation of reaction spaces in electron transfer processes, or size-selective chemical sensing, etc. (Bein and Mintova, 2005; Gilson *et al.,* 2011). New insights on the re-organization of intruded molecules in zeolite hosts promoted by pressure, have been demonstrated in recent years and fascinating discoveries with potential technological implications have been reported by several authors (Richard *et al.*, 2016; Santoro *et al.*, 2016; Arletti *et al.*, 2017; Gatta *et al.*, 2018).

Gas storage: Zeolites have been used for gas separation and purification in industrial processes, but the ability of zeolites to adsorb and store within their cavities different types of gases can be useful in different fields as: energy-related applications, medical applications and environmental applications (Bein and Mintova, 2005; Morris and Wheatley, 2008).

Concerning the gas storage for energy applications, the hydrogen storage in porous materials has attracted considerable attention, as a consequence of the role of H_2 for its possible use as a substitute of fossil fuel. The physisorption of H_2 on zeolites can be an efficient solution to store and transport H_2 safely and economically (Morris and Wheatley, 2008).

The capacity of zeolites to store and slowly release the gas in a biological system, coupled with the very low toxicity showed by nanosized zeolite particles has been recently exploited in several medical applications (Mintova *et al.,* 2013; Georgieva *et al.,* 2016).

In the context of environmental remediation, the zeolites can remove the gas from the environment for a very long time, preventing the environmental effects of the gas becoming a problem. Greenhouse gases, like CO_2, are clearly of most interest, but other toxic gases such as sulfur dioxide and ammonia also have an important impact on the environment (Siriwardane *et al.*, 2001; Morris and Wheatley, 2008). This problem is widely discussed in Chapter 4.

Medical and biomedical applications: The diverse and highly controlled properties of zeolites, make them interesting candidates for a variety of further biological and medical applications (Bacakova *et al.*, 2018). Specifically, the use of synthetic zeolites has been tested in: 1) regeneration of artificial dialysis solutions (Cheah *et al.,* 2017) and fabrication of zeolite-based material for artificial kidney application (Lu *et al.,* 2015); 2) immobilization of contrast agents (as Gd^{3+}) for magnetic resonance imaging (Platas-Iglesias *et al.,* 2002); 3) chromatographic carrier and protein stabilization while removing from biological structural matrix (Chiku *et al.,* 2003; Sakaguchi *et al.,* 2005); 4) supports for enzyme immobilization, including Penicillin G acylase (Corma and Fornes, 2002); 5) adsorbents for perfluorocarbons (PFC) applied in the treatment of respiratory diseases (Proquitté et al., 2004); 6) binding agents for toxic compounds, antioxidants and used as mineral additive in various dietary strategies (Galvano *et al*., 2001); 7) as controlled-release delivery vehicle for anti-inflammatory drugs in human body (Rimoli *et al.,* 2008; Khodaverdi *et al.,* 2014); 8) construction of biosensors and systems for harvesting and detecting biomarkers of serious disease, particularly tumors (Greco *et al.,* 2015; Soldatkin *et al.,* 2015); 9) zeolites as hemostatic agents (Pourshahrestani *et al.,* 2016).

Energy storage in zeolites: Promising technologies about mechanical energy absorption, storage, and generation is based on forced penetration of a nonwetting liquid in hydrophobic porous solids. The energy of applied pressure can be converted into the energy of the solid−liquid interface. Pure-silica zeolites (zeosils) have been largely studied for this kind of application during the last years, due to the presence of highly hydrophobic micropores with very small openings; these materials demonstrate high energetic performance under intrusion of water and electrolytic solutions (Eroshenko *et al.,* 2001; Popyk and Eroshenko, 2014; Confalonieri *et al.,* 2018).

Concerning the energy storage and transfer in zeolites, organic/inorganic hybrid materials as zeolites + dyes are currently used in area of sustainable energy technologies. The excellent optical properties and chemical stability of these composites make them key components of artificial antenna systems, sensors, light emitting and bio-nano devices (Calzaferri, 2012; Lülf *et al.,* 2013). These materials formed by the encapsulation of dye molecules in mono-dimensional channel systems of zeolites can harvest and transmit the light energy through the FRET (Forster Resonance Energy Transfer) process (Calzaferri and Lutkouskaya, 2008).

Sensors and optics: New routes -through high pressure- for molecules polymerization were explored, using the nanoconfinement provided by zeolite pores to induce the reaction. Materials formed by conducting polymers (such as polyacetylene) confined within zeolite channels were synthesized catalyzing the polymerization reaction through pressure. In this way polymers, not chemically stable otherwise, would be well protected in the zeolite matrices (Santoro *et al.,*

2013). Emerging applications of these materials, once properly functionalized, are in sight in diverse fields such as nano-electronics, nano-sensoring and nano-photonics (Davis, 2002).
In last years, molecular sieves have found new uses as hosts for the preparation of small metal- and semiconductor clusters that can be grown in confined zeolite spaces and are used in photo-catalysis, sensors, flat panel displays, non-linear optics, etc. (Zhai *et al.*, 2000). The importance of small metal clusters in catalysis and in many advanced applications is due to the significant physical changes that occur when reducing the size of a material down to a few nanometers, these systems often display unique nano-chemical and nano-physical properties allowing the formation of nanoscopic magnets, spatially ordered nanostructures, nano-electronic devices, quantum electronics, etc. (Bein and Mintova, 2005).

Besides all the already listed applications, many others possible uses of zeolites are currently studied. Biomass processing, processing of syngas derived products and direct conversion of alkanes are just few of the chemical applications exploiting zeolites (Gilson *et al.*, 2011). Moreover, zeolite-based hybrid materials, zeolite films, layers and membranes are used in electrochemistry, as dielectric layers for semiconductor applications, in optical applications and acoustic devices.

2 AIMS OF THE THESIS

The aim of this PhD thesis is to induce and to understand possible reactions occurring in the micropores of zeolites, to be exploited in environmental and technological applications. The first question that need be answered to target our goal is: how do guest molecules behave in the confined environment of zeolite pores under the requested conditions?

In fact, only recently, particular interest has been devoted to the structural study of the reactions occurring among the guest species adsorbed within the cavities of these microporous materials, rather than to the behavior of the bare framework. It has been in fact demonstrated that zeolites can be considered as nanoreactors, and/or as “molds” and that can be exploited for several applications already described in the previous chapter. The continuous technological improvement and development of the characterization techniques in material sciences is giving the possibility to modify the sample environment during *in situ* measurements and is opening new perspectives in these studies.

To pursue our objectives, and to increase the knowledge of the reactions occurring in confined environment, two systems have been studied: i) nanosized zeolites for CO_2 adsorption and ii) 1D zeolites for condensation of amino acid molecules.

In the first system (Chapter 4) carbon dioxide adsorption/desorption has been followed in situ in two zeolite nanocrystals with faujasite structure, with the aim to investigate the possibility of CO_2 storage in these porous materials. In the second one (Chapter 5) the amino acid adsorption and condensation has been tentatively induced under pressure in the mono-dimensional channel system of mordenite zeolite to form a peptide chain.

In light of this, the thesis aims to enrich the knowledge on how the geometrical restriction imposed by zeolite frameworks, combined with non-ambient conditions, can affect the behavior and the reactivity of the guest molecules. Both the systems studied well rank in the environmental topic at the cutting edge of the scientific Green Chemistry research, since the results can be exploited to find alternative path to obtain useful chemical reactions and for CO_2 captures.

3 EXPERIMENTAL METHODS

3.1 Synchrotron X-ray powder diffraction

As well as all crystalline materials, also zeolite have been largely characterized by X-ray diffraction techniques. The X-ray diffraction data of zeolite allowed to determine, in the last decades, the crystal structures of these materials. One of the biggest problems in the study of lab-made materials, as synthetic zeolites, is the difficulty of synthesizing a single crystal of sufficient size and quality to allow the structural characterization by single crystal X-ray diffraction. The development of applications of X-ray powder diffraction (XRPD), as the use of synchrotron radiation, had a strong impact on the structural characterization of zeolites.

Synchrotron radiation facilities are today spread all over the world. In these large-scale laboratories, electrons or other charged particles, moving at relativistic speed in a storage ring, are forced by magnetic fields to follow curved trajectories, in this way they emit electromagnetic radiation in the direction of their motion, known as synchrotron radiation (Balerna and Mobilio, 2015). The production of this radiation is given by the presence, in the storage ring path, of bending magnets, or more sophisticate insertion devices formed by periodic magnets (wigglers and undulators), able to deflect the electron beam, producing a narrow and collimated radiation beam.

The particular properties of the synchrotron radiation allow to obtain results inaccessible with conventional X-ray sources. The beam properties are: high intensity, very broad and continuous spectral range from infrared up to the hard X-ray region, high degree of polarization, high brightness of the source due to small cross section of the electron beam and high degree of collimation. Moreover, the synchrotron laboratories allow to perform a large series of in situ experiments at non-ambient conditions, treated in more detail in paragraph 3.1.1.

The storage ring where the electromagnetic radiation is generated has many ports, each of them opening onto a beamline. Here scientists set up their experiments and collect data. Beamlines are built tangentially to the electron beam orbit of the storage ring and capture radiation emitted from insertion devices or bending magnets, tuning it to the desired wavelength. Each beamline has an optical section and an experimental station, monitored by an external control room (Figure 3.1).

All the data reported in this thesis were collected in different beamlines, all of them located at ESRF (European Synchrotron Radiation Facility) in Grenoble (France), figure 3.2. The beamlines descripted in the next paragraphs, are: ID22, ID15 and ID27.

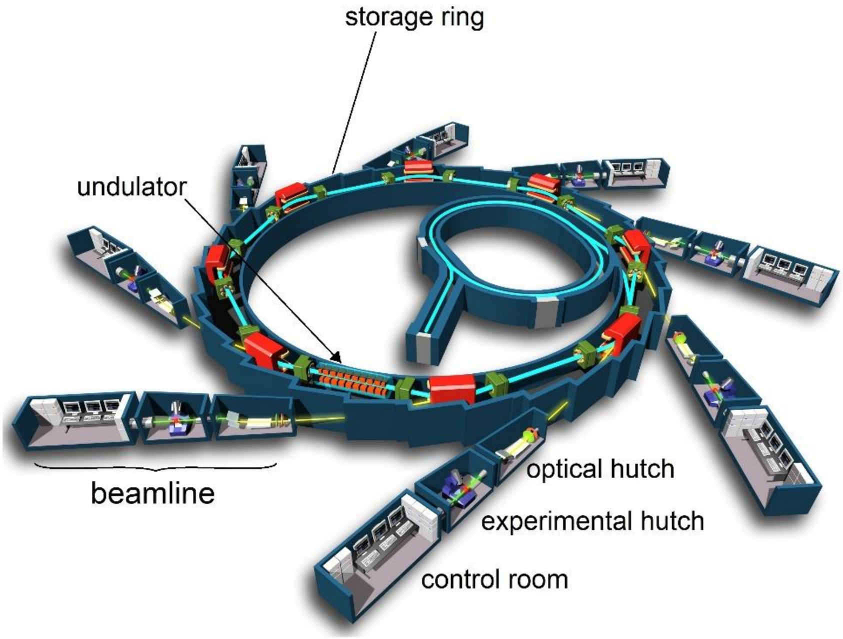

Figure 3.1: Synchrotron structure scheme

Figure 3.2: ESRF, Grenoble.

3.1.1 In situ X-ray diffraction at non-ambient conditions

Among the advantages given by non-conventional radiation sources as synchrotron facilities, one of the most important is the possibility to perform experiments in non-ambient conditions, as high temperature, high pressure, during gas adsorption etc.

On ID22 beamline, a hot air blower allows to heat the sample stage while the X-ray beam is on. In this way it is possible to carry out in situ X-ray diffraction collections during the sample heating, studying processes (i.e. zeolite dehydration) in a certain temperature range. This device was used to dehydrate the Na-X and Na-Y samples before the CO_2 adsorption experiment. In the same beamline, ID22, a gas-rig, connected to the capillary containing the powder sample, allowed to send and to pump gas through a wire system. Different kinds of gases can be used connecting different gas bottles to this device.

In addition, this beamline is equipped with a high-resolution detector (Figure 3.3), in which nine analyzer crystals are mounted on a single rotation stage. The beamline hutch and the mentioned instruments are shown in figure 3.4.

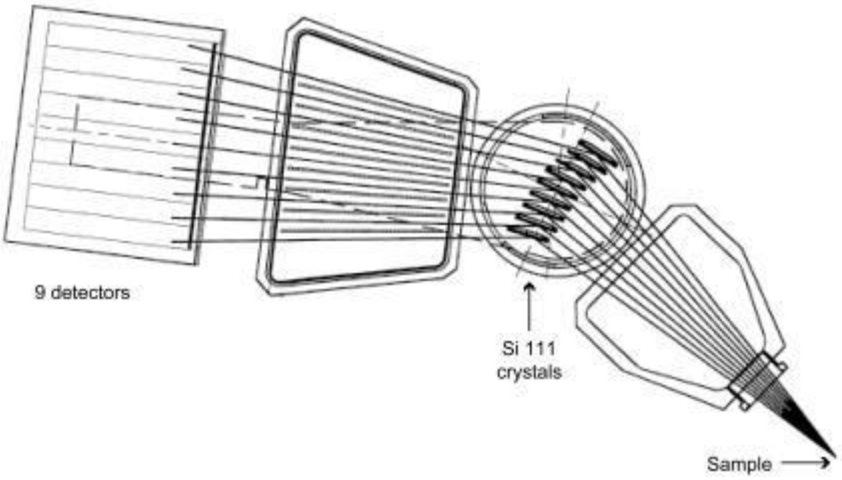

Figure 3.3: Scheme of the high-resolution multianalyzer detector at ID22 beamline.

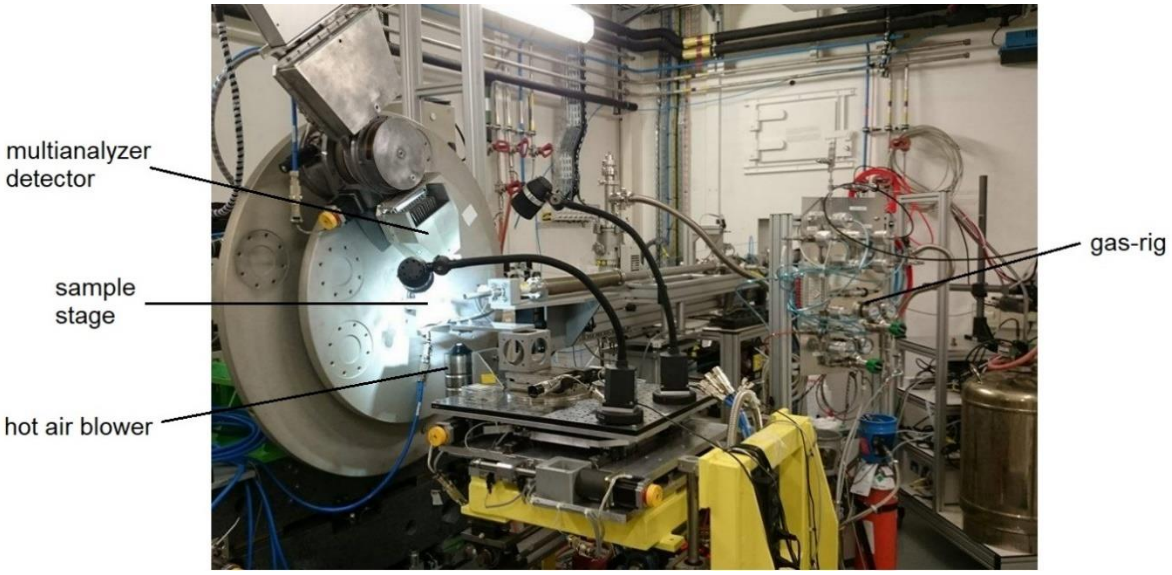

Figure 3.4: ID22 beamline experimental hutch (ESRF, Grenoble).

The in situ high pressure experiments were performed at ID27 beamline. To exercise a hydrostatic pressure, a diamond anvil cell (DAC) was used. In this high-pressure device, the analyzed sample is located between tiny flat faces ground on the pointy ends of two diamonds (cutlet faces). More in detail, the sample is confined in a hole of a metal disk called “gasket” (usually made of stainless steel or rhenium), together with a fluid that transmits the pressure in hydrostatic way once compressed by the two diamonds. The role of the gasket is to laterally confine the liquid and the powder sample, avoiding leaks when the pressure is applied. The scheme of a diamond anvil cell is shown in figure 3.5a, and a picture of the gasket between the two diamonds in figure 3.5b.

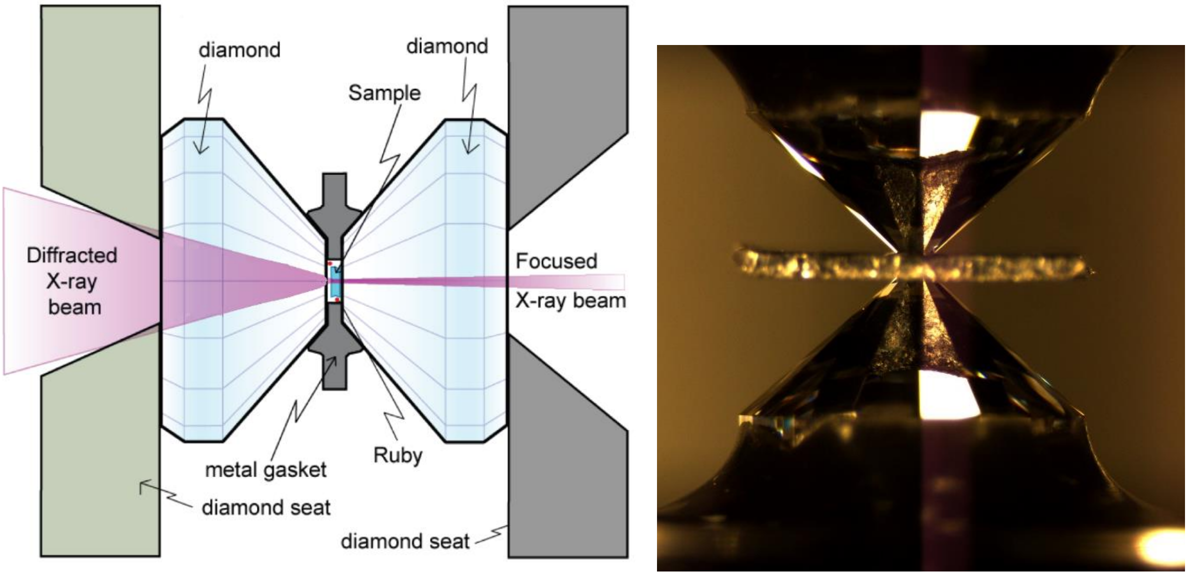

Figure 3.5a (left): Scheme of a diamond anvil cell. 3.5b (right): Diamonds and gasket in a diamond anvil cell.

A modest force applied across the wide face of the diamond can generate high pressure in the confined environment between the two small "cutlet" faces. Different types of diamond anvil cell can move closer the diamonds in mechanical way through screws or thanks to a gas membrane. The medium used to transmit the pressure to the sample is called “pressure transmitting medium” (PTM) and can be liquid, or sometimes solid. Different types of PTM can reach different values of pressure, remaining in a hydrostatic regime (Klotz *et al*., 2009). In the case of zeolite study, the used pressure transmitting media can be distinguished in two type depending on the dimension of the molecules (or atoms) constituting the medium. If the molecules of the medium are smaller than the dimension of the zeolite apertures, they can penetrate the pores and the medium is considered nominally “a penetrating PTM”. In the case that the dimension of the molecules exceeds the diameter of the zeolite pores the medium is called “a non-penetrating PTM”.

Because of no correlation exists between the force applied on the diamonds and the pressure inside the DAC, the presence of pressure calibrants inside the gasket together with the sample allows to measure the pressure during compression. The most common pressure calibrant is ruby, whose fluorescence changes with the pressure. As reported by Forman *et al*. (1972); Barnett *et al.* (1973), two characteristic radiations emitted by Cr^{3+} doped α-Al_2O_3 change frequency on a nonlinear hydrostatic scale when the crystal is under pressure. The estimated error of this measure is 0.05 GPa (Mao *et al.*, 1986). This method was used to monitor the pressure during all the XRPD experiments of this thesis.

3.1.2 Data analysis

After collecting 2D images of the Debye diffraction ring, the XRPD data treatment begins with the conversion of the images into the classical intensity *vs.* 2θ view through an integration process. The software used for this transformation is DIOPTAS (Prescher and Prakapenka, 2015). Once obtained the XRPD patterns in the desired form, structural refinements can be performed.

As well known, a structural refinement allows to optimize a pre-existing structural model, modifying it in order to minimize the differences between the calculated XRPD pattern of the model and the measured XRPD pattern of the studied sample. During a structural refinement, different variables are considered, for example, the unit cell parameters (related to the diffraction peaks position), the atomic coordinates, the atomic thermal parameters, the occupancy factors of the atoms etc.

When refining zeolite samples hosting in their cavities guest species, the atomic positions of these guest species have to be found and added in the structural model. This missing information is hidden in the relative peak intensities of the observed diffraction pattern.

The peak intensity of a *hkl* peak is related to the structure factor F_{hkl} which is defined as:

$$\mathrm{F_{hkl}} = \sum_{1}^{n} \mathrm{f}_n \, \mathrm{e}^{2\pi i(\mathrm{h}x+\mathrm{k}y+\mathrm{l}z)}$$

where f_n is the atomic scattering factor for the atom *n*, and *x*,*y*,*z* are the fractional coordinates of the atom *n*. The structure factor of an *hkl* reflection is basically the resulting wave scattered, at a certain angle, from all the *n* atoms present in the unit cell. Hence, the intensities of all the diffraction peaks are related to the atom types and position inside the unit cell.

The structure factor equation can be also express in terms of electron density (ρ):

$$\mathrm{F_{hkl}} = \int_{\mathrm{V}} \rho\,(\mathrm{x})\ \mathrm{e}^{2\pi i(\mathrm{h}\cdot\mathrm{x})} d\mathrm{v}$$

In this formula, the Miller indexes *hkl* are represented with a vector h, and the *xyz* coordinate are substituted with the vector x in the direct space.

We can generate the electron density from the inverse Fourier transform of the structure factors, as shown in the following formula:

$$\mathrm{\rho(x)} = \frac{1}{\mathrm{V}} \sum_{\mathrm{h}} \mathrm{F\,(h)e}^{(-2\pi i \mathrm{h \cdot x})}$$

During a structural refinement it is possible to generate a difference Fourier map, which shows the difference between the ρ calculated using the observed $|F_o|$ and the calculated $|F_c|$ as coefficient of a Fourier series:

$$\Delta\rho = \rho_o(x, y, z) - \rho_c(x, y, z) = \frac{1}{V} \sum (F_o - F_c) e^{(-2\pi i(hx + ky + lz)}$$

In this way, positive maxima in the difference Fourier map, represent missing atoms in the structural model that can be added. The intensity of the maxima is strictly related to the atom type (hence, the number of electron) and the occupancy factor, which statistically indicates the presence or not of one atom.

In this thesis work the Rietveld and the Le Bail methods were used in order to refine the structure of the zeolite materials or to determine the unit cell parameters.

The Rietveld method (Young, 1993) is a least-squares procedure, which minimizes the following quantity:

$$\mathrm{Sy} = \sum_i \mathrm{w}_i\,(\mathrm{Y}_i - \mathrm{Y}_{ci})^2$$

Where Y_i is the observed intensity at point i of the observed powder pattern and Y_{ci} is the calculated intensity. The weight, w_i, is based on the counting statistics, $w_i=Y_i^{-1}$, although at different stages of the refinement it may be advantageous to use $w_i=Y_{ci}^{-1}$. The contribution to Y_{ci} from Bragg reflections, diffraction optics effects and instrumental factors is expressed as:

$$\mathrm{Y}_{ci} = \mathrm{s} \sum_{\mathrm{H}} \mathrm{L\,M_H |F_H|^2 \varphi(2\theta}_i - 2\theta_{\mathrm{H}})\mathrm{P_H A} + \mathrm{Y}_{\mathrm{b}i}$$

Where:
s = overall scale factor
H = hkl indices of the Bragg reflection
L = Lorentz and polarization factors
M_H = multiplicity of the reflection
F_H = structure factor for H_{th} Bragg reflection
$\varphi(2\theta_i-2\theta_H)$ = profile function where $2\theta_i$ is corrected for the 2θ zero error
P_H = preferred orientation function
A = absorption factor
Y_{bi} = background intensity at step *i*

The refinement of all these parameters, combined with the analysis of the difference Fourier maps and the possibility to add entire molecules in the structural models, allows to determine the structure of the loaded zeolite samples.

The final reliability of a refinement is expressed on the basis of different indexes, the results showed in this manuscript are expressed with the coefficient R_{F^2} (Toby 2006) defined as:

$$R_{F^2} = \frac{(\sum_{hkl} F^2 o,_{hkl} - F^2 c,_{hkl})}{(\sum_{hkl} F^2 o,_{hkl})}$$

In the Le Bail method (Le Bail, 2005), the Rietveld extraction method is used to estimate reflection intensities without a structural model. The extracted intensities of the individual peaks are no longer treated as least-squares parameters and are never refined. Initially, all of the peak intensities are set to an arbitrary value. These are treated as "calculated" values as if they had been derived from a structural model. The F_{hkl}(calc) are set from extracted F_{hkl}(obs), and the process uses iteratively the Rietveld decomposition formula for the whole powder pattern. Generally, the intensities extraction from powder diffraction data are complicated by overlapping diffraction peaks with similar d-spacings. For the Le Bail method, the unit cell and the space group of the sample must be predetermined because they are included as a part of the fitting technique. The algorithm involves refining the unit cell parameters, the background, the profile parameters, and the peak intensities to match the measured powder diffraction pattern.

All structure refinements showed in this thesis, with both Rietveld and Le Bail methods, were performed using GSAS package (Larson and Von Dreele, 1994) with the EXPGUI interface (Toby, 2001).

3.2 Thermogravimetric analysis (TGA) and Evolved Gas Mass Spectrometry (MSEGA)

The thermal analyses were performed with two different instruments: for Na-X and Na-Y samples (paragraph 4.2.2. *Na-X and Na-Y nanosized zeolites*) were performed using a SETSYS instrument (SETARAM) analyzer at Laboratoire Catalyse et Spectrochimie in Caen, with heating rate of 5 °C/min and a 40 mL^{-1} flow of air; for mordenite sample were carried out at the University of Modena and Reggio Emilia using a Seiko SSC/5200 thermal analyzer. The samples were loaded in a Pt sample holder and heated in the following experimental conditions: heating rate 20 °C/min, temperature range 20-1000 °C. All the samples were exposed to air before performing the TG analysis. The second thermal analyzer is equipped with a quadrupole mass spectrometer (ESS, GeneSys Quadstar 422) to analyze the gas evolved during heating. All the TG analyses with MSEGA were performed in He atmosphere with a flux of 100 ml/min. The gas analyses were performed in multiple ion detection mode (MID), allowing the qualitative determination of the evolved masses *vs*. time or temperature.

3.3 TEM

The crystal size, morphology and crystallinity of nanosized Na-X and Na-Y samples were determined by transmission electron microscopy (TEM) using a Titan 80-300 operating at 300 kV at the Laboratoire Catalyse et Spectrochimie in Caen.

3.4 SEM

The SEM images of Na-mordenite sample were collected on a JEOL JSM-IT300LV instrument, at Dipartimento di Scienze della Terra of Turin University. The instrument is equipped with an X-ray microanalysis system in energy dispersion (EDS) Oxford INCA Energy 200 and a detector INCA X-act SSD. The images were collected at 20 KeV.

3.5 Elemental analysis

The elemental analyses were performed using a Flash 2000 CHNS/MAS200R instrument at Modena and Reggio Emilia University. The analyzer is based on the principle of "FLASH" dynamic combustion (modified Dumas method), followed by reduction, entrapment, complete chromatographic separation and detection with a thermal conductivity detector (TCD). The sample, solid or liquid, is dropped into a high-temperature oven, at 1000 °C. At the same time, a quantity of oxygen is released automatically to induce a drastically oxidation until the temperature reaches the maximum of 1800 °C (flash combustion). In these conditions any product is decomposed releasing elementary gases. The Flash 2000 pneumatic circuit ends with a GC finish, consisting of a separation chromatographic column and a sensitive TCD detector. The amount of sample used for the analyses ranges from 0.1 mg to few mg. The result is expressed as mass percentage of the element within the sample. The analyzed elements were C, N, H and S.

3.6 Infrared spectroscopy

Infrared (IR) spectroscopy is a reliable and well recognized fingerprinting method to characterize and identify many substances. This vibrational spectroscopy technique can be used to obtain spectra from a very wide range of solids, liquids and gases, and can be used in transmission or in reflection mode.

The IR spectra performed in this thesis were collected with two different instruments. A FTIR Nicolet 6700 IR spectrometer at laboratories of the University of Caen was used on Na-X and Na-Y samples (chapter 3: *CO_2 adsorption in Na-X and Na-Y nanosized zeolites*). A Bruker IFS 28 instrument, equipped with a Globar source and a La-DTGS or MCT detector, was used on mordenite + amino acid samples (chapter 4: *Confinement and condensation of amino acid molecules in Na-mordenite*).

The FTIR spectrometer uses an interferometer to modulate the wavelength from a broadband infrared source. A detector measures the intensity of transmitted or reflected light as a function of its wavelength. The signal obtained from the detector is an interferogram, which must be analyzed with a computer using Fourier transforms to obtain a single-beam infrared spectrum.

3.7 Raman spectroscopy

The Raman spectroscopy is a technique used to determine vibrational, rotational and other low-frequency modes of molecules. The Raman scattering, an inelastic scattering of photons, can be detected illuminating a sample with a laser beam. The instrument used to collect the Raman spectra showed in this thesis is located at the ICGM (Institute Charles Gerhardt Montpellier), University of Montpellier. The non-compact instrument was assembled by different pieces (Figure 3.6). A green laser source (532 nm wavelength) generates the laser beam, an optical path composed by lenses and filters allows the beam to arrive to a microscope able to focalize the beam on the sample and to detect the Raman signal in reflection mode. The sample stage is able to accommodate the DAC to perform *in situ* high-pressure experiments (Figure 3.7a and b).

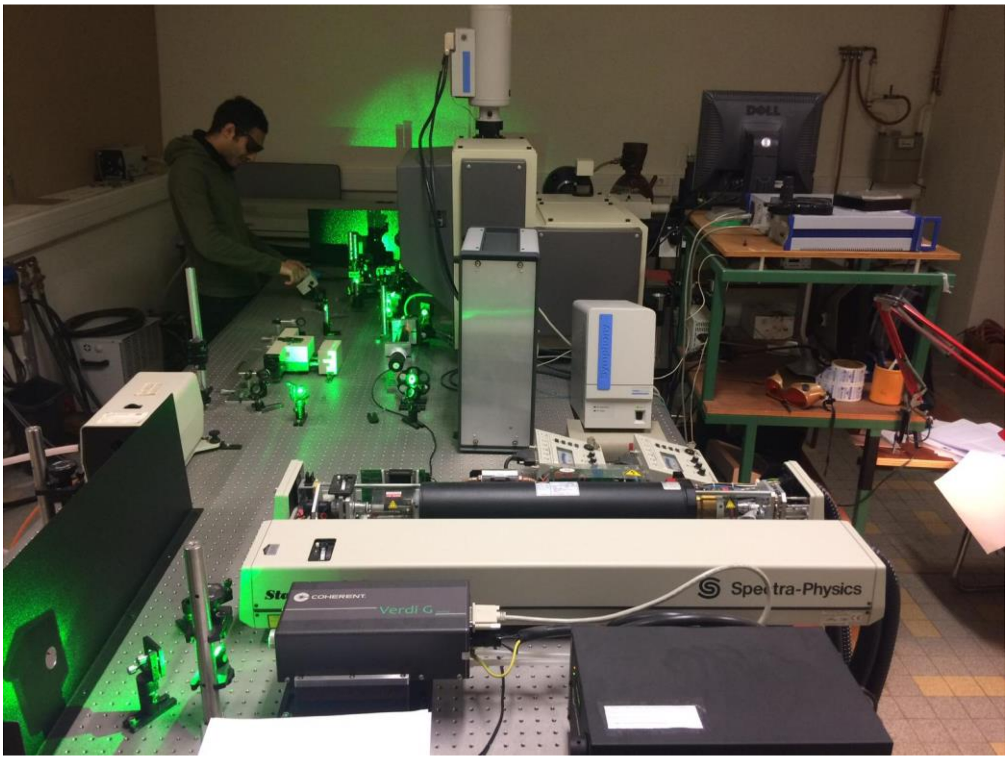

Figure 3.6: Raman instrument at the University of Montpellier.

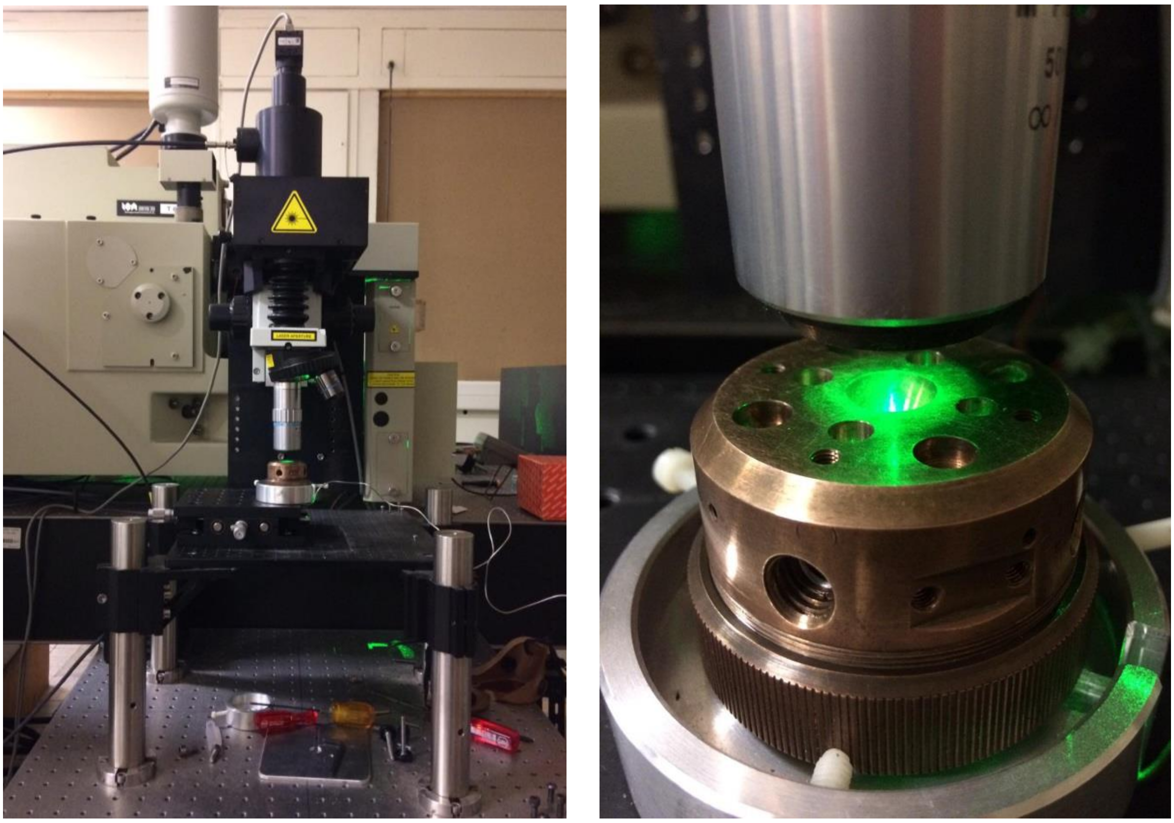

Figure 3.7: a) (left) Raman microscope; b) (right) DAC under the green laser beam.

3.8 Dynamic light scattering analysis

The size of the FAU nanoparticles was measured by a Malvern Zetasizer Nano instrument using a backscattering geometry (scattering angle of 173°, He–Ne laser with a 3 mW output power at a wavelength of 632.8 nm). The dynamic light scattering (DLS) analyses were performed on samples in water suspensions with a solid concentration of 1 weight %.

3.9 ICP analysis

The chemical composition of FAU was determined by inductively coupled plasma (ICP) optical emission spectroscopy using a Varian ICP-optical emission spectroscopy 720-ES.

4 CO_2 ADSORPTION IN Na-X AND Na-Y NANOSIZED ZEOLITES

The results presented in this chapter are reported in the paper: Michelangelo Polisi, Julien Grand, Rossella Arletti, Nicolas Barrier, Sarah Komaty, Moussa Zaarour, Svetlana Mintova, and Giovanna Vezzalini. CO_2 Adsorption/Desorption in FAU Zeolite Nanocrystals: In Situ Synchrotron X-ray Powder Diffraction and in Situ Fourier Transform Infrared Spectroscopic Study. *Journal of Physical Chemistry C* 2019, 123. Pages: 2361-2369.

4.1 Introduction

Climate change is a global challenge our generation is facing, which will probably affect the future generations if not contrasted. One of the main causes of climate change is the continuous increase of carbon dioxide, one of the principal greenhouse gases, in the atmosphere (Yang *et al.*, 2008). As long as the global energy requirements are satisfied by the combustion of carbon-based fossil fuels, serious environmental problems must be faced with efficient solutions, first of all the reduction of CO_2 emission. Different technologies have been examined during the last years in order to capture and separate CO_2 from flue gases. The CO_2 capture in solid systems provides a way to permanently store, easily transport, and possibly extract this gas, skipping the technical and environmental difficulties involved in largescale direct stocking into the Earth’s depths.

Several works explored methods of separation using different kinds of materials operating via weak physisorption interactions or strong chemisorption processes (Choi *et al.*, 2009). Activated carbon materials, polymers, calcium oxides, hydrotalcites, mesoporous and microporous materials (such as zeolites and MOFs) are currently studied as adsorbent materials (Morris *et al.*, 2008). Reactions, characterized by CO_2 trapping via open-structure solid-state systems, allow tuning CO_2 equilibrium in a given environment and represent an efficient way of low-energy storage/release of this gas.

Among the cited materials, zeolites are appropriate candidates for selective adsorption and separation of carbon dioxide (Siriwardane *et al.*, 2001), not only because of their high adsorption capacity and their particularly low price (Choi *et al.*, 2009; Zukal *et al.*, 2010) but also because their properties (i.e., crystal size, pore architecture, chemical composition, and nature of extraframework cations) influencing the adsorption performance, can be tuned systematically during synthesis process. Particular attention has been paid to faujasite-type zeolites (FAU framework type, paragraph *4.2.1*), which are considered as possible good candidates for CO_2 separation process. The adsorption performances of FAU-type zeolites (synthetic zeolites X and Y), were investigated with different methods. Lee *et al.* (2002) and Lu *et al.* (2008) found that zeolite 13X possesses higher adsorption capacity for CO_2 and a more favorable adsorption, with respect to activated carbon composites. Siriwardane *et al.* 2005, studying, by adsorption isotherms, the performance of different zeolites, reported that 13X zeolite shows preferential adsorption for CO_2 from a gas mixture representing coal combustion compared to other commercial zeolites (4A, 5A, APG-II, and WE-G 592). Also, computational studies (Maurin *et al.*, 2005; Plant *et al.*, 2006) indicate zeolites X and Y as the most promising adsorbents for CO_2 storage. Recently, experimental diffraction studies have been carried out to investigate the adsorption properties of zeolite Na−Y, under a structural point of view, by both neutron (Wong-Ng *et al*., 2013) and synchrotron X-ray powder diffraction (Arletti *et al*., 2016). Both studies indicate that the cations and H_2O molecules distribution in zeolite pores strongly affects the carbon dioxide adsorption/desorption dynamics.

In recent years, the interest in nanosized zeolites is strongly increased due to the potential variation of the properties of these materials as a function of the powder grain size (Mintova *et al.*, 2015). The advantages of using nanosized zeolites lie in their unique properties such as tunable crystal size, larger external surface areas, reduced diffusion path lengths, and more accessible active sites compared to micron-sized zeolite crystals. On the other hand, the size of zeolite crystals plays a major role when it comes to biomedical applications. As mentioned in chapter 1.6 (A*pplications fields of zeolites*), new biomedical techniques require the use of nanosized carriers. The modifications of zeolite crystal size, from micron to nanoscale, yielding biocompatible nano-zeolites, become a forefront research field. The target delivery of CO_2 by nanozeolites is considered an essential moderator in human physiology, controlling blood circulation and pH (Anfray *et al.*, 2017; Komaty *et al.*, 2018; Georgieva *et al.*, 2018).

In order to exploit the nanozeolites functionalities and to design tailor-made materials, it is of paramount importance to unravel the mechanisms that underlie the CO_2 trapping phenomena, by understanding the host-guest interactions.

As detailed reported in the next pages of this thesis, the CO_2 adsorption/desorption mechanism in two nanosized zeolite samples with FAU framework type, having different Si/Al ratios, cations, and particle size distributions is investigated. Combined in situ synchrotron high-resolution XRPD and in situ Fourier transform infrared (FTIR) spectroscopy experiments were carried out to unravel the host−guest and guest−guest interactions governing the CO_2 adsorption/desorption mechanism.

4.2. Materials

4.2.1 FAU type zeolite

The natural zeolite faujasite, having FAU framework type, has been discovered in 1842 and although it is not a common zeolite, it is important among zeolites, due to its synthetic counterparts, largely used as sorbents and catalysts.

The topological symmetry of the FAU materials is *Fd-3m*, the idealized parameter of the cubic unit cell is 24.345 Å, and the volume is 14428.8 Å^3 (http://europe.iza-structure.org/IZA-SC/ftc_table.php). The framework structure is formed by two composite building units: *sod* and *d6r* (fig 4.1).

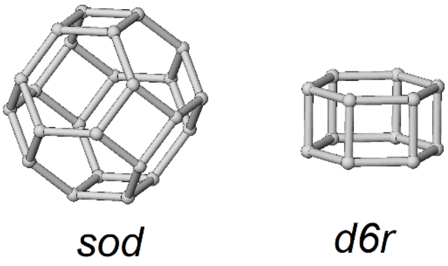

Figure 4.1: Composite building units of FAU structure

The sodalite cages (*sod*, or *β* cage) are connected each other through the double 6-membered rings (*d6r,* hexagonal prism). Specifically, every sodalite unit is connected in a cubic manner to other four sodalite cages tetrahedrally placed around it. In this way bigger cages, called supercages, interconnected among them by windows of 12-membered ring, are formed (Bergerhoff *et al.*, 1958). The diameter of these 12-rings is 7.4 Å from oxygen to oxygen. Each unit cell contains 8 supercages, 8 sodalite cages, 16 double 6-rings and 16 12-rings. The FAU structure (figure 4.2) can be described as the diamond structure, in that the sodalite cages are stacked in the same way of carbon atoms in diamond (Baur 1964).

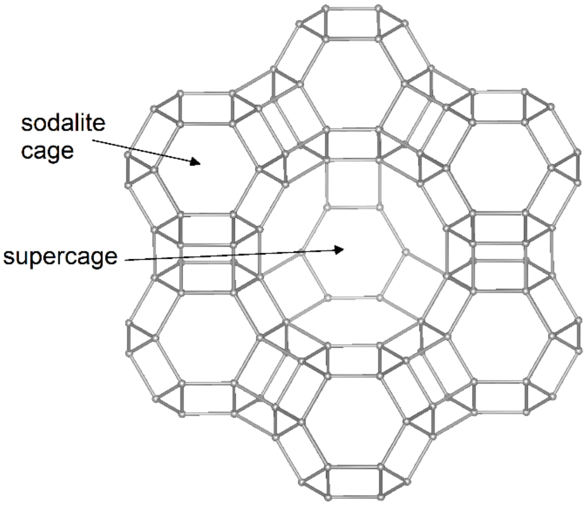

Figure 4.2: FAU framework, viewed along the [111] direction

The framework density of FAU structure is about 12.7 T/1000 Å^3 and corresponds to the most open framework among the natural zeolites.

The Si content in the natural samples is variable from 64% to 72% (Gottardi and Galli, 1985). In the synthetic FAU zeolites, depending on the Si/Al ratio, the FAU zeolites can be divided in types X and Y, in which the Si/Al ratio is respectively 1-1.5 (type X) and higher than 1.5 (type Y) (Julbe and Drobek, 2014).

Concerning the extraframework cations, several crystallographic sites accommodating cations are present in FAU structure. Frising and Leflaive (2008) listed in a review the cation distribution in X and Y zeolites, reordering the names of all crystallographic sites reported in literature for the FAU structure (figure 4.3 and table 4.1).

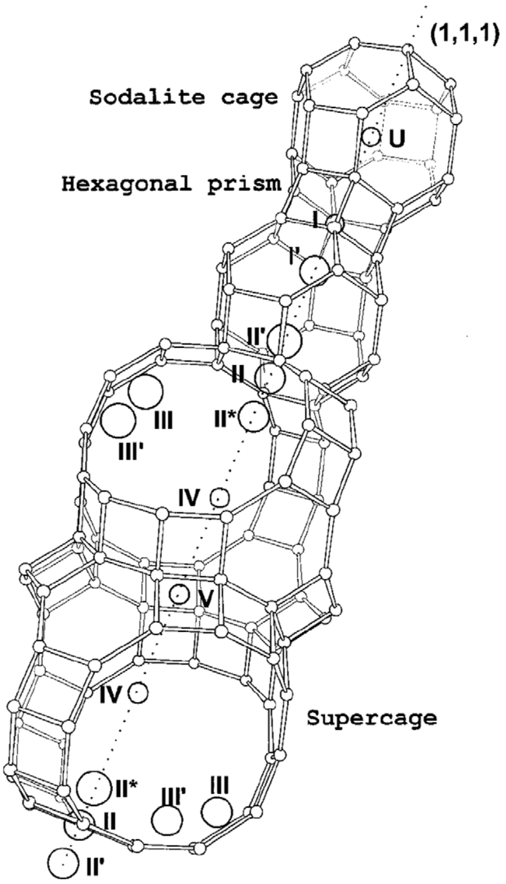

Figure 4.3: Cation positions reported by Frising and Leflaive (2008).

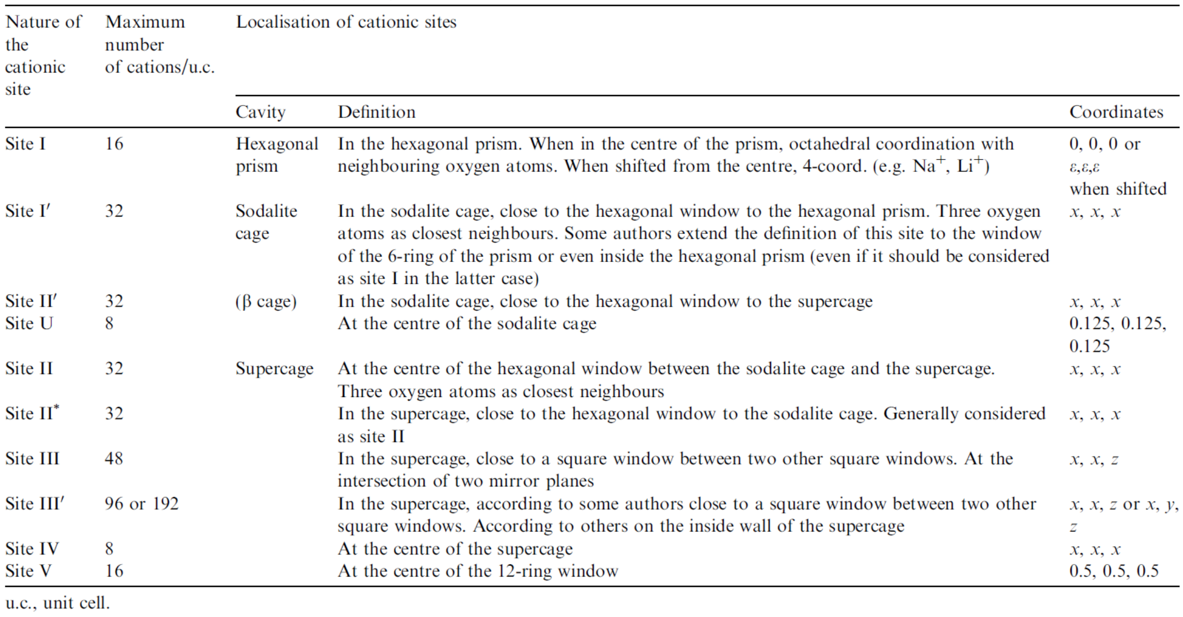

Nature of the cationic site	Maximum number of cations/u.c.	Localisation of cationic sites		
		Cavity	Definition	Coordinates
Site I	16	Hexagonal prism	In the hexagonal prism. When in the centre of the prism, octahedral coordination with neighbouring oxygen atoms. When shifted from the centre, 4-coord. (e.g. Na^+, Li^+)	0, 0, 0 or $\varepsilon,\varepsilon,\varepsilon$ when shifted
Site I′	32	Sodalite cage	In the sodalite cage, close to the hexagonal window to the hexagonal prism. Three oxygen atoms as closest neighbours. Some authors extend the definition of this site to the window of the 6-ring of the prism or even inside the hexagonal prism (even if it should be considered as site I in the latter case)	x, x, x
Site II′	32	(β cage)	In the sodalite cage, close to the hexagonal window to the supercage	x, x, x
Site U	8		At the centre of the sodalite cage	0.125, 0.125, 0.125
Site II	32	Supercage	At the centre of the hexagonal window between the sodalite cage and the supercage. Three oxygen atoms as closest neighbours	x, x, x
Site II*	32		In the supercage, close to the hexagonal window to the sodalite cage. Generally considered as site II	x, x, x
Site III	48		In the supercage, close to a square window between two other square windows. At the intersection of two mirror planes	x, x, z
Site III′	96 or 192		In the supercage, according to some authors close to a square window between two other square windows. According to others on the inside wall of the supercage	x, x, z or x, y, z
Site IV	8		At the centre of the supercage	x, x, x
Site V	16		At the centre of the 12-ring window	0.5, 0.5, 0.5

u.c., unit cell.

Table 4.1: Nature, multiplicity and localization of the cation sites in FAU structure reported by Frising and Leflaive (2008).

The more abundant cations in natural faujasites are Na^+ and Ca^{2+}, but FAU zeolites exchanged with different cations (K^+, Ba^{2+}, Cu^{2+}, Ni^{2+}, Li^+, Rb^+, Sr^{2+}, Cs^+, …) have been extensively studied over the last half century, due to their use in separation and catalysis engineering, being the distribution of the various cations in the zeolite structures one of the key aspects to understand the sorption mechanisms and selectivity.

The pores system, constituted by supercages and sodalite cages can accommodate about 235 H_2O molecules per unit cell (p.u.c.) in the natural sample (Gottardi and Galli, 1985). The H_2O content in X and Y synthetic samples varies depending on the cations type, cations number and also on the environmental conditions.

4.2.2 Na-X and Na-Y nanosized zeolites

The FAU type zeolites studied in this thesis project were synthesized at Laboratoire Catalyse et Spectrochimie in Caen (France). Specifically, two nanosized zeolites Na-X and a Na-Y were prepared, having different Si/Al ratio, cations and particle size.The following initial reagents were used for the preparation of the precursor mixtures: Al powder (Al, 325 mesh, 99.5 %, Alfa Aesar); aluminum hydroxide ($Al(OH)_3$, Sigma-Aldrich); sodium aluminate (Al_2O_3 ~ 50-56 wt. %, Na_2O ~ 40-45 wt. %, Sigma-Aldrich); sodium hydroxide (NaOH, Sigma-Aldrich, 97 %); colloidal silica (SiO_2, Ludox-HS 30, 30 wt. % SiO_2, pH = 9.8, Sigma-Aldrich); sodium silicate (SiO_2 ~ 26.5 wt. %; Na_2O, ~10 wt. %, Sigma-Aldrich). The zeolites were prepared according to the following procedures.

Na-X: The nanosized zeolite Na-X was synthesized from a clear precursor suspension. The initial reactants were mixed to prepare two initial solutions denoted A and B according to the following procedure: Solution A was prepared by dissolving 2.5 g of NaOH in 3 g double distilled water (dd H_2O) followed by slow addition of 0.297 g alumina powder (325 mesh, 99.5 %); solution B was prepared by mixing 10 g colloidal silica (Ludox-HS 30, 30 wt. % SiO_2, pH=9.8) with 1.1 g NaOH and 1 g of dd H_2O. Solution A was added dropwise under vigorous stirring to the solution B (solution B was kept in ice during the mixing). The resulting clear suspension was aged 24 h at room temperature, and then the water content was adjusted to obtain a colloidal precursor suspension with the following composition: 10 SiO_2: 1.1 Al_2O_3: 9 Na_2O: 50 H_2O. The hydrothermal crystallization was conducted at 50 °C for 24 h. After crystallization, the suspensions were purified by high-speed centrifugation (20000 rpm, 100 min). The resulting solid was washed with doubly distilled water until pH 7.5 was reached. The nanosized crystals were freeze-dried to prevent their irreversible agglomeration.

The resulting crystalline sample presents uniform particle size with average size of 20 nm as shown in the TEM image (Figure 4.4a) and DLS curve (Figure 4.4b), confirming the narrow, monomodal particle size distribution of the crystals.

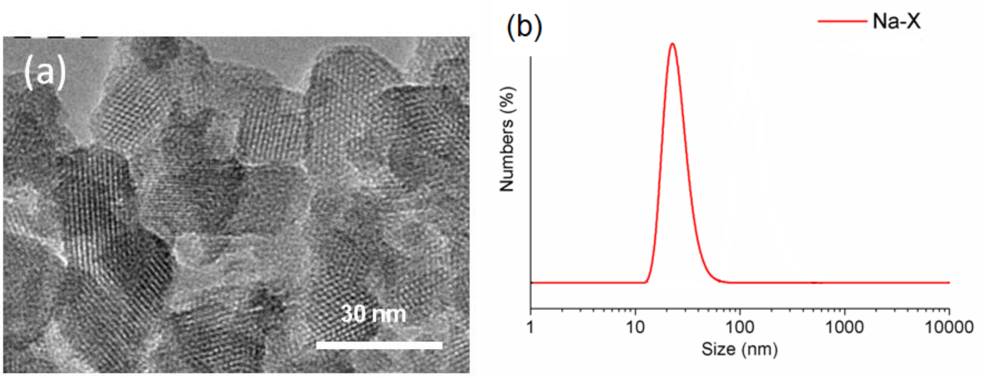

Figure 4.4: (a) TEM image of as-prepared Na-X crystals. (b) DLS curve of zeolite suspension with a solid content of 1 wt %.

The chemical composition (in wt %) determined by ICP analysis is: Si 19.5 %, Al 15.8 %, Na 14.5 %. The amount of water was determined by thermogravimetric analysis. In figure 4.5a the TG curve of Na-X sample shows a weight loss of 25%, in the DTG curve (Figure 4.5b) two main losses are present at 100 °C and 146 °C, corresponding to H_2O adsorbed on the surface of the nanoparticles and in the zeolite channels and hence differently bonded. Considering TG and ICP analyses, the chemical formula representing the nanosized Na-X sample is:

$$Na_{94.5}(Al_{87.6}Si_{104.4}O_{384}) \cdot 252H_2O \ (Si/Al = 1.19)$$

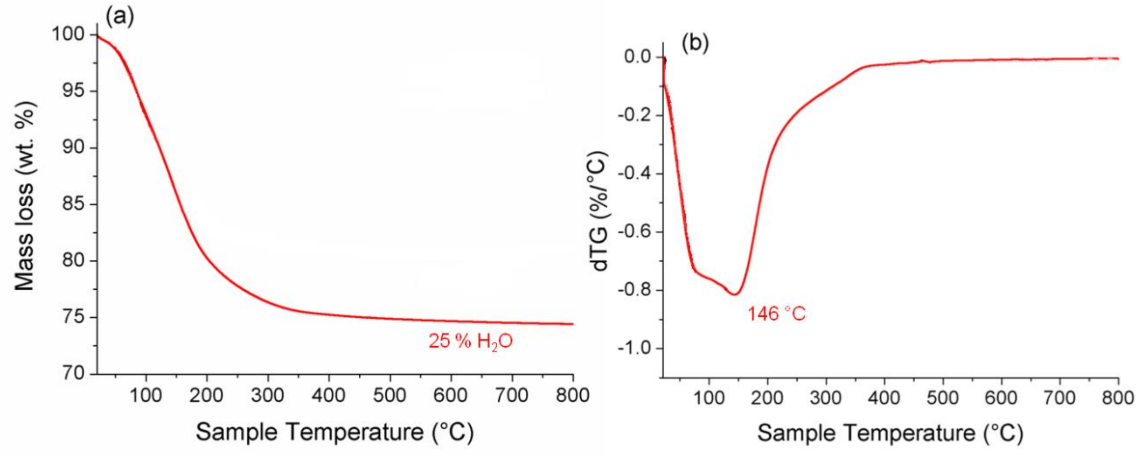

Figure 4.5: (a) TG and (b) DTG curves of Na-X zeolite.

Na-Y: The nanosized Na-Y zeolite was synthesized from a clear precursor suspension. The initial reactants were mixed to prepare two initial solutions denoted as A and B according to the following procedure: Solution A was prepared by dissolving 0.65 g of sodium aluminate in 3 g of dd H_2O; solution B was prepared by mixing of 13 g of colloidal silica (Ludox-HS 30, 30 wt. % SiO_2, pH=9.8) with 2.5 g of NaOH and 0.98 g of (dd) H_2O. Solution A was added dropwise under vigorous stirring to the solution B (solution B was kept in ice during the mixing). The resulting clear suspension was aged four days at room temperature. A colloidal precursor suspension with the following molar composition was obtained: 10 SiO_2: 0.7 Al_2O_3: 6.5 Na_2O: 122 H_2O. The hydrothermal crystallization was conducted at 100 °C for 2 h. The crystalline product was purified and dried in the same way described for zeolite Na-X.

The resulting sample presents uniform and highly crystalline particles with average size of 150 nm. Figure 4.6a shows the TEM image and figure 4.6b DLS curve of the Na-Y sample. The homogeneous nanocrystals exhibit a typical octahedral morphology with fully crystalline and well-developed faces.

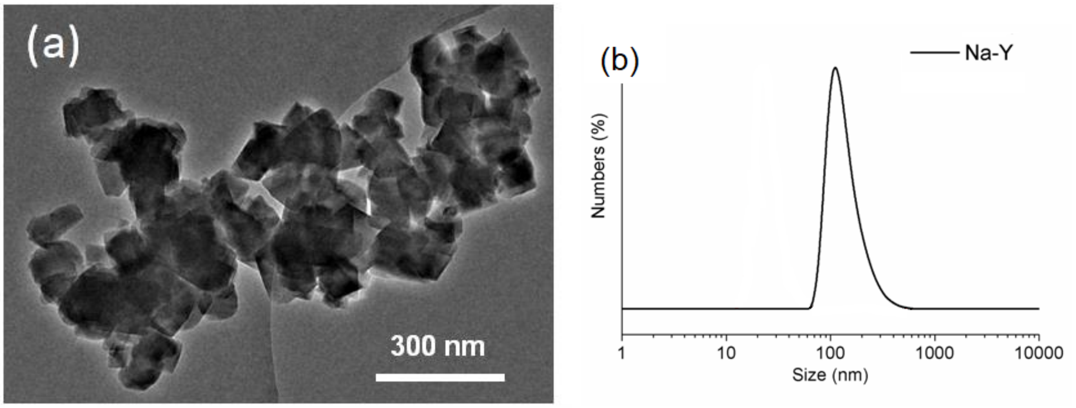

Figure 4.6: (a) TEM image of as-prepared Na-Y crystals. (b) DLS curve of zeolite suspension with a solid content of 1 wt %.

The chemical composition determined by ICP is the following: Si 43.1 %, Al 17.0 %, Na 15.4 %. The TG and DTG curves are shown in figures 4.7a and 4.7b. The only peak of the DTG is at 102 °C, contributing to 19 wt % loss of the total mass. The chemical formula resulting from ICP and TG is the following:

$$Na_{59.5}(Al_{55.9}Si_{136.1}O_{384}) \cdot 167H_2O \text{ (Si/Al = 2.43)}$$

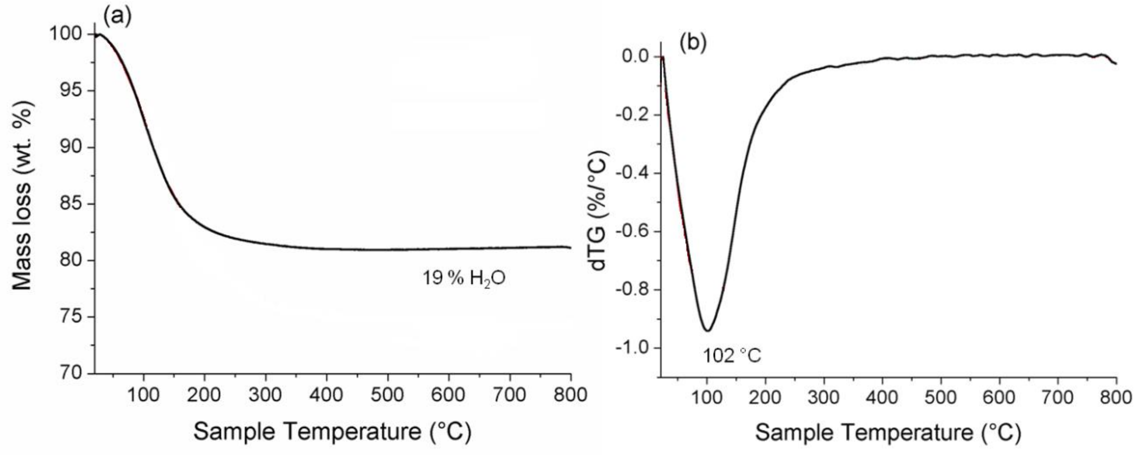

Figure 4.7: (a) TG and (b) DTG curves of Na-Y zeolite.

4.3 Experimental methods

4.3.1 *In situ* synchrotron XRPD experiments

The CO_2 adsorption - in situ XRPD experiments- on the two nano-zeolites Na-X and Na-Y were performed at the high-resolution beamline ID22 at ESRF (Grenoble, France) with a fixed wavelength of 0.3999 Å (Figure 4.8). LaB_6 was used as a standard to calibrate the wavelength. Na-Y and Na-X samples were packed in 0.7 mm quartz capillaries and mounted on a support connected to the gas rig. After an XRPD data collection at ambient conditions, the samples were heated in situ using a hot-air blower with a heating rate of 3 °C/min, from room temperature to 250 °C and evacuated nominally to 5×10^{-3} Torr by means of a turbo vacuum pump in order to favor the water release. Then a second XRPD pattern was collected.

The dehydrated samples were kept at room temperature and the XRPD data collected again. CO_2 was sent into the capillaries (maximum pressures 1.85 and 1.50 bar for Na-Y and Na-X, respectively) and equilibrated for 15 minutes before data collection. Then, the samples were pumped 10 minutes to test the CO_2 stability in zeolite porosities.

All the diffraction patterns were collected using the high-resolution multianalyzer, in the 2θ range 0.8−26° (data collection time: 37 min).

Resuming: for both samples, the data collections were performed in the following conditions:

(1) ambient conditions (labels Na-X-*RT* and Na-Y-*RT*);

(2) 250 °C (Na-X-*D-HT* and Na-Y-*D-HT*);

(3) room temperature after dehydration (Na-X-*D-RT* and Na-Y-*D-RT*); (4) after CO_2 loading (Na-X-CO_2 and Na-Y-CO_2);

(5) RT after pumping (Na-X-*AP* and Na-Y-*AP*).

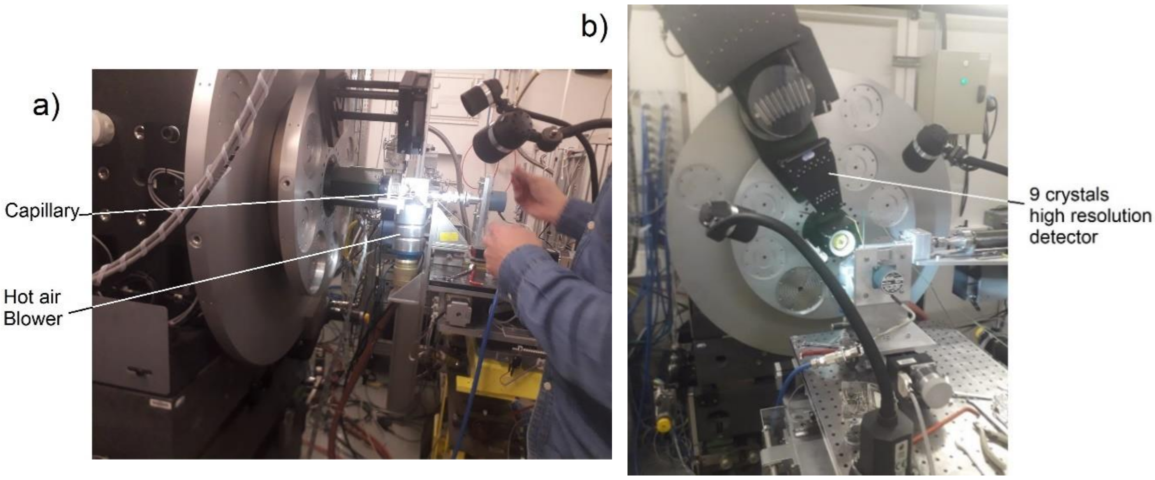

Figure 4.8: Sample holder (a) and detector (b) in ID22 beamline during the *in situ* gas adsorption experiment.

4.3.2 *In situ* FTIR experiments conditions

Na-X and Na-Y powders (about 20 mg each sample) were pressed, at ~10^7 Pa, into self-supported discs (2 cm^2 area) and placed in an IR cell equipped with KBr windows. The IR spectra were recorded using a Nicolet 6700 IR spectrometer with an MCT detector, and an extended-KBr beam splitter was used. Spectra were recorded in the 400−5500 cm^{-1} range with a resolution of 4 cm^{-1}, and 128 scans were collected for each spectrum. A movable quartz sample holder allowed placing the self-supported discs in the infrared beam, for recording spectra, and moving them into a furnace at the top of the cell for thermal treatment. The cell was connected to a high vacuum line with a reachable pressure of ~10^{-9} bar. The samples were activated in a two-step process: (i) 100 °C for 0.5 h to desorb most of the physisorbed H_2O and (ii) 250 °C for 2 h, to remove any chemisorbed H_2O. Both steps were performed under secondary vacuum (~5×10^{-9} bar). Then, small CO_2 doses were introduced into the FTIR cell at RT and kept in equilibrium for 15 min. High vacuum desorption was then conducted at room temperature for 15 min, followed by desorption at 250 °C for 15 min.

4.3.3 XRPD data analysis

In the CO_2 loaded Na-X and Na-Y refinements (Chapter 4.3 *Structural characterization*), to locate the loaded CO_2 molecules, the initial refinements were carried out in the space group (s.g.) $Fd\bar{3}$, using the framework coordinates published by Su and co-workers (2012). Sodium cations, H_2O, and CO_2 molecules were found by difference Fourier maps. After the localization of the extra-framework species, the refinement suggested a higher symmetry for the Na-Y zeolite, so for this sample, the $Fd\bar{3}m$ s.g. and the model of Olson (1970) were used for all refinements. Lattice parameters and refinement details are presented in table 4.2; observed and calculated patterns after Rietveld refinements are reported in Figure S1a−h. The Bragg peak profiles were modeled by a pseudo-Voigt function (Thompson *et al.*, 1987), and the peak intensity cutoff was set to 0.01 of the peak maxima. The background curve was fitted by a Chebyshew polynomial with a variable number of coefficients from 15 to 30. The 2θ-zero shift, the overall scale factor, and the unit cell parameters were refined accurately in each cycle. Soft constraints were imposed on the tetrahedral T−O (1.63 Å) and C−O lengths (1.18 Å), and the tolerance value was set at 0.03. The isotropic thermal displacement parameters of the framework oxygen atoms were constrained to the same value. For samples Na-X-RT and Na-Y-RT, also the thermal displacement parameters of the H_2O molecules were refined constrained to the same value.

Na-X	*-RT*	*-D-RT*	*-CO_2*	*-AP*
Space group	*Fd-3*	*Fd-3*	*Fd-3*	*Fd-3*
a (Å)	25.022(1)	24.980(2)	24.9669(14)	24.954(2)
V (Å^3)	15668(2)	15587(3)	15562(3)	15539(3)
Rp (%)	3.42	3.76	3.29	3.43
Rwp (%)	4.37	4.80	4.24	4.41
R F**2 (%)	4.88	6.93	3.74	4.22
No. of Variables	83	70	92	100
No. of observations	838	870	957	870

Na-Y	*-RT*	*-D-RT*	*-CO_2*	*-AP*
Space group	*Fd-3m*	*Fd-3m*	*Fd-3m*	*Fd-3m*
a (Å)	24.7570(2)	24.8542(5)	24.7947(4)	24.8282(4)
V (Å^3)	15173.8(4)	15353.1(9)	15243.3(8)	15305.0(8)
Rp (%)	3.09	3.46	3.15	3.11
Rwp (%)	4.08	4.63	4.11	3.98
R F**2 (%)	8.59	7.10	6.29	5.59
No. of Variables	74	67	95	94
No. of observations	609	728	718	718

Table 4.2: Lattice parameters and Rietveld refinement figures of merit for Na-X and Na-Y structures under the different conditions.

4.4 Structural characterization

4.4.1 Structures at ambient condition (Na-X-*RT*; Na-Y-*RT*)

The *in situ* XRPD measurements at room temperature and the corresponding Rietveld refinements allowed to obtain the structure features of both samples Na-X and Na-Y before dehydration and CO_2 adsorption/desorption cycling. In particular, the structural analysis allowed to determine the position and the amount of the extra-framework species (H_2O molecules and Na cations), which play -as shown below- an important role in the CO_2 sorption mechanism.

In the Na-X sample, four crystallographic independent Na sites were identified and named: Na2, Na2', Na3, Na6 (labelled after Olson, 1970), shown in figure 4.9. Na2 and Na2' sites are located in the sodalite cages and correspond to site I and I' according to the conventional classification reported in figure 4.3 (paragraph *4.2.1*). The existence of these two Na sites, very close each other, was explained by Olson (1995) on the basis of the aluminum content of the 6-ring to which they are coordinated, that could be 2 or 3 atoms in different 6-rings. A longer Na-O distance, related to cation Na2', is consistent with a lower Al content for these 6-ring. Na3 site is placed at the center of the hexagonal window between the sodalite cage and the supercage and corresponds to site II (Frising and Leflaive, 2008). Site Na6 is inside the supercage near the site III'b (Su *et al.*, 2012). The total amount of sodium is in good agreement with the ICP analysis, 96.5 atoms p.u.c. from the refinement *vs.* the 94.5 atoms p.u.c. from the chemical analysis. Six crystallographic independent H_2O sites were found, accounting for a total of 250 H_2O molecules, in perfect agreement with 252 molecules p.u.c. determined by TG analysis. Five H_2O molecules are located in the supercage, coordinated to the Na6 cations or in weak interaction with framework oxygen atoms, and one in the sodalite cage coordinated to Na2' cations (for structure details see Tables T1 and T2 in appendix).

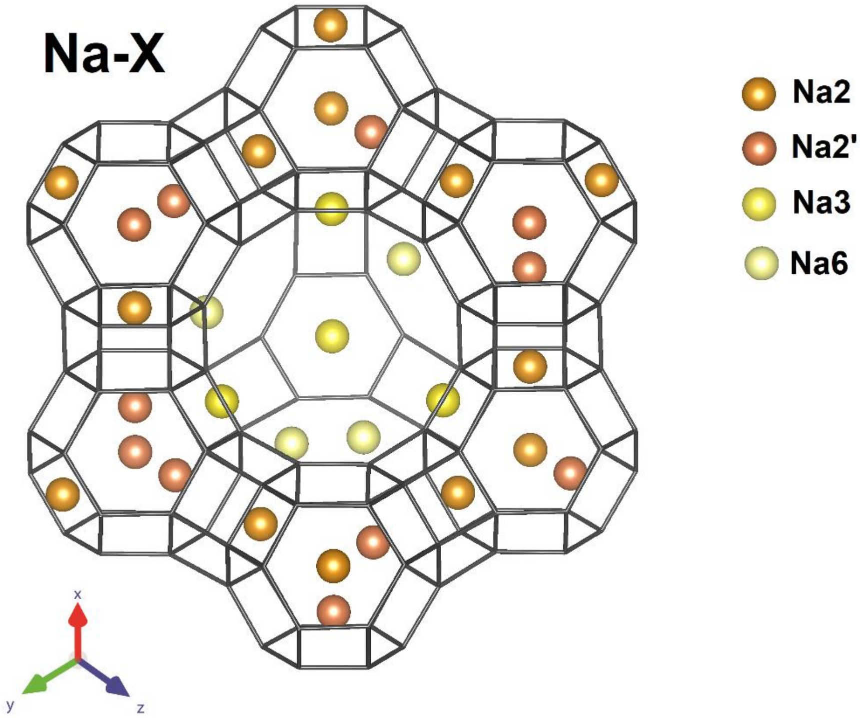

Figure 4.9: Cations location in Na-X-*RT* sample. View along the [111] direction of a single supercage. The number of drawn Na sites is according to their occupancy factors. H_2O molecules are not shown for sake of clarity.

The same Na sites were found in the Na-Y sample, with the exclusion of site Na6 located in the supercage (Figure 4.10). The total amount of sodium is 55.4 atoms p.u.c., which also in this case is in good agreement with the ICP results (59.5 Na p.u.c.). Five positions, accounting for 235 H_2O molecules p.u.c., were located in the supercage: two of them are in weak interaction with framework oxygen atoms and one is coordinated to the Na2' cations (Tables T1 and T2 in appendix). In Na-X sample, the H_2O content calculated by the Rietveld refinement was similar to that determined by the TG analysis, in the case of Na-Y, a higher amount of H_2O was obtained by the refinement. The difference could be related to the different hydrophilicity of the two samples, leading to different hydration degrees in relation to the environment humidity.

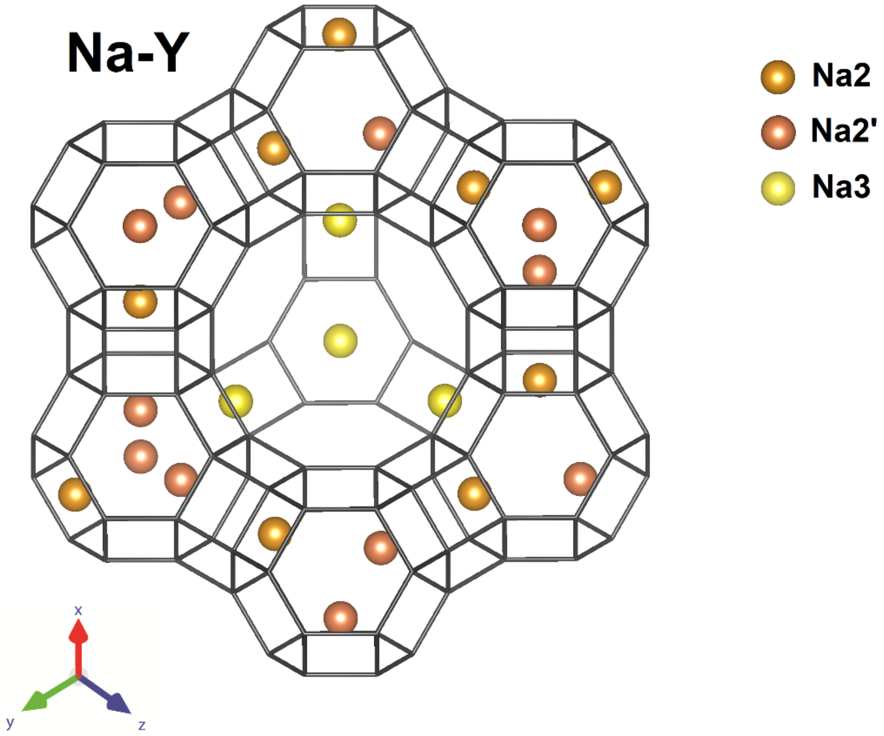

Figure 4.10: Cations location in Na-Y-*RT* sample. View along the [111] direction of a single supercage. The number of drawn Na sites is according to their occupancy factors. H_2O molecules are not shown for sake of clarity.

4.4.2 Structure of dehydrated FAU zeolites (Na-X-*D-HT*; Na-Y-*D-HT*)

After the RT data collections, both samples were dehydrated by heating. The removal of H_2O is a fundamental step for the use of FAU zeolites as adsorbents, since most of the porosity is occupied by H_2O molecules, hindering the penetration of other species at ambient condition. In the case of Na-X, the HT treatment at 250 °C seems to be not completely effective in dehydrating the sample, since the structural refinement shows the presence of about 38 residual H_2O molecules. On the contrary, sample Na-Y was successfully dehydrated under the HT treatment at 250 °C. Once the samples were brought back to *RT* conditions, due to their hydrophilic character, several H_2O molecules were re-adsorbed and 126 and 35 H_2O molecules p.u.c. were respectively located in samples Na-X-*D-RT* and Na-Y-*D-RT*. The figure 4.11 shows the residual amounts of H_2O calculated from the refinements during the dehydration steps in both samples.

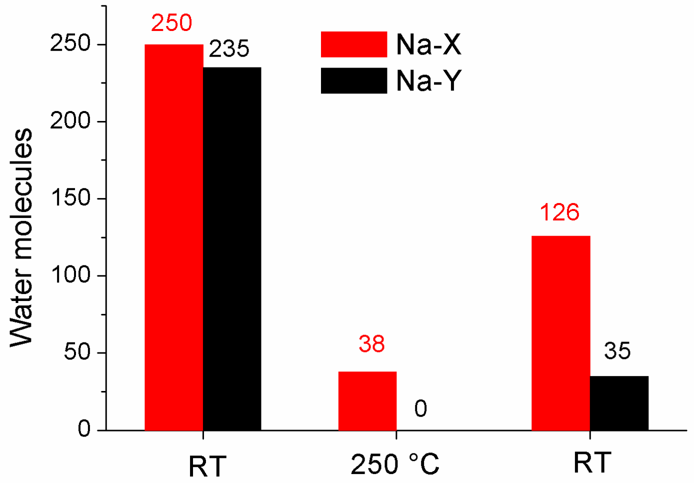

Figure 4.11. Number of H_2O molecules in as-prepared Na-X and Na-Y zeolites at room temperature (Na-X -*RT*, Na-Y-*RT*), at 250 °C and under vacuum ($5\cdot 10^{-3}$ Torr) (Na-X-*D-HT*, Na-Y-*D-HT*) and back to *RT* (Na-X-*D-RT*, Na-Y-*D-RT*) as determined by *in situ* XRPD and Rietveld refinement.

4.4.3 Structure of CO_2 loaded FAU zeolites (Na-X-*CO_2*, Na-Y-*CO_2*)

Once the dehydrated samples were recovered at ambient condition, CO_2 was sent in the capillaries and the gas adsorption was followed by *in situ* XRPD. The host-guest and guest-guest interactions are discussed in this section taking into account the presence of residual H_2O in zeolites cavities and the intrinsic limit of X-ray diffraction analysis, which allows the determination of an average structure for the material under study.

The inspection of the difference Fourier map and the analysis of distances and angles between the electron density maxima, suggested the presence of bi-dentate bicarbonate groups labelled CO_3-1 (Figure 4.12, Tables T1 and T2 in appendix), in the supercage of the Na-X sample, probably formed as a consequence of the interaction between the adsorbed CO_2 and the residual H_2O molecules. The less-shielded sodium cations hosted in the supercage (Na6 sites) can be responsible for the CO_2 molecules polarization. The preferential formation of bicarbonate groups, associated to the presence of cations in the supercage sites, has been already discussed by Jacobs *et al.* (1973). One of the oxygens forming the CO_3 group (site O13, Table T1 in appendix) corresponds to the H_2O molecule W8 in the dehydrated phase at room temperature (Na-X-*D-RT*). The presence of H_2O during the CO_2 adsorption has been demonstrated to favor the formation of bicarbonate species via hydroxyl group formation (Bonenfant *et al.*, 2008).

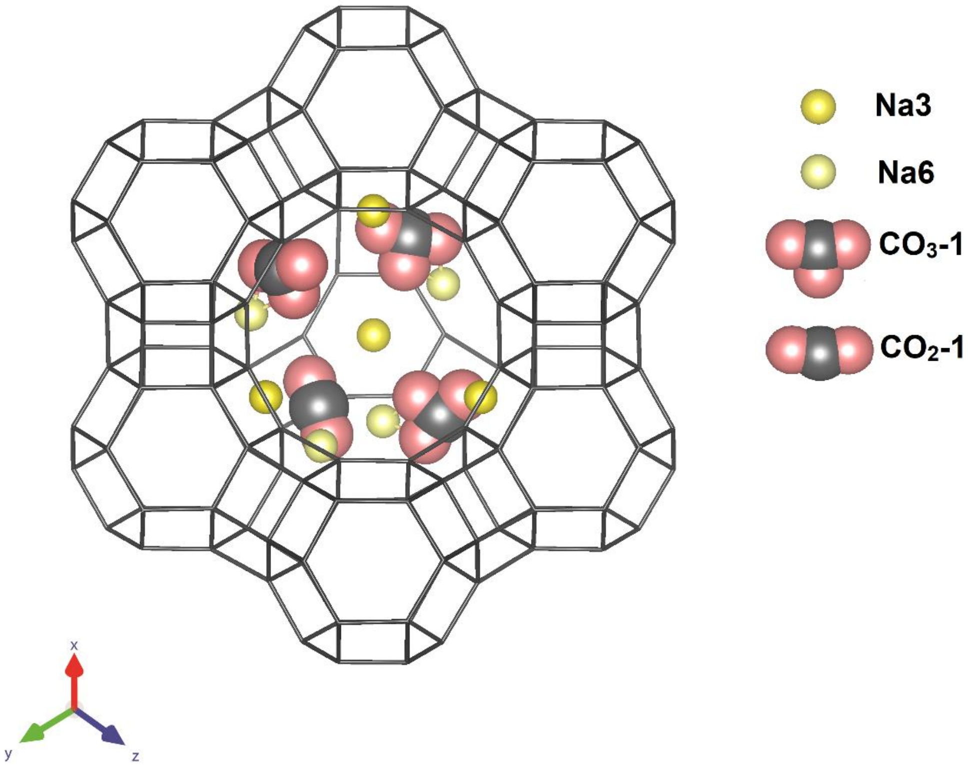

Figure 4.12: Extra-framework location in Na-X-*CO_2* sample. View along the [111] direction. Only the Na sites in the supercage are shown. H_2O molecules are not shown for sake of clarity.

From the inspection of figure 4.12, one can argue that the geometry of group CO_3-1, does not perfectly fit that of a bicarbonate group (i.e. with the angle O-C-O = 120°). This could be an artefact derived from the average structure determined by X-ray diffraction and can be attributed to the presence, in the same crystallographic positions, of a second configuration consisting of a linear CO_2 molecule and of a H_2O molecule, alternatively present (Figure 4.13).

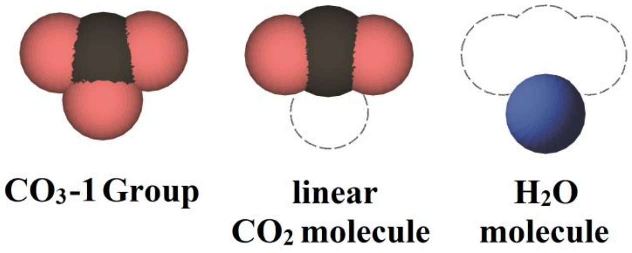

Figure 4.13: Possible configurations of the CO_3-1 group in Na-X-*CO_2* sample.

Assuming the alternative existence of CO_3^{2-}, CO_2 and H_2O it is impossible to establish the relative amount of the three species. However, assuming the only presence of the bicarbonate, the total number of bicarbonate groups would be 29 (i.e. 4.6 molecules in each supercage). The distribution of the bi-dentate bicarbonate groups, bonded to Na cations, present in one supercage is shown in Figure 4.14.

During the CO_2 adsorption, additional 35 H_2O molecules are delivered to the Na-X zeolite sample accounting for a total of 138 re-adsorbed H_2O molecules; the additional H_2O probably came from the CO_2 bottle or from the gas lines.

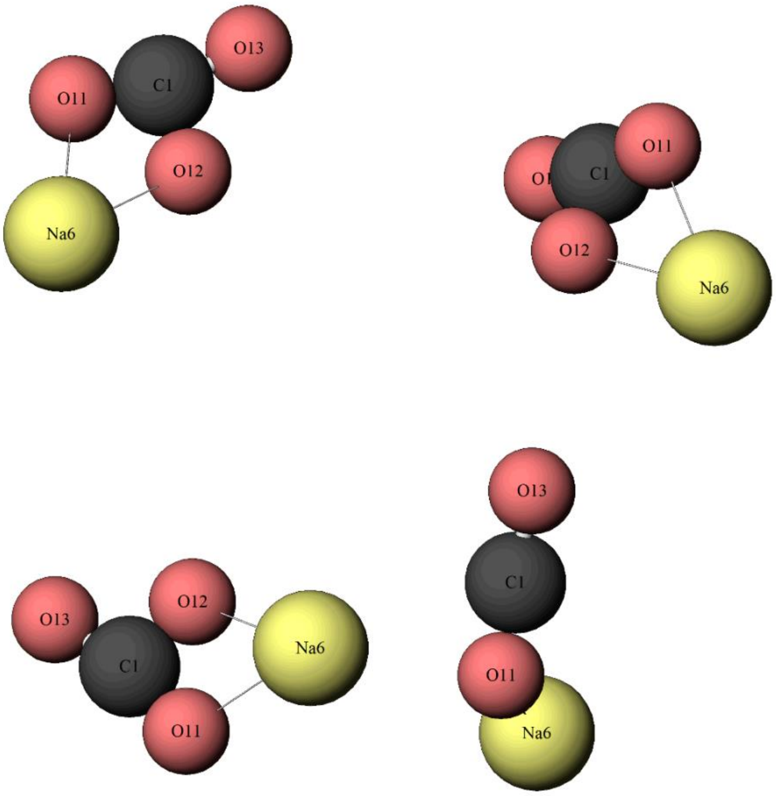

Figure 4.14. Possible distribution of CO_3^{2-} groups and Na6 cations in the supercage of the Na-X-CO_2 sample, taking into account their occupancy factors and distances (only bonded Na6 are drawn).

In the Na-Y sample only physisorbed CO_2 molecules are hosted in the supercage, accounting for a total amount of 66 molecules. CO_2 molecules occupy three different positions as shown in figures 4.15 and 4.16: (1) CO_2-2 (see Tables T1 and T2 in appendix for structural details) accounting for 14 molecules p.u.c. (i.e. 1.8 molecules in each supercage, in green in figures

4.15 and 4.16); (2) CO_2-3: lying in the 12-ring windows between two supercages, accounting for 34 molecules p.u.c. (i.e. 4.3 molecules per supercage, in red in figures 4.15 and 4.16); (3) CO_2-4, accounting for 18 molecules p.u.c. (i.e. 2.2 molecules per supercage, in blue in figures 4.15 and 4.16).

Even in the Na-Y zeolite further H_2O molecules are adsorbed during the delivery of the CO_2 and as a whole 55 H_2O molecules were found (not shown in figure 4.15 and 4.16).

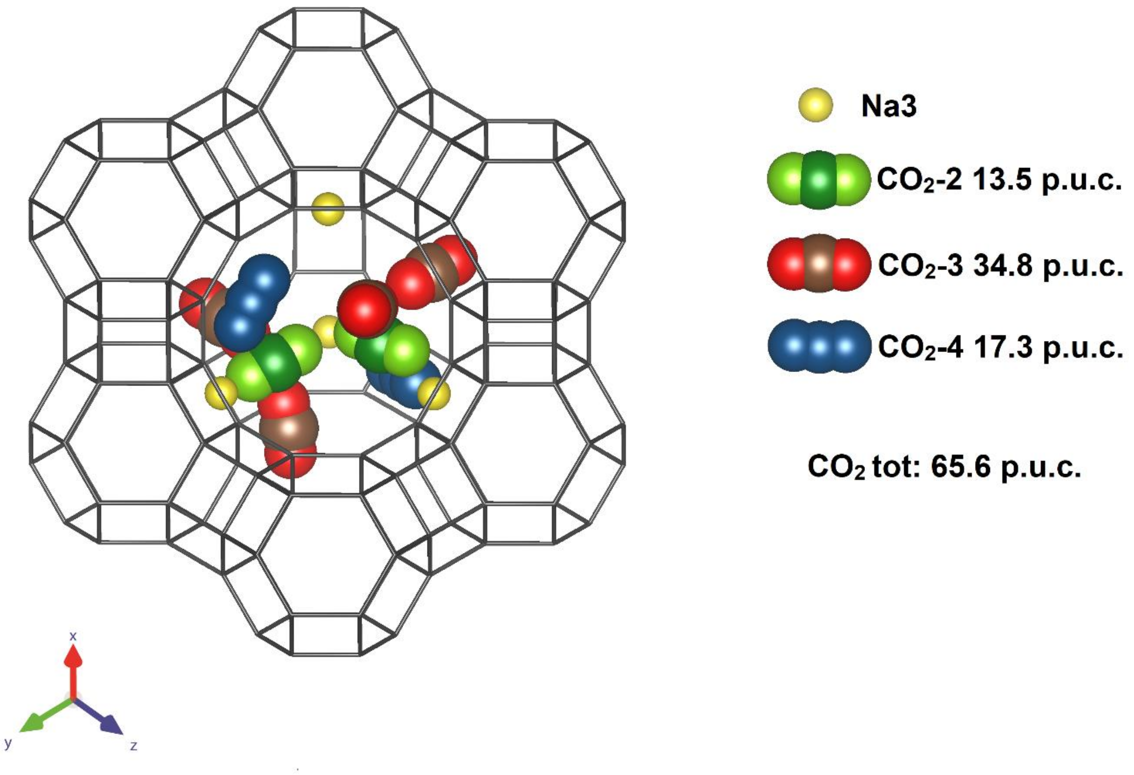

Figure 4.15: Extra-framework sites in Na-Y-CO_2 sample. View along the [111] direction. Only the Na sites in the supercage are shown. H_2O molecules are not shown for sake of clarity.

Figure 4.16 shows a possible distribution of the CO_2 molecules, Na^+ cations and W3 in the supercage of Na-Y, taking into account their occupancy factors, distances and steric hindrance. Two crystallographic equivalent CO_2 clusters, formed by one CO_2-2, two CO_2-3 and one CO_2-4 molecules, are coordinated to Na3 cations and W3 H_2O molecule via CO_2-2 and CO_2-4 molecules. Each cluster is involved in weak interactions with that hosted in the neighboring supercage via the CO_2-3 molecule sited in the 12 membered-ring (figure 4.17). The presence of these large clusters probably hinders further CO_2 adsorption.

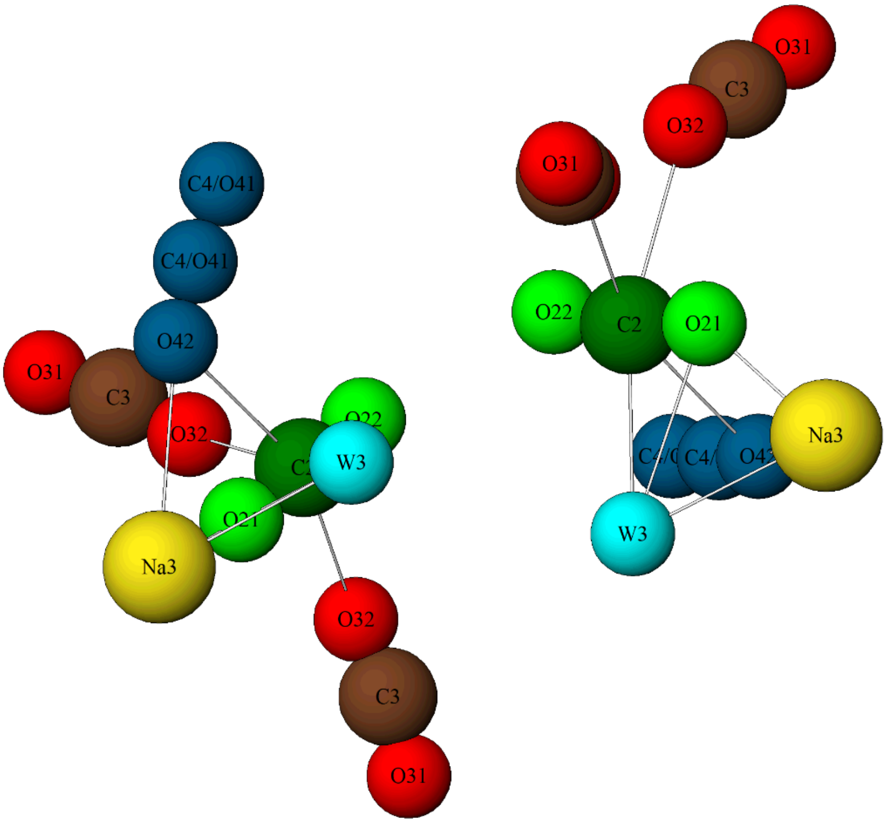

Figure 4.16: Possible distribution of CO_2 molecules, Na^+ cations and W3 molecule in the Na-Y-CO_2 supercage (only Na3 and W3 bonded to the clusters are drawn). The labels C2, O21 and O22 represent the CO_2-2 molecule, C3, O31 and O32 the CO_2-3 molecule and C4, O41 and O42 the CO_2-4 one.

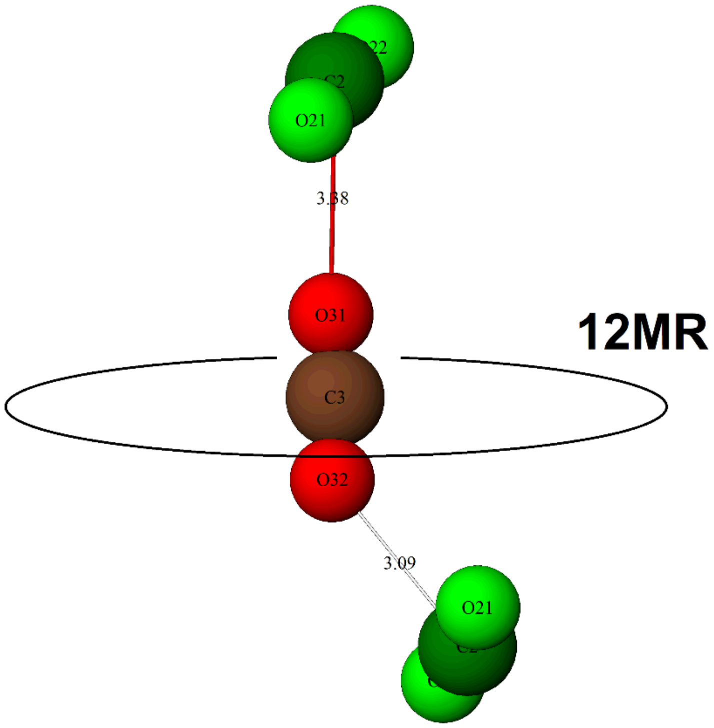

Figure 4.17: Interactions among CO_2-2 and CO_2-3 molecules in neighboring supercages in Na-Y-CO_2 through the 12MR.

The Na3 – CO_2 distances found for CO_2-2 and CO_2-4 are consistent with linearly coordinated molecules reported by Maurin *et al.* (2005). On the contrary, CO_2–3 is not coordinating cations, but shows weak interactions with framework hydroxyl groups (table T2b in appendix) as confirmed by the in situ FTIR results (explained in detail in the paragraph *4.5*), where a band at 3742 cm^{-1}, characteristic of silanol groups, is present in the activated zeolite (figure 4.18).

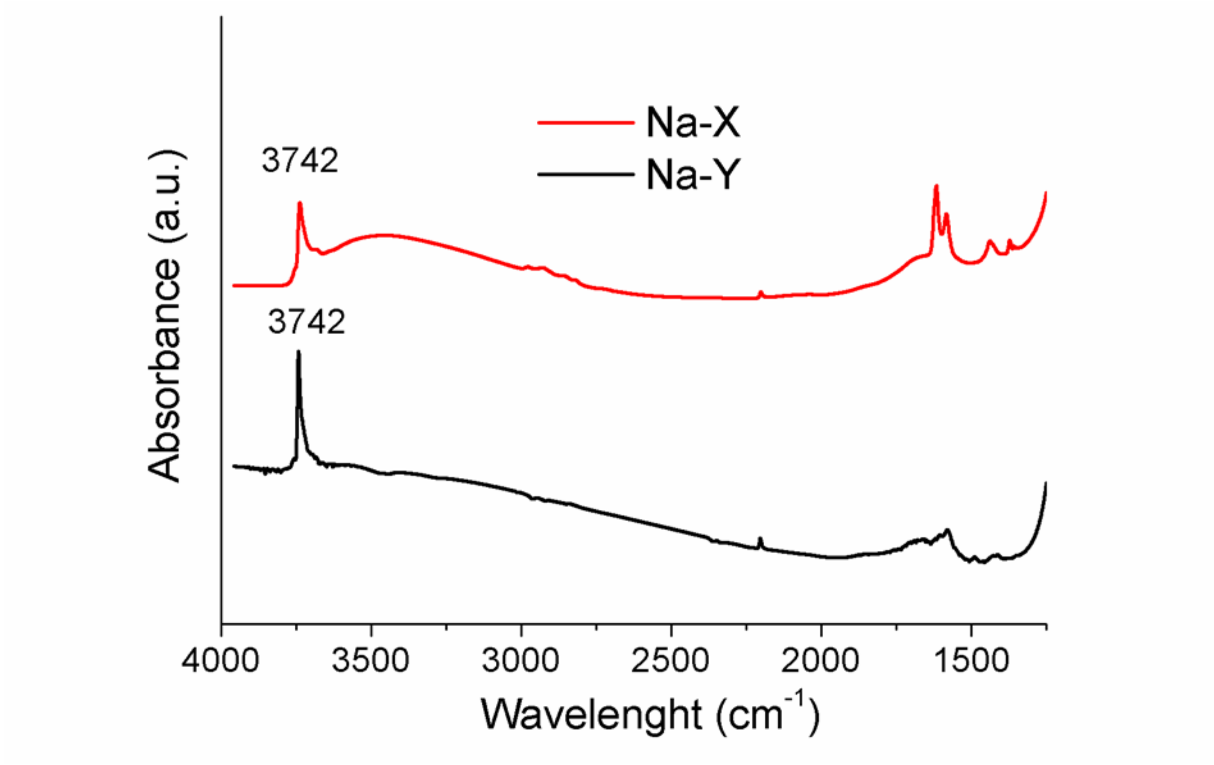

Figure 4.18: FTIR spectra of activated zeolite samples (250 °C) revealing the band at 3742 cm^{-1} characteristic of silanol groups.

Despite the presence of H_2O molecules and cations coordinating CO_2 molecules, the presence of carbonates is not detected. This probably because Na3, contrariwise to what observed for Na6 in Na-X, is well compensated by framework oxygen atoms and thus is less effective in the CO_2 polarization.

4.4.4 Structure after desorption of FAU zeolites (Na-X-*AP*, Na-Y-*AP*)

The desorption mechanism of CO_2 was studied under vacuum. The persistence of CO_2 in the zeolite samples is strongly dependent on the formed host-guest interactions. Refinement results show that Na-X-*CO_2* sample is stable even under vacuum (5 x 10^{-3} Torr): from 29 CO_3 bi-dentate bicarbonate groups “nominally” adsorbed (mentioned in previous paragraph), about 24 remain in the pores after pumping (figure 4.19).

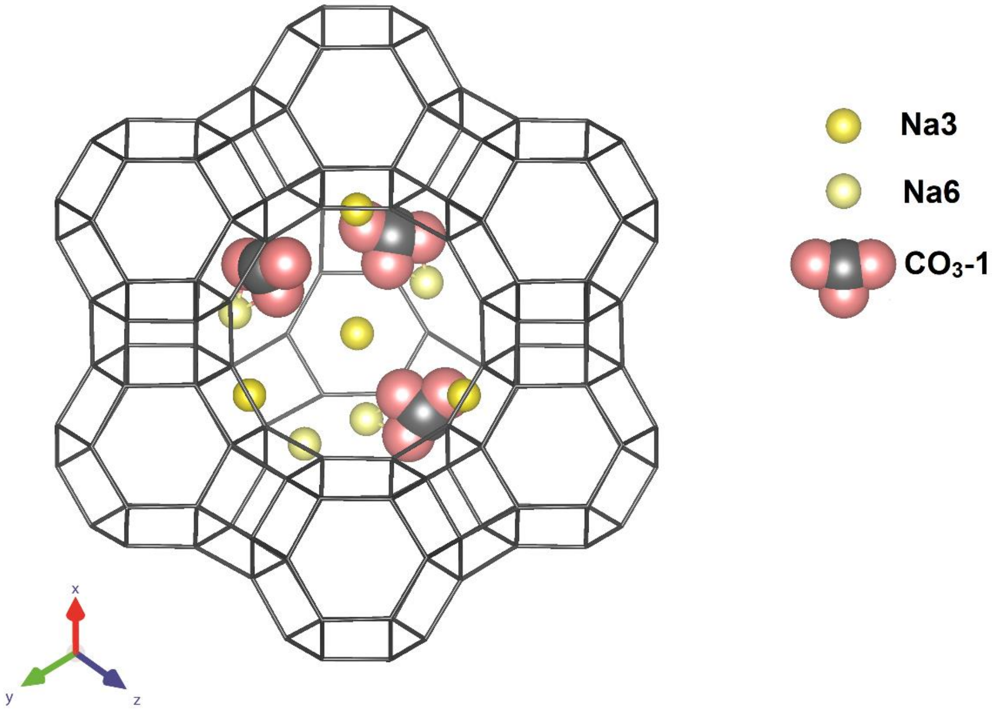

Figure 4.19: Extra-framework species location in Na-X-*AP* sample. View along the [111] direction. Only the Na sites in the supercage are shown. H_2O molecules are not shown for sake of clarity.

On the contrary, in the Na-Y-*CO₂* sample, the pumping seems to be more effective than in the Na-X-*CO₂*. The CO_2 content decreases more than a half, i.e., about 31 CO_2 molecules p.u.c. from the original 66 still remain in the zeolite porosities (figure 4.20). This is consistent with the fact that in the Na-Y-*CO₂* sample only physisorbed CO_2 molecules are present.

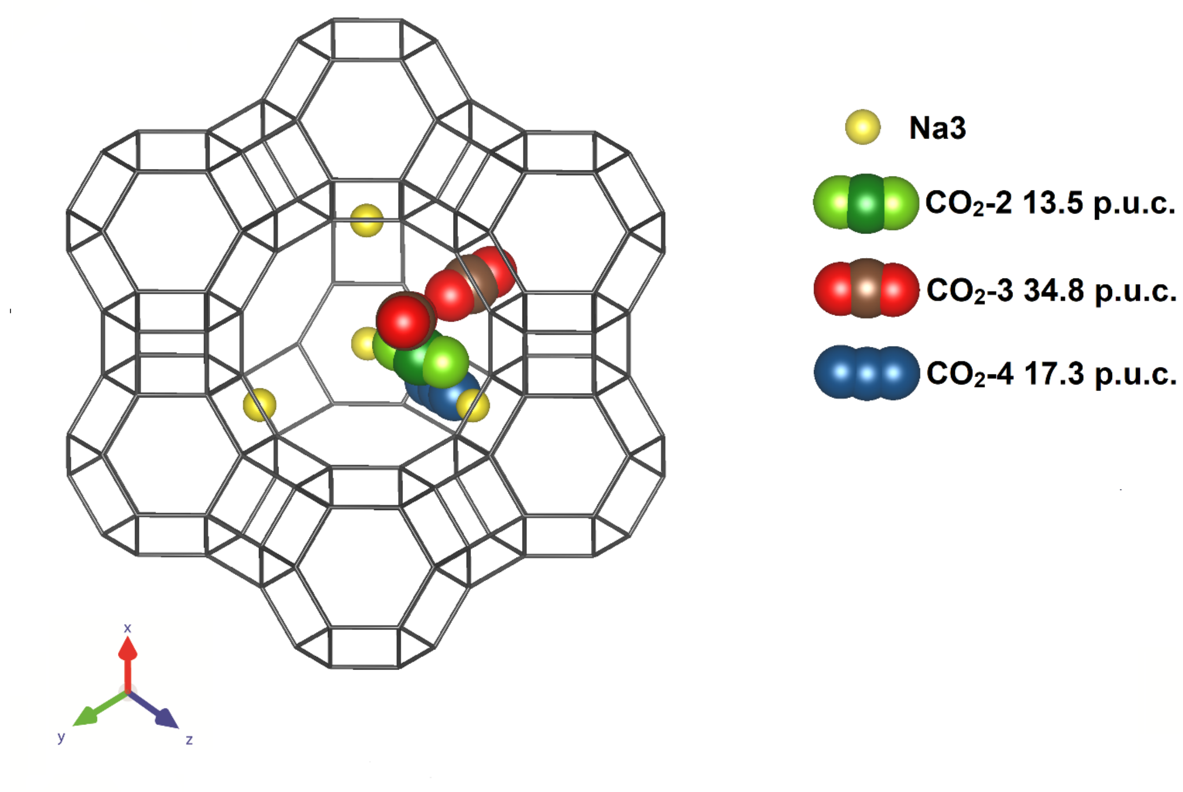

Figure 4.20: Extra-framework species location in Na-Y-*AP* sample. View along the [111] direction. Only the Na sites in the supercage are shown. H_2O molecules are not shown for sake of clarity.

4.5 *In situ* FTIR characterization

In order to obtain more information about the adsorption mechanism of CO_2 in both Na-X and Na-Y zeolites, the CO_2 adsorption (at *RT*) and desorption (at *RT* and 250 °C) were monitored by *in situ* FTIR spectroscopy (figures 4.21 and 4.22). In both cases, the absence of the band at 1627 cm^{-1} in the IR spectra of the activated samples counts for the successful removal of H_2O. Nevertheless, considering the results from the TG for sample Na-X (figure 4.5), we may expect the presence of some residual H_2O in the channels of zeolite at the activation temperature used (250 °C).

Upon exposing Na-X to excess of CO_2, new sets of bands appear which were not present in the IR profile of the activated sample (figure 4.21, table 4.3). The new band at 2352 cm^{-1} corresponds to CO_2 physically adsorbed on the zeolite, the broadening of the feature is explained by the presence of CO_2 excess in the gas phase (non-adsorbed form). As a consequence of the high CO_2 content, the ^{13}C isotope (natural abundance) in CO_2 is detected at 2285 cm^{-1}. On the other hand, bands arising between 1707 and 1366 cm^{-1} are attributed to the chemisorbed CO_2. These correspond to different types of carbonates due to the participation of framework oxygen atoms (table 4.3 and figure 4.21). These results are consistent with the report by Busca (2017) where bands are attributed to perturbed CO_2, bicarbonates, mono- and bi-dentate carbonates. Upon subjecting the samples to high vacuum desorption ($\sim 5 \cdot 10^{-9}$ bar) at room temperature, the band corresponding to physisorbed CO_2 (and CO_2 in gas phase) diminished drastically, while those corresponding to the chemisorbed CO_2 remained unchanged with the exception of the bands at 1484 and 1435 cm^{-1} (monodentate carbonates species) that slight increase. Such feature can result from the reaction of physisorbed CO_2 during evacuation. A quasi total desorption of CO_2 at 250 °C was achieved; the spectrum highly resembles that of the initially activated sample.

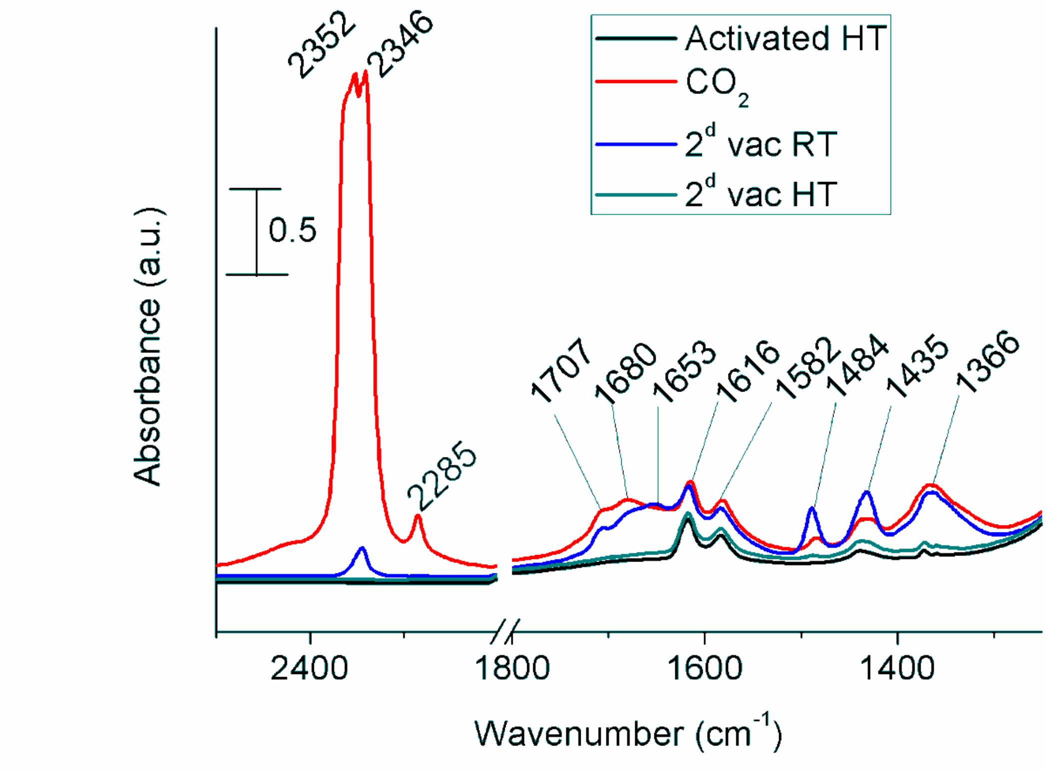

Figure 4.21. FTIR spectra of nanosized Na-X zeolite activated at 250 °C (black), after adsorption of 0.01 bar CO_2 (red), under secondary vacuum ($\sim 5 \cdot 10^{-9}$ bar) at room temperature (blue), and under secondary vacuum ($\sim 5 \cdot 10^{-9}$ bar) and at 250 °C (green).

Bands (cm^{-1})	Assignements	FTIR band area (a.u.)			
		Activated	CO_2	2^d vac RT	2^d vac HT
2352	Physisorbed CO_2	0	122.5	3.48	0
1707	CO_2 molecules Perturbed	0	5.15	3.16	0
1680 & 1366	Bicarbonates	0	27.83	25.10	1.13
1653	Residual acidity	0	7.35	9.98	0.49
1616	H_2O	0	3.28	3.10	0.16
1582	Bidentate carbonates	0	3.51	3.24	0.50
1484 & 1435	Monodentate carbonates	0	4.12	11.31	1.15

Table 4.3. FTIR bands and the corresponding assignments recorded for the Na-X nanosized zeolite initially activated and after adsorption of 0.01 bar CO_2. Residual acidity indicates acid sites which did not interact with CO_2.

The physisorbed CO_2 in Na-Y zeolite induces the formation of a band at 2354 cm^{-1} with a set of bands related to chemisorbed CO_2 observed between 1750 and 1300 cm^{-1} (figure 4.22, table 4.4). Unexpectedly, signals of bicarbonates were detected at 1681 and 1364 cm^{-1} despite the activation at 250 °C which is enough to eliminate the H_2O from the sample, as evidenced by TGA. One possible explanation for their presence is the reaction of incoming CO_2 with residual H_2O (not detected by IR) -available in the zeolite channels- or with the residual acid sites visible at 1653cm^{-1}.

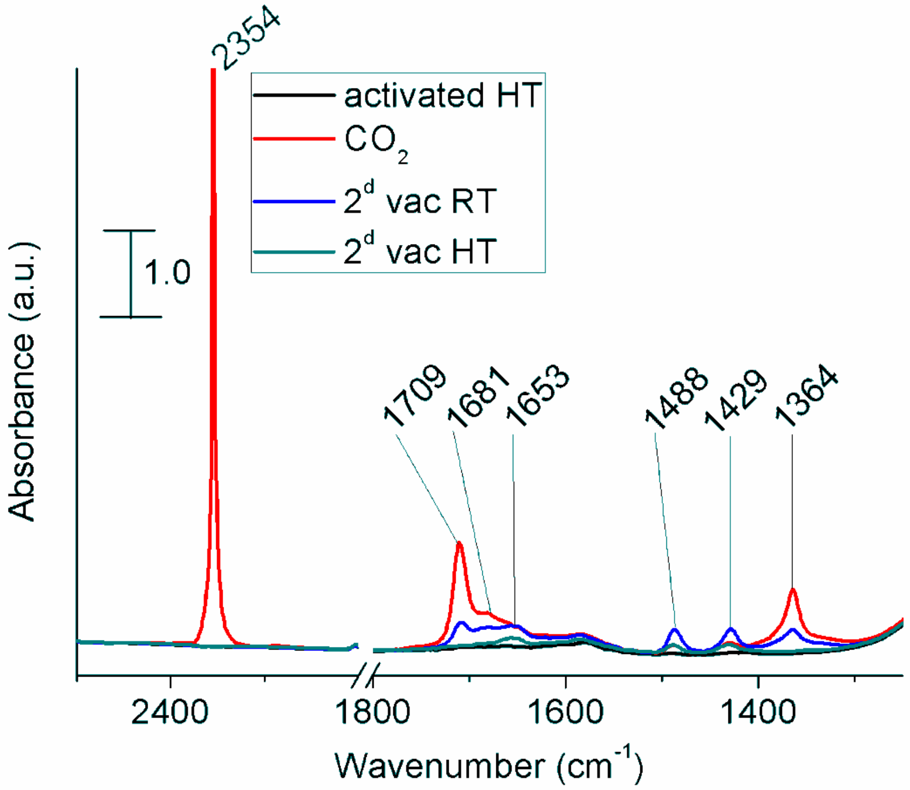

Figure 4.22. FTIR spectra of nanosized Na-Y zeolite under activation at 250 °C (black), after adsorption of 0.01 bar CO_2 (red), under secondary vacuum (~$5 \cdot 10^{-9}$ bar) at room temperature (blue), and under secondary vacuum (~$5 \cdot 10^{-9}$ bar) and activation at 250 °C (green).

A desorption behavior similar to Na-X was recorded for Na-Y at *RT*: the band corresponding to physisorbed CO_2 disappeared completely, chemisorbed CO_2 (perturbed CO_2 and bicarbonates) decreased significantly, while the bands corresponding to monodentate carbonates and residual acidity increased. As shown in figure 4.22 (green curve), an increase of the temperature up to 250 °C was required to almost fully desorb the chemisorbed CO_2. The latest spectrum (green) is very similar to that collected from the initially activated Na-Y (black), demonstrating the reversibility at high temperature of CO_2 sorption within the Na-Y nanosized zeolite with minor residual acidity maintained.

Bands (cm^{-1})	**Assignements**	**FTIR band area (a.u.)**			
		Activated	**CO_2**	**2^d vac RT**	**2^d vac HT**
2354	Physisorbed CO_2	0	34.86	0.15	0
1709	CO_2 molecules perturbed	0	16.97	4.69	0.22
1681 & 1364	Bicarbonates	0	16.92	8.43	0.53
1653	Residual acidity	0	3.48	5.35	1.69
1488 & 1429	Monodentate carbonates	0	1.94	6.33	0.83

Table 4.4: FTIR bands and the corresponding assignments recorded for the Na-Y nanosized zeolite initially activated and under adsorption of 0.01 bar of CO_2.

An interesting observation lies on the existence of bidentate carbonate in Na-X, but not in Na-Y. The lower Si/Al ratio of the Na-X sample induces a closer proximity of Al within the framework and the Na cations, and thus higher possibilities for the formation of bidentate species.

4.6 Discussion

Coupling of the two complementary techniques (XRPD and FTIR) adopted in this work, allowed to probe the CO_2 adsorption/desorption mechanisms at different levels, in particular, on the average structure by XRPD and on the local structure by IR. This approach allowed to appreciate a different behavior in adsorbing/desorbing of CO_2 by the two nanosized Na-Y and Na-X zeolites. The main differences are related to the amount of CO_2 molecules adsorbed and to their interaction with the zeolite framework and extra-framework species.

The results for Na-Y XRPD are consistent with the presence of physisorbed CO_2 molecules only, while IR results show even the presence of mono dentate carbonates formed after the interaction of framework oxygen atoms and bicarbonates, probably formed by the interactions with residual H_2O -that unintentionally reentered the zeolite channel- or residual acidic sites. The chemisorbed CO_2 species are probably present in a very low amount, that cannot be detected by X-ray diffraction. Regarding the nanosized Na-X zeolite, both physisorbed and chemisorbed species were detected by both the XRPD and IR techniques. In particular, XRPD indicates the presence of bicarbonate only, while IR detected even mono and bidentate carbonates.

Concerning the interpretation of the results relative to desorption, from the spectroscopic investigations, it appears that, while the physisorbed species are removed from the zeolites channel by pumping under secondary vacuum ($\sim 5 \cdot 10^{-9}$ bar) at room temperature, carbonates and bicarbonates remain in the pores and are completely removed under heating at 250 °C. On the contrary, from the XRPD it appears that both chemisorbed and physisorbed species are only partially removed from the porosity. The different behavior is due to different vacuum conditions of the two devices used in the experiments ($\sim 5 \cdot 10^{-9}$ bar for IR experiment *vs* $\sim 6 \cdot 10^{-7}$ bar for XRPD one).

The limits of the XRPD techniques and in particular of the Rietveld structural refinements on nanophases (Na-X crystals size ~20 nm) should be considered. In fact, despite the high-resolution of the synchrotron data collections, the determination of the exact number of molecules can be affected by large errors, further worsened by the presence of partially occupied crystallographic sites and by atoms with weak scattering factors.

Previous studies performed on this topic shed light on different factors that may influence the CO_2 adsorption in zeolites, finding that in addition to the structural and chemical features of the zeolite, other aspects must be considered (Bonenfant *et al.,* 2008). In particular, the carbonates/bicarbonates formation plays a key role during the carbon dioxide adsorption, in fact the presence of these species might decrease the accessibility of CO_2 molecules, limiting further adsorption and hindering the regeneration capacity in successive adsorption/desorption cycles (Angell and Howell, 1969; Busca, 2017). The formation of carbonates, in most of the cases, is associated with the presence of cations in the electrostatically less-shielded type III site, located in the FAU supercage, that occurs only in Na-X (Jacobs *et al.,* 1973). In our study the presence of carbonates/bicarbonates was evidenced in both Na-X and Na-Y samples from IR results, even if in very different amount.

The influence of H_2O in the CO_2 adsorption is of paramount importance, being water one of the key components in flue gas. The presence of H_2O molecules in the zeolite cavities during the CO_2 adsorption seems to favor the formation of bicarbonates species via hydroxyl group reaction (Siriwardane *et al.*, 2001; Bonenfant et al., 2008). Different behaviors in relation to H_2O content were also reported. Brandani and Ruthven (2004) observed that even small amounts of H_2O can inhibit the CO_2 adsorption on different cationic forms of zeolite X. Bertsch and Habgood (1963) suggest that the presence of small amount of pre-adsorbed H_2O greatly accelerates the rate of CO_2 adsorption, presumably by catalyzing the chemisorption step.

In our study the presence of H_2O molecules favors the formation of bicarbonates in nanosized Na-X zeolite. The small amount of bicarbonate found in the Na-Y should be due to the use of moist CO_2.

Two recent papers investigated -from the structural point of view- the CO_2 adsorption in micron-sized zeolite Y, using neutron (Wong-Ng *et al.,* 2013) and synchrotron X-ray (Arletti *et al.,* 2016) powder diffraction. In both papers only physisorbed CO_2 was determined, which it agrees with our work for the nanosized Na-Y. The discrepancies on the number of molecules found could be due to different pressure conditions used for the CO_2 adsorption and to the different crystal sizes of the samples studied. In fact, the nanosized zeolites analyzed in this work favored the adsorption leading to a higher CO_2 adsorption capacity.

Wong-Ng *et al.* (2013) found two crystallographically independent CO_2 sites, bonding the Na cations, in the supercage. Arletti and co-workers (2016) found the evidence of tetrameric clusters of CO_2 molecules connected by H_2O to the Na cations of adjacent FAU supercages. These clusters, even if placed in the same portion of the supercage, are different from that found in this work, consisting of three/five CO_2 molecules. This could be dictated by the higher quantity of molecules adsorbed in consequence of the higher CO_2 pressure applied in the present work. In both papers, a CO_2 molecule located in the supercage (O16-C15-O16 in Wong-Ng *et al.* (2013) and CO_2b in Arletti *et al.* (2016)) corresponds to the CO_2-4 molecule of this work. In addition, the position of the CO_2-3 molecule of this work, in the window between two supercages, almost corresponds to that reported by Wong-Ng (2013) (O12-C11-O13), but shifted of about 1.9 Å along the molecule axis.

4.7 Conclusions

In situ synchrotron X-ray powder diffraction and in situ FTIR were used to study the adsorption/desorption of CO_2 in two FAU zeolites with nanosized dimensions, one corresponding to zeolite Na-X (Si/Al=1.24) and the other to Na-Y (Si/Al=2.54). Rietveld refinements performed on the XRPD patterns showed that, in Na-X and Na-Y 29 CO_2/CO_3^{2-} and 66 CO_2 molecules p.u.c. were adsorbed, respectively. The structural refinement results are in line with the FTIR spectroscopy analysis, representing the presence of physisorbed CO_2 in both zeolites, while chemisorbed CO_2 was not detected in the Na-Y by XRPD probably as a consequence of the low amount. In the case of Na-X, on the contrary, the presence of the less-shielded Na6 cations in the FAU supercage, and of H_2O molecules, induces the formation of bidentate bicarbonate groups, identified by both XRPD and FTIR.

The release of adsorbed species under high vacuum treatment ($5 \cdot 10^{-9}$ bar) from the nanosized Na-Y zeolite, where the CO_2 is mainly physisorbed, is almost complete. On the contrary, for the nanosized Na-X the vacuum treatment induces the desorption of physisorbed CO_2 only, while the chemisorbed species remain trapped in the pores. Only high temperature treatment (above 250 °C) effectively removes the carbonates.

This experiment allowed to shed light on the CO_2 adsorption/desorption mechanism of FAU zeolites with nanosized dimensions and to compare these results with those of other micron-sized samples, largely studied in the last years by many research groups.

The samples analyzed in this work are suitable hosts for the CO_2 capture from an environmental point of view. Moreover, the possibility to obtain different ratio of physisorbed and chemisorbed CO_2 in the nanosized FAU zeolite crystals, make these materials suitable to be used for target carbon dioxide delivery in biological systems for biomedical applications, since has been demonstrated a release of physisorbed gases by zeolites in biological systems (Wheatley *et al.* 2006; Mintova *et al.* 2016).

5 CONFINEMENT AND CONDENSATION OF AMINO ACID MOLECULES IN Na-MORDENITE

5.1 Introduction

Amide bond formation is one of the most important reactions in organic chemistry. It plays a key role in biological systems growth and development, since the amide bond is the main chemical bond connecting amino acids together giving peptides and proteins (figure 5.1). Amide bonds are also present in several widely used drugs (Valeur and Bradley, 2009) and synthetic polymers with catalytic applications (Carrea *et al.*, 2005).

The synthesis of oligo/poly-amino acids with catalytic activity is among the most intriguing molecular challenges in industrial biotechnology. During the last years, novel chemical approaches to amide bond formation have being developed (Pattabiraman and Bode, 2011; Łukasik and Wagner-Wysiecka, 2014). The great demand of improved methods for the synthesis of amide/peptide functionality is due to the expensive and wasteful approach of the current synthesis strategies, that are not "atom economical", since great quantities of waste are generated (Constable *et al.,* 2007) and dozens of molecules are sacrificed just to form one amide bond (Coin *et al.,* 2007).

Furthermore, the polymerization of amino acids under abiotic conditions is one of the key topics at the base of the studies investigating the origin of life (Hazen, 2005). The condensation of molecular building blocks as amino acids to yield the first active biopolymers, during primitive Earth ages, is an intriguing question that nowadays still remains open, since these processes are thermodynamically disfavored in highly diluted water solutions. To overcome the competition between the condensation reaction and the hydrolysis of peptides (Rimola *et al.*, 2009), Bernal's (1951) crucial hypothesis suggested a prebiotic polymerization on minerals surface. Several works (Lambert, 2008; Gilliam and Jia, 2018) examined the possibility to adsorb and condensate amino acids on different mineral surfaces as silica (Sakhno *et al.,* 2019), titanium oxide (Martra *et al.,* 2014), iron oxides (Shanker *et al.,* 2012), clays (Fuchida *et al.,* 2014), layered double hydroxides (Erastova *et al.,* 2017) and layered precipitate minerals (Grégoire *et al.,* 2018).

At the end of '90s, a series of pioneering papers of J.V. Smith (1998) suggested the possibility that zeolites, thanks to their ordered porous framework, could have a potential key role in assembly organic species into polymers, taking advantage of a protective environment. The idea that zeolites contributed to the formation of biopolymers in prebiotic conditions, could be more plausible considering that in early Earth, silica-rich volcanic glasses should have been abundant and their crystallization into zeolites and feldspar should have been common as in actual continental basins (Smith, 1999).

Several papers studied the adsorption of amino acids within synthetic zeolite pores (Munsch *et al.*, 2001; Titus *et al.*, 2003; Krohn and Tsapatsis, 2006) in order to deepen the knowledge on separation processes and interactions between these organic species and the microporous materials.

The adsorption capability of zeolites has been tested on amino acids (Carneiro *et al.*, 2011) and nucleic acid bases (Baú *et al.*, 2012; Anzinelli *et al.*, 2016) also in prebiotic chemistry experiments, but polymerization reactions have not been taken into account.

The aim of this thesis work is to promote the condensation reaction of amino acids in a confined environment (i.e. the zeolite pores) by applying moderate pressures, so to realize a “zeolite + amino acid oligomers” hybrid material. The use of pressure to induce oligo/polymerization of amino acids has been already tested in shock experiments simulating comet impact (Bertrand *et al.*, 2009; Sugahara and Mimura, 2015). High temperature/high pressure experiments, simulating the diagenetic and metamorphic processes occurring on Earth have been tested as well (Ohara *et al*., 2007; Otake *et al*., 2011; Furukawa *et al*., 2012). In all these experiments the peptide polymerization was limited to the formation of cyclic species or linear oligomers composed by few units.

The thesis rises from the idea that the coupling of a high-pressure regime with geometrical confinement, provided by a 1-D zeolite framework, could drive the formation of linear arrays of peptides.

In the present study, glycine, α-alanine and β-alanine amino acids were chosen for the polymerization experiments as they are the simplest amino acids, and since they represent the reference molecules in several experiments and theoretical investigations on amino acids adsorption onto mineral surfaces (Lambert, 2008). Moreover, these amino acids are the main products of the fundamental Miller experiment (Miller, 1953) on organic synthesis that occurred in Earth’s primitive atmosphere and ocean under influence of electrical discharge and sun radiation.

Na-mordenite (MOR framework-type), characterized by a mono-dimensional channel system, with 12 membered-ring channels running along the *c* axis, has been selected as a good candidate for our scope. Although a natural mordenite sample would have been more appropriate for simulating an Earth environment, a synthetic Na-MOR sample was chosen in order to simplify the system in the initial stage of this research. The Na cations located in the side pocket of Na-MOR are expected to trap the H_2O molecules possibly generated by the formation of the peptide bond during the condensation reaction.

The mordenite/amino acid hybrid realization was followed with a series of in situ technique and the resulting material was characterized by a multi-technique approach at ambient condition.

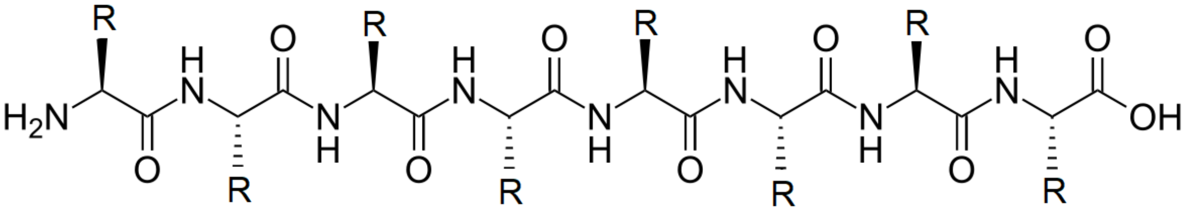

Figure 5.1: Example of poly-peptide molecule

5.2 Materials

5.2.1 MOR type zeolite

The MOR type zeolites have topological symmetry *Cmcm*. The natural mordenite has the following idealized cell parameters: a= 18.256 Å, b= 20.534 Å, c= 7.542 Å and V= 2827.3 Å^3 (http://europe.iza-structure.org/IZA-SC/ftc_table.php). The framework density of the MOR structure is 17.2 T/1000 Å^3. The building unit constituting the MOR structure is the *t-tes* (figure 5.2).

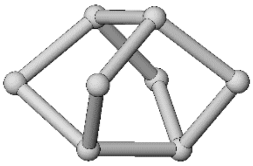

Figure 5.2: *t-tes* composite building unit of MOR framework type

Mordenite structure was resolved by Meier in 1961. The framework can be described as the combination of 5-1 SBUs. More in detail, the MOR framework can be built up from the assembly of puckered sheets formed by 6-membered rings parallel to the (100) plane, which define the perfect (100) cleavage. The sheets are linked together by 4-membered rings. The resulting structure is characterized by two channel systems parallel to the crystallographic *c* axis. One is a 12MR channel and presents side pockets on the channel walls in the [010] direction. The side pockets connect the 12-ring channel -through 8-membered rings- with the 8MR channel parallel to the first one (Gottardi and Galli, 1985; Martucci *et al.*, 2003). MOR framework is shown in figure 5.3 along the [001] direction and along the [010] direction.

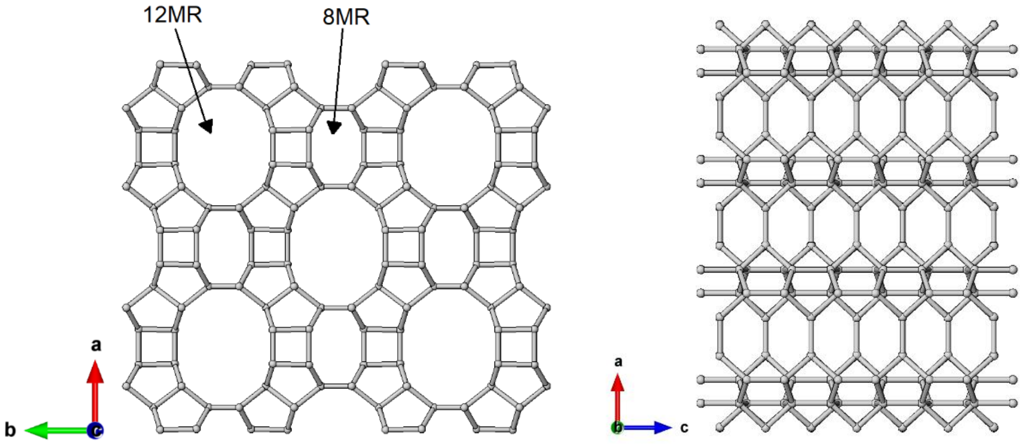

Figure 5.3: MOR structure along the [001] direction (left) and along the [010] direction (right).

The 12MR channel diameters reported by Baerlocher *et al.* (2007) are 7.0 Å and 6.5 Å, while the 8MR channel diameters are 5.7 Å and 2.6 Å, as shown in figure 5.4.

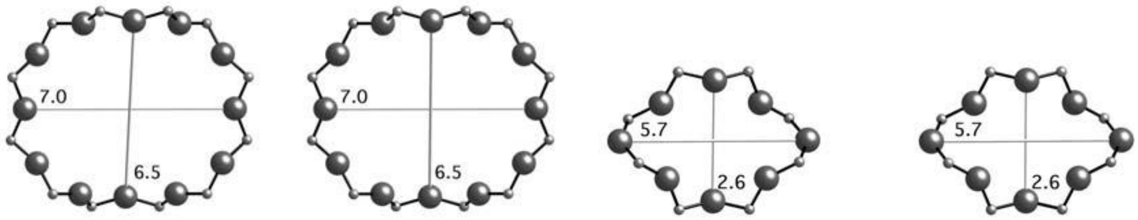

Figure 5.4: 12MR and 8MR channels diameters. View along the [001] direction. (Figure from Baerlocher *et al.*, 2007).

As previously mentioned, the symmetry of mordenite is *Cmcm*, as the systematic absences in diffraction data are consistent with this s.g., but several authors (Alberti *et al*., 1986; Simoncic and Armbruster, 2004) suggested a symmetry lowering to the s.g. $Cmc2_1$, due to the acentric extraframework cations distribution and to prevent the energetically unfavorable 180° T-O-T angle, due to the position of the O8 oxygen on an inversion center.

The idealized chemical composition of a natural mordenite is $Na_3KCa_2Al_8Si_{40}O_{96}·28H_2O$. The Si/Al ratio ranges from 4.3 to 6.0 (Coombs *et al.*, 1997), while synthetic MOR can be prepared in a wider range, from 5.0 to 16.0 by direct synthesis (Kim and Ahn, 1991) or with an even higher Si/Al ratio following a dealumination process. Concerning the Si/Al distribution, several authors (Gottardi and Galli, 1985; Alberti *et al.*, 1986) reported a small, but definite, Al-enrichment in the 4-rings which connect the hexagonal sheets, in that the tetrahedra of these 4-rings are little larger than those in the sheets. Takaishi and co-workers (1995) formulated a new rule, complementary to the Löwenstein's rule, concerning the Al distribution in the mordenite framework. This rule states that none of the five-membered rings of the framework can contains two Al atoms. According to this rule, the possible configurations of Al distribution in Al-rich mordenites are very limited, and the maximum number of Al atoms in the framework, when both the Löwenstein's rule and the 2Al/5-ring avoidance rule are satisfied, is 8 (Kato *et al.*, 2003).

The cation sites in MOR were coded by Mortier *et al.* (1982). These authors describe three main cation sites: site A inside the 8MR channel, near the center of the 8-ring which connects the 8MR channel with the side pocket, site D close to the center of the 8-ring connecting the side pocket with the 12MR channel, and site E in the 12MR channel, far from the 4-rings. These crystallographic sites are preferred by most of the cations (figure 5.5).

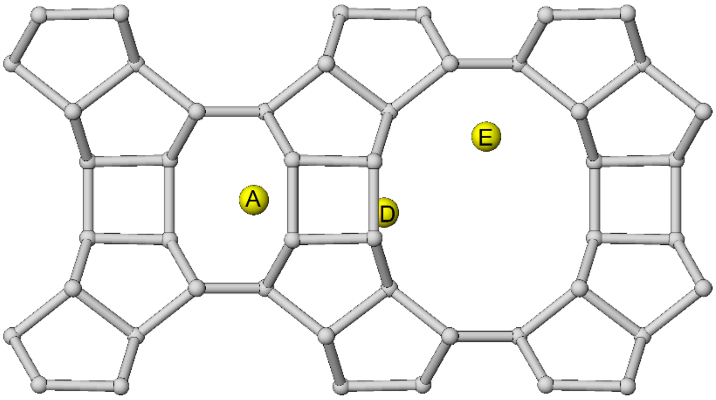

Figure 5.5: Cations location in MOR structure.

5.2.2 Na-MOR sample

Na-MOR used in this thesis was synthesized at Institut Charles Gerhardt Montpellier following the procedure standardized by Hamidi *et al*. (2004) starting from a precursor gel of composition $6Na_2O/Al_2O_3/30SiO_2/780H_2O$, prepared by mixing a suspension of precipitated silica Zeosil175MP with an alkaline solution of sodium aluminate. The gel was sealed in an autoclave and the crystallization was carried out at 160 °C for 72 hours.

5.2.3 Amino acids

Amino acids are the building blocks of proteins, which are of primary importance for the continuing functioning of life, being proteins the catalysts of most of chemical reactions occurring in the cells. Amino acid molecules are constituted by an amino group ($-NH_2$), and a carboxyl group (-COOH), along with a side chain (R group) specific of each amino acid. About 500 naturally occurring amino acids are known and can be differently classified, for example according to the location of core structural functional groups inside the molecule (alpha (α-), beta (β-), gamma (γ-) or delta (δ-) amino acids).

As discussed in the Introduction, three different amino acids were used for the loading experiments of this thesis project: glycine, α-alanine and β-alanine. These were chosen because they are the simplest amino acids and the reference molecules in several experiments and theoretical investigations addressing the origin of long complex molecules and the origin of life on the primordial Earth (Lambert, 2008).

Glycine: glycine (figure 5.6) is the simplest amino acid, with just a single hydrogen atom as its side chain (R group). The chemical formula is NH_2CH_2COOH. Glycine is a non-chiral molecule and one of the proteinogenic amino acids. The material occurs as white crystalline powder.

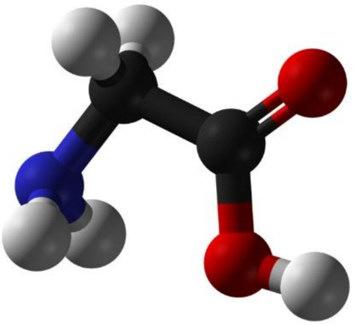

Figure 5.6: Glycine molecule (C atoms in black, O atoms in red, N atom in blue, H atoms in white).

α-alanine: is an aliphatic amino acid, it means that the amino group, the carboxyl group and the R group are all attached to the central carbon atom (α-carbon), (figure 5.7). The R group of alanine is a methyl group. The chemical formula is NH_2CHCH_3COOH.

Alanine is the simplest α-amino acid after glycine, its methyl side chain is non-reactive and is therefore hardly ever directly involved in protein function. The L-isomer of alanine (left-handed) is the one incorporated into proteins and is one of the most abundant. The material occurs as white micro-crystalline solid.

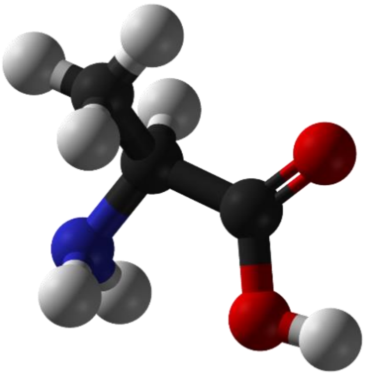

Figure 5.7: L-α-alanine molecule (C atoms in black, O atoms in red, N atom in blue, H atoms in white).

β-alanine: is a naturally occurring β amino acid. In this amino acid, the amino group is in β position respect to the carboxylate group (figure 5.8). The chemical formula is the same of α-alanine, but unlike its counterpart α-alanine, β-alanine has no stereocenter. The material occurs as white micro-crystalline solid. This amino acid is not found in any major proteins or enzymes, but it is a component of several naturally occurring peptides.

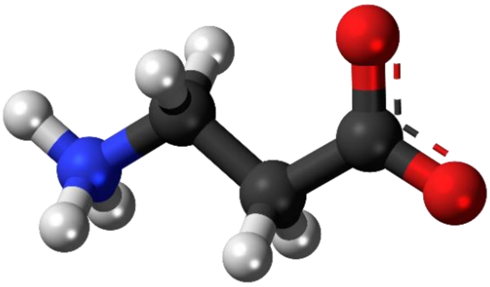

Figure 5.8: β-alanine molecule in Zwitterionic form (C atoms in black, O atoms in red, N atom in blue, H atoms in white).

5.2.4 Amino acid loaded samples

The three types of amino acids were loaded in two different methods inside the mordenite sample, by adsorption from vapor phase and by adsorption from aqueous solution. Vapor loading resulted to be not effective in the case of α-alanine since, as demonstrated by IR monitoring the amino acid did not penetrate the zeolite pores.

Loading from vapor phase. With this method were realized the samples **Na-MOR+gly** and **Na-MOR+βala:** The Na-MOR sample was preliminary activated at 500 °C in 10 mbar of O_2 for 1 hour, in order to completely remove water. The amino acids crystals were sublimated at 150 °C for 8 hours inside a vacuum tube together Na-MOR powder (figure 5.9). IR monitoring during the loading showed no variation in the intensity signal of the amino acid within the loaded sample for time higher than 8 hours. After the preparation, all the samples were held under controlled Ar atmosphere in a glove-box to avoid sample rehydration. The vapor loading for the α-alanine was tested, but this method was not effective for this type of amino acid and no trace of adsorbed molecule was detected on the sample.

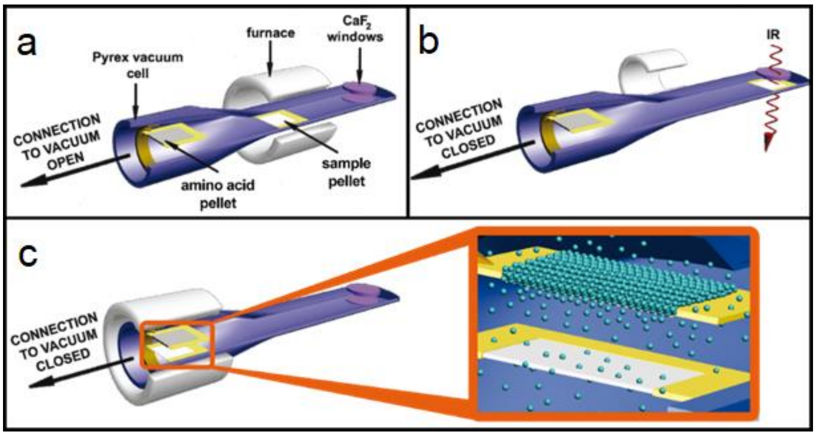

Figure 5.9: Pictorial representation of the setup used for the vapor phase amino acid loadings. The quartz tube is used for both the initial MOR activation (a) and the subsequent amino acid sublimation (c) by putting the pellets close to each other. The IR spectra are collected in the bottom part of the tube (b) where the infrared beam passes through CaF_2 windows.

Loading from aqueous solution. With this method were realized the samples **Na-MOR+gly_w** and **Na-MOR+αala_w:** The amino acid adsorption from aqueous solution was accomplished by the Selective Adsorption method. The loading was performed soaking 100 mg of Na-MOR powder in 1 ml of a 1 mM amino acid solution in ultrapure water and stirred for 48 hours. The sample was then centrifuged for 10 minutes at 10 kRPM and dried overnight at 80 °C. Finally, the sample was kept in vacuum at 200 °C for 1 hour to obtain H_2O removal. This was the highest reachable temperature avoiding the amino acid degradation. After the preparation, all the samples were held under controlled Ar atmosphere in a glove-box to avoid sample rehydration.

5.3 Experimental methods

The amino acid loaded Na-MOR samples were characterized by a multi-technique approach: X-ray powder diffraction (XRPD), Infrared spectroscopy (IR), thermogravimetric analysis (TGA) and elemental analysis. Successively, the hybrids were studied under pressure by XRPD in situ synchrotron experiments -using both penetrating and non-penetrating pressure transmitting media (PTM)- and by in situ HP Raman spectroscopy -using a non-penetrating PTM- in order to shed light on the amino acid behavior in a confined environment under pressure. Furthermore, two hybrid synthesis experiments at HT/HP in a large volume cell were performed. All the experimental conditions are described in the next pages. In table 5.1 are indicated which techniques were used to analyze the different samples.

sample	TGA	MS-EGA	Elemental A.	IR	XRPD P_{amb}	XRPD HP Daphne	XRPD HP Ar	Raman HP
Na-MOR	X			X	X			
Na-MOR+gly	X	X	X	X	X	X	X	
Na_MOR+gly_w								X
Na-MOR+αala_w	X	X	X	X	X	X	X	
Na-MOR+βala	X		X	X				
Na-MOR+βala_w								X
Na-MOR+gly_LV				X				
Na-MOR+βala_LV				X				

Table 5.1: Characterization techniques used for the different samples (LV indicates large volume synthesis samples).

5.3.1 XRPD Experimental conditions

As synthesized Na-MOR characterization

The synchrotron XRPD pattern of as synthesized Na-MOR was collected at ID15 beamline at ESRF. The sample was loaded in a 0.3 boron capillary and a monochromatic beam with a wavelength of 0.412 Å was used. Data were acquired in Debye Scherrer geometry on a MAR2560 detector, with a sample-detector distance of 547 mm. LaB_6 was used as a standard to calibrate wavelength, sample to detector distance, and tilting angle of the detector.

Hybrids characterization

Both ambient and high pressure (HP) XRPD experiments on two samples (Na-MOR+gly and Na-MOR+αala_w) were performed at ID27 beamline of ESRF (figure 5.10a and 5.10b), using a wavelength of 0.3738 Å. For Na-MOR+βala sample, no structural characterization is reported since it has not been possible to measure it.

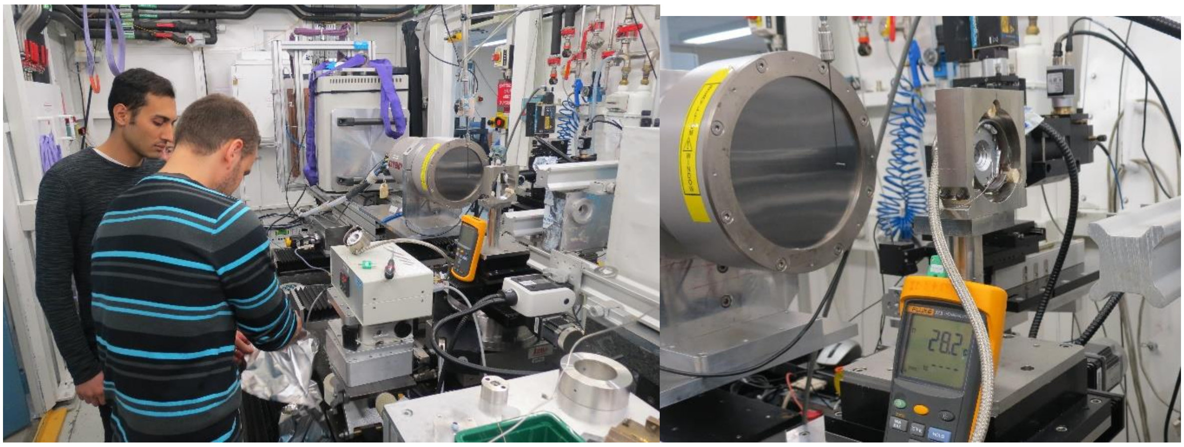

Figure 5.10a: Left, ID27 beamline experimental hutch; 5.10b: Right, DAC positioned in sample stage and detector MAR2560.

The two amino acid-loaded samples Na-MOR+gly and Na-MOR+αala were held under controlled Ar atmosphere in a glove-box to avoid sample rehydration for the whole experiment. The ambient condition data collections were performed after packing and sealing the powders in boron capillaries. For HP experiments, the samples were loaded in a membrane diamond anvil cell (DAC), using both DAPHNE oil as non-penetrating PTM (DAC loading performed inside a glove box with a controlled Ar atmosphere) and cryo-loaded argon as penetrating PTM (DAC loading using a high-pressure gas-load device located in the ESRF laboratories).

The pressure investigated in the different experiments are reported in Table 5.2.

Na-MOR+gly	DAPHNE	**P_{amb}**	0.44	1.02	1.57	2.06	2.7	1.68 R	1.1 R	**P_{amb}R**
	Ar	0.07	0.36	0.92	1.43	1.29 R	0.76 R	0 R		
Na-MOR+αala	DAPHNE	0.59	0.85	1.2	1.88	2.48	3.02	1.9 R	0.18 R	
	Ar	0.1	0.32	0.79	1.1	1.46	1.77	2.13	P_{amb}R	

Table 5.2: Pressure (GPa) steps in the different HP experiments. "R" indicates steps upon pressure release. In bold the data collections for which structure refinement was performed.

In the HP experiments performed in Ar, the crystallization of Ar was detected from above 1GPa. Pressure was calibrated using the ruby fluorescence method (estimated error 0.05 GPa), (Mao *et al.* 1986). All diffraction patterns were recorded on a MAR165 detector placed at 196 mm from the samples. The one-dimensional diffraction patterns were obtained in the 2θ range 0-21° by integrating the bi-dimensional images with the software DIOPTAS.

5.3.2 XRPD data analysis

As synthesized Na-MOR structure refinement

The *Cmc2₁* s.g. was adopted for all the refinements, to facilitate the location of the H_2O molecules and amino acid molecules within the MOR channels, so avoiding symmetry related problems. The starting model for the refinement of the as-synthesized Na-MOR was taken from Simoncic and Armbruster (2004). In this paper the structure of mordenite is refined in *Cmc2₁* s.g. from single crystal data and it is described by two structural domains shifted by *c*/2 as a consequence of framework defects and crystallographic faulting (the concentration of the defect domain is about 3%). In order to simplify the system, and to allow the refinement from powder data, only the predominant domain described by Simoncic and Armbruster (2004) was used for Na-MOR. In this model, the position of the framework atom O8, on an inversion center in the *Cmcm* s.g., is split into four closely spaced (ca. 0.5 Å) positions, with site-occupancy 0.25 each.

Hybrids structure refinement

For the Na-MOR+gly sample the as synthesized Na-MOR structure was used as starting model. The positions of H_2O and glycine molecules were derived from the difference Fourier map. The structural model -resulting from the Rietveld refinement- of Na-MOR+gly at ambient condition was used to refine the HP data. The quality of the XRPD pattern collected in DAC allowed to perform structural refinements only in the first step (ambient pressure) and the last step (ambient condition after pressure release). Only the unit cell parameters were obtained for the other pressure steps.

Concerning Na-MOR+αala, the presence of unwanted H_2O within the pores together with the amino acid, did not allow to make reliable structural refinements. LeBail method (Le Bail, 2005), was adopted to get the unit cell parameters evolution upon compression.

A pseudo-Voigt profile function was used for peaks fitting, the peak intensity cut-off was set to 0.001 of the peak maximum. The background was fitted by a Chebyshev polynomial with 21 coefficients for the P_{amb} refinement and 33 coefficients for the high-pressure refinements. Soft constraints were imposed on the tetrahedral bond lengths T-O (1.63 Å) for all the structure refinements and on the glycine molecule C-C (1.52 Å), C-O (1.25 Å), C-N (1.48 Å), O-O (2.2 Å). Lattice parameters and refinement details of the four structural refinements performed are presented in table 5.3. Atomic coordinates and bond distances are reported in tables T3 and T4 in appendix. Observed and calculated patterns after Rietveld refinements are reported in Figure S2a−d.

	Na-MOR	Na-MOR+gly	Na-MOR+gly_P$_{amb}$	Na-MOR+gly_P$_{amb}$R
R F^2	0.152	0.097	0.12	0.17
a (Å)	18.0801(5)	18.075(1)	18.080(1)	18.075(2)
b (Å)	20.3795(4)	20.350(1)	20.348(1)	20.337(2)
c (Å)	7.4886(2)	7.4912(4)	7.4908(4)	7.4877(6)
V (Å^3)	2759.3(1)	2755.5(3)	2755.9(4)	2752.4(6)
observations	4332	2167	1952	1963
variables	148	146	151	151

Table 5.3: Lattice parameters and Rietveld refinement figures of merit (R F^2) for the Na-MOR and the Na-MOR+gly in capillary, inside the DAC at P$_{amb}$ and inside the DAC after pressure release.

5.3.3 IR spectroscopy

The infrared spectra were collected on a Bruker IFS 28 instrument equipped with a Globar source and a La-DTGS or MCT detector, averaging 100 scans (4 cm^{-1} resolution) to attain a good signal to noise ratio. The sample powder is compressed into a self-supporting pellet (ca. 10 mg/cm^2), hold by a goldframe and loaded into a quartz traditional IR cell. The cell can be connected to a vacuum line (residual pressure 10^{-4} mbar) for the removal of atmosphere and contact with vapors and gasses.

Isotopic exchange H/D is performed by contacting a previously outgassed sample with D_2O vapor pressure, then removing the excess by further outgas, completing an exchange cycle. These contact/outgas cycles are repeated until spectral invariance (typically 5-10 cycles). IR spectra were collected for Na-MOR, Na-MOR+gly, Na-MOR+αala_w and Na-MOR+βala samples.

5.3.4 HP Raman spectroscopy

The *in situ* HP Raman experiments were performed in reflection mode using a green laser (wavelength 532 nm). Two different in situ HP experiments were carried out with the glycine and a β-alanine loaded samples. The Raman signal collected on the vapor loaded samples (Na-

MOR+gly and Na-MOR+βala) was hidden by fluorescence signal of the MOR, making difficult the interpretation of the patterns. Two data sets of two experiments are shown in the next pages, both experiments were performed on samples loaded by aqueous solution with glycine and β-alanine, Na-MOR+gly_w and Na-MOR+βala_w, respectively. Fluorinert FC77 was used as non-penetrating PTM. This fully-fluorinated liquid (all H atoms are replaced by F atoms) was used in order to avoid the presence of C-H stretching signal in the spectra due to the medium. The Na-MOR+gly_w was compressed up to 3.4 GPa in four steps and one other step was collected during pressure release. The Na-MOR+βala_w sample was compressed up to 3.5 GPa in four steps and other three steps were collected during pressure release.

5.3.5 Large volume synthesis

Large-volume synthesis using a high-pressure bomb device were carried out at the Physics Department of the University of Montpellier. These experiments were carried out in order to test the behavior of the hybrids at high pressure in presence of an excess of amino acid in vapor phase (i.e. to evaluate possible polymerization induced as a consequence of the pressure of the vapor in the cells). Two experiments were prepared, one with glycine and the other one with β-alanine. The dehydrated Na-MOR powder and amino acids crystals (¾ in volume of mordenite and ¼ of amino acid crystals in both experiments) were grinded together and loaded in a threaded Teflon lined capsule (15mm length and 6mm of diameter) inside a glove box. The capsule was mounted inside a furnace (figures 5.11 a and b) and placed in the pressure bomb, Unipress 3-stage gas compressor, connected through a capillary system with a piston cylinder (figures 5.12 a and b) using He gas as pressure medium.

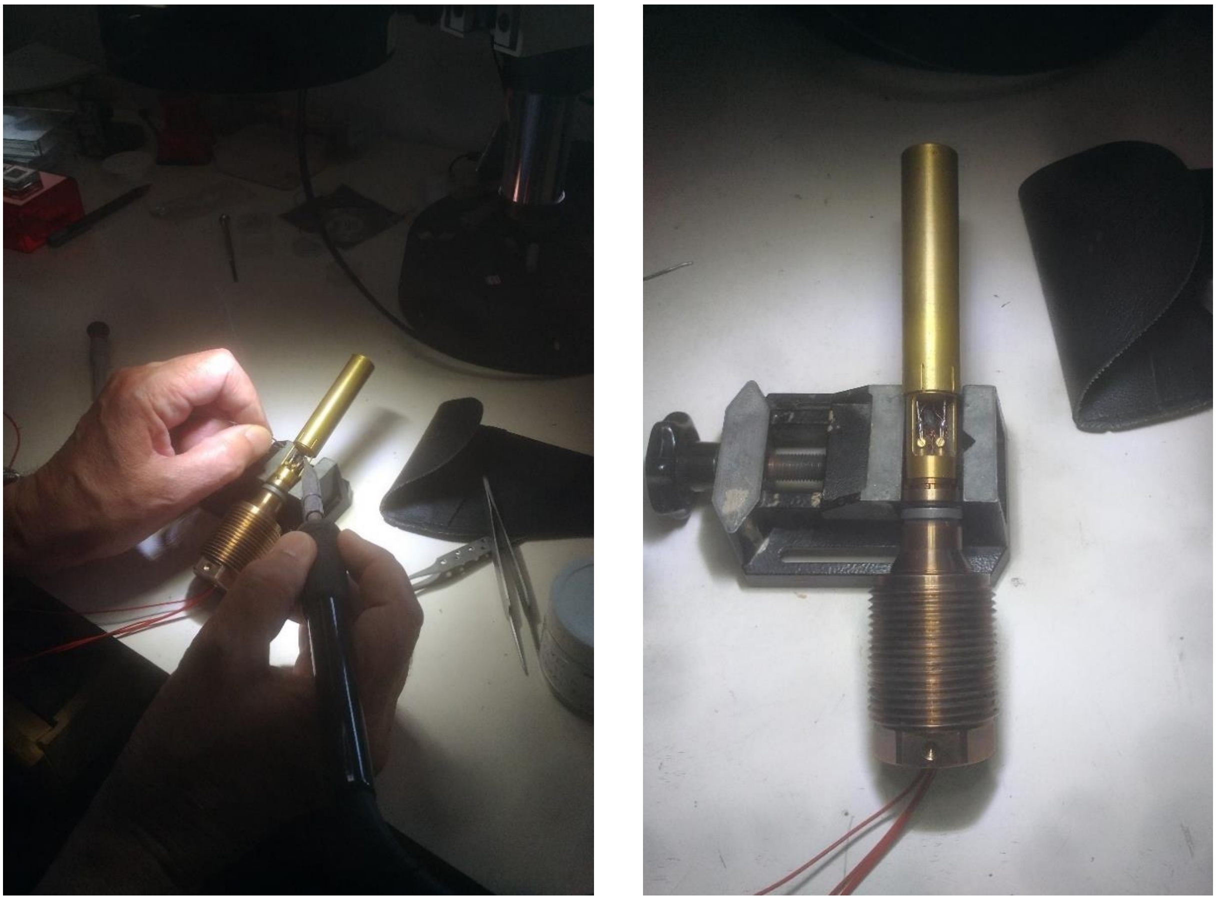

Figure 5.11 (a and b): Furnace containing the threaded Teflon lined capsule for the large-volume HP experiment.

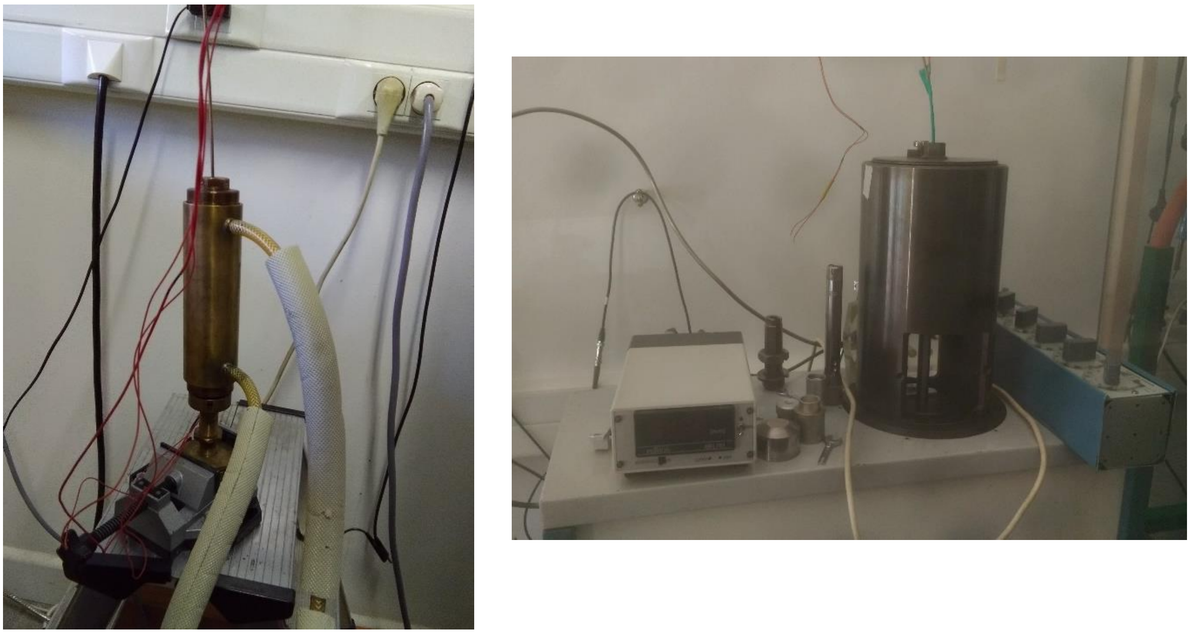

Figure 5.12: (a, left) Pressure bomb. (b, right) Piston cylinder.

The Na-MOR+gly_LV experiment was conducted in the following conditions: pressure was kept at 15 MPa, while the temperature was increased up to 150 °C. After 20 minutes pressure was slowly increased up to 440 MPa, while the temperature oscillated in the range 145-155 °C. After 2 hours in this condition the temperature and the pressure were brought back to ambient conditions.

In the Na-MOR+βala_LV experiment, the pressure was kept stable at 15 MPa, while the temperature was increased up to 150 °C. Again, after 20 minutes, the pressure was slowly increased up to 290 MPa, while the temperature oscillated in the range 145-155 °C. After 2.5 hours in this condition the temperature and the pressure were brought back at ambient conditions. The samples were recovered and characterized by IR spectroscopy.

5.4 Results and discussion

5.4.1 Na-MOR sample characterization

TGA

Figure 5.13 shows the TG and DTG curves of Na-MOR. The total weight loss is 14.6%. Most of the loss (14%) occurs below 400 °C and corresponds to 27 H_2O molecules p.u.c.

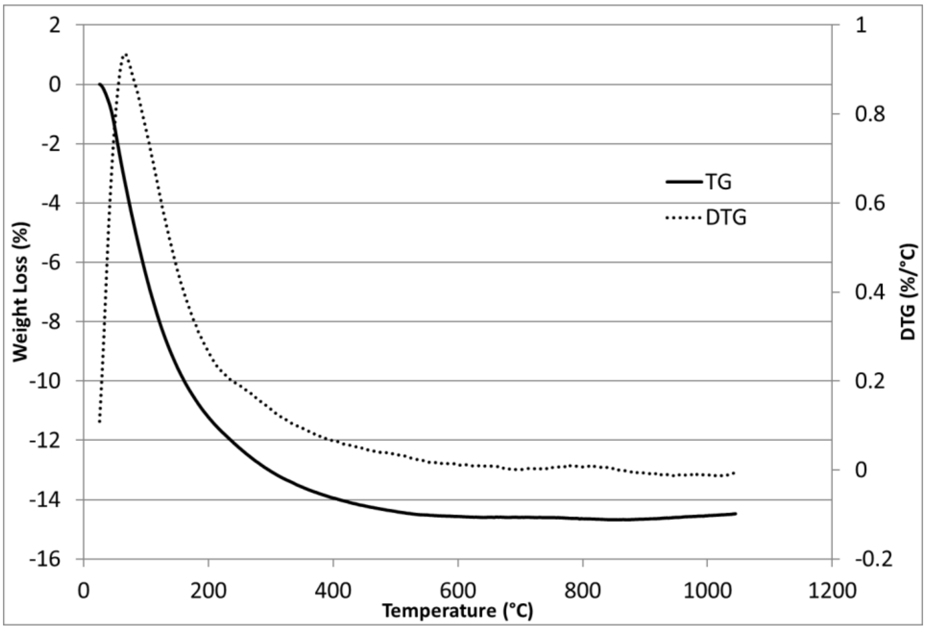

Figure 5.13: TG and DTG curves of Na-MOR sample.

SEM

SEM images of Na-MOR are reported in figure 5.14. The crystals show a flat morphology with ogive shape. The average crystal size is about 10 µm.

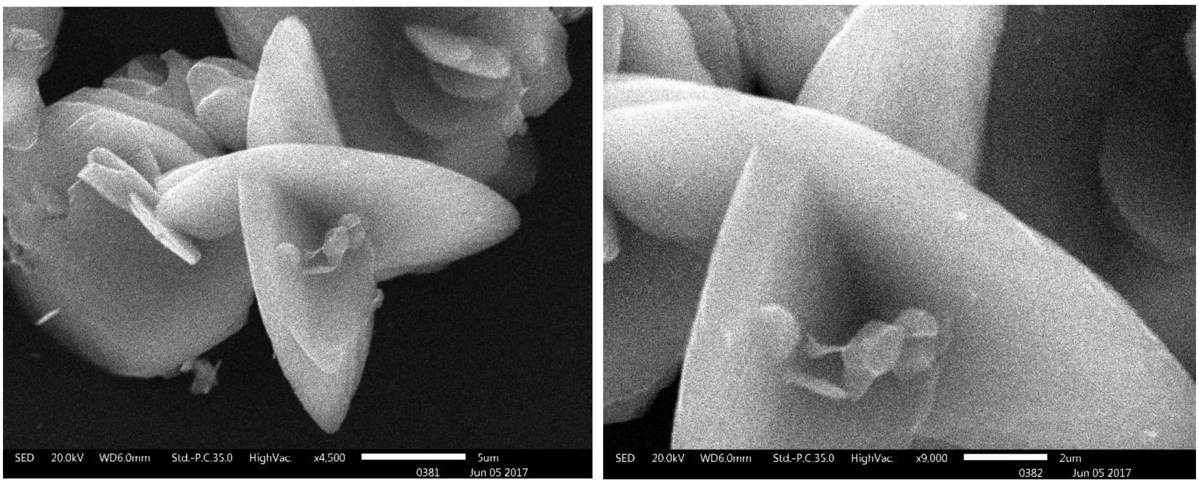

Figure 5.14: SEM images of Na-MOR.

Structural refinement

Rietveld refinement details and unit cell parameters of Na-MOR sample are reported in table 5.2, while atomic coordinates and bond distances are reported in tables T3a and T4 in appendix. Concerning the framework, the T-O distances show average bonds longer than 1.63 Å for the tetrahedral sites T3 (1.66 Å) and T4 (1.68 Å). Previous works (Martucci *et al.*, 2000; Takaishi *et al.*, 1995) suggested an Al-enrichment in the four-rings connecting the hexagonal sheets, in the same sites (T3 and T4, figure 5.15) the structural refinement suggesting a higher concentration of Al. This assumption agrees with the fact that the oxygen atoms bonded to the Na1 and Na3 cations belong to these two tetrahedra (see below).

On the basis of the distances and occupancy factors of the refined extraframework sites, two Na^+ cation sites are located in the unit cell: i) Na1, placed at the center of 8MR channel and coordinated by six framework oxygens and two H_2O oxygens, and ii) Na3, located in the site D (Mortier *et al.*, 1982), in the 8MR window between the 12MR channel and the side pocket, slightly shifted from the (100) plane (figure 5.15) and coordinated by six oxygen atoms (three framework oxygens and three H_2O oxygens). On the basis of the refined occupancy factors, the total amount of Na is 4.9 atoms p.u.c.

H_2O molecules are located in seven crystallographic independent sites: W1 in the 8MR channel, coordinated to Na1; W6 inside the side pocket coordinated to Na3; and five further H_2O molecules (W2, W3, W4, W7 and W10) in the 12MR channel forming a hydrogen bonded cluster, with interatomic distances ranging between 2.50 and 3.16 Å (table T5 in appendix). W1, W3 and W4 are also in weak interaction with framework oxygen atoms. The total amount of H_2O is 26.6 molecules p.u.c., in perfect agreement with the TG results.

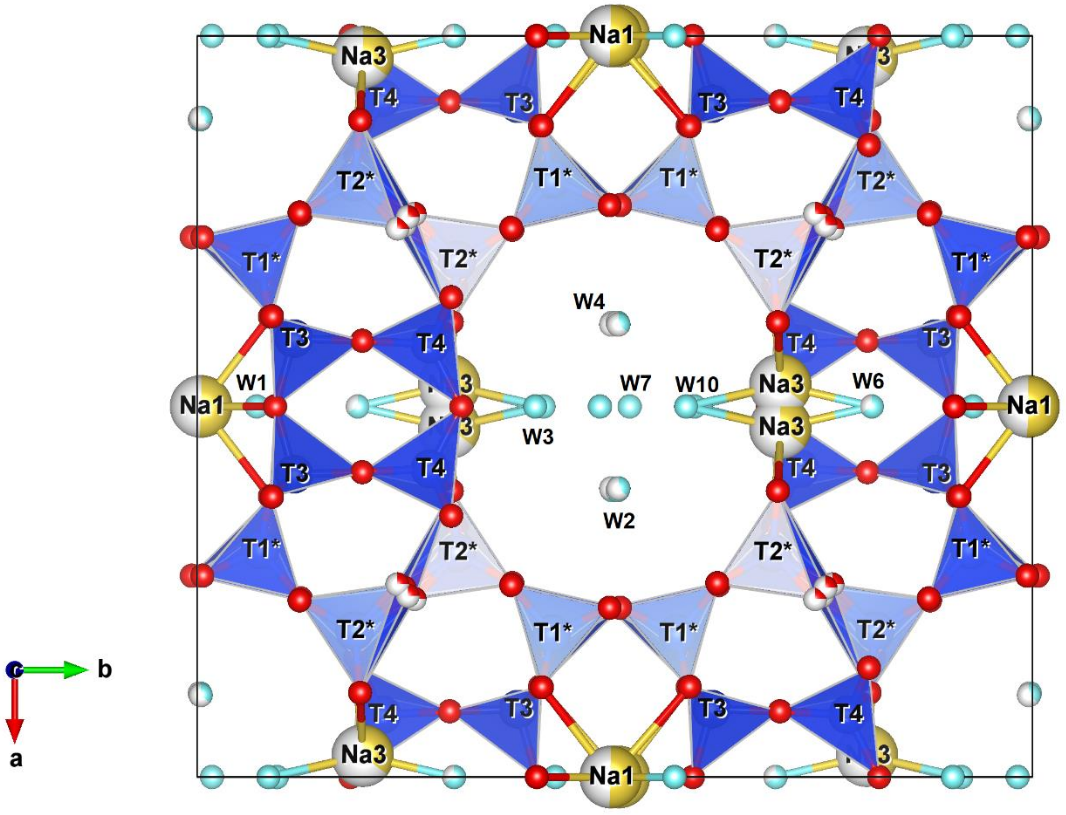

Figure 5.15: View along [001] of the as synthesized Na-MOR structure. T sites with "*" indicate the positions generated by symmetry lowering from *Cmcm* space Group.

The structural determination of the as synthesized Na-MOR indicates that, on the basis of the position of the Na cations, this zeolite seems a good candidate for the condensation of the amino acids, since, once dehydrated the zeolite, in the 12MR channels there is room enough to host a peptide polymer.

IR spectroscopy

The hydration state of Na-MOR was studied also by IR spectroscopy (Figure 5.16) in the temperature range from room temperature (RT) to 200 °C and under vacuum. This study was carried out in order to investigate the behavior of the Na-MOR once dehydrated after the amino acid loading from aqueous solution. Besides the two signals at 1970 and 1860 cm^{-1}, that correspond to the combination modes of Si-O stretching vibration (νSiO_2) of zeolite, common in all the spectra, the main feature in the RT sample is the sharp absorption at 1635 cm^{-1} assigned to the deformation mode (δH_2O) of the water molecules adsorbed at RT (black curve).

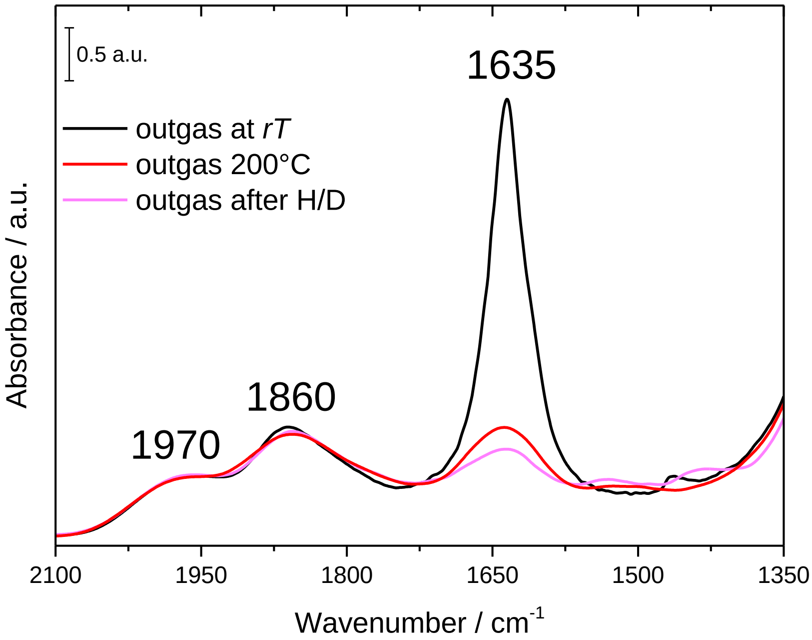

Figure 5.16: Infrared profiles in the 2100 – 1350 cm^{-1} range of Na-MOR sample after outgas at RT (black curve), outgas at 200 °C (red curve) and outgas after H/D isotopic exchange (pink curve).

The thermal treatment at 200 °C of the Na-MOR samples under outgas conditions (red curve) leaves a weak absorption of δH_2O witnessing that some H_2O molecules are still absorbed on the material. It is possible to estimate the amount of H_2O left after the outgas at 200 °C by integrating this signal. To do this, it is important to understand if the residual H_2O is responsible for the whole signal, hence a H/D isotopic exchange (shifting all the δH_2O signal at lower frequencies) is performed. The pink curve in figure 5.16 is the signal of the system after the H/D isotopic exchange showing the presence of an overtone mode of the zeolite at 1640 cm^{-1}. On the basis of this result it is possible to estimate the residual water in the Na-MOR degassed at 200 °C (subtracting from the signal collected that deriving from the overtone) in about 5% of the H_2O at RT. This result agrees with the TGA results where a further weight loss is found at temperature above 200 °C.

5.4.2 Na-MOR+gly sample

TGA + MSEGA and elemental analysis

Figures 5.17a shows the TG and the DTG curves of Na-MOR+gly sample and figure 5.17b the evolved gas masses spectrometry results during the thermal treatment. The different masses are identified on the basis of the ratio m/z (mass/charge number of ions).

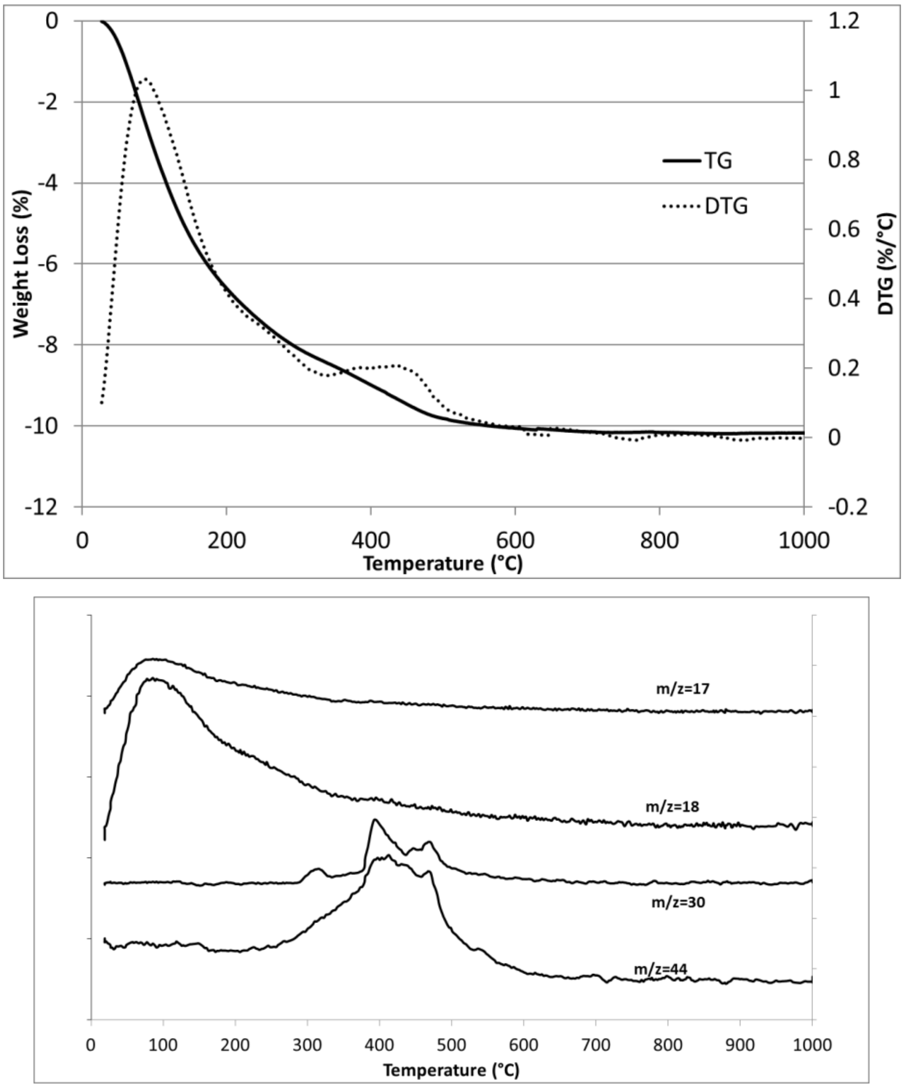

Figure 5.17: (top): TG and DTG curves of Na-MOR+gly sample; (bottom): Evolved gas mass resulting from the MSEGA analysis.

The following species were identified from the MSEGA output: m/z= 17 (OH^-, NH_3), m/z= 18 (H_2O), m/z= 30 (NO, CH_3-CH_3), m/z= 44 (CO_2). Since to perform TG analysis the powder was exposed to air, Na-MOR+gly sample re-adsorbed some H_2O molecules, as attested by the m/z = 18, 17 curves ascribed to H_2O and OH^- formed during dehydration. The loss of the re-adsorbed H_2O mostly occurs from RT to about 350 °C, as shown by the gas-mass 18 curve trend. The amino acid degradation begins at about 250 ° C and continues up to 550 °C, as shown by the loss of the 30 and 44 masses. The amount of glycine, can be estimated between 0.9 and 1.3 molecules p.u.c., even if, due to the presence of H_2O, whose release continues during glycine degradation, it is difficult to accurately define the precise amount of amino acid molecules in the cavities.

The degradation temperature of the amino acid loaded in the zeolite is higher than the degradation temperature of the pure amino acid, which is about 300 °C (Huang et al., 2013; Simmonds *et al.*, 1972). This result indicates the penetration of the amino acids inside the zeolite channels.

The elemental analysis performed on Na-MOR+gly sample indicates the following weight %: N= 0.58%; C= 1.03%; H= 1.29%, corresponding to a glycine content of about 1.4 molecules p.u.c., considering the N and C percentage. The H content should not be considered, being derived from for glycine, residual H_2O molecules and zeolite silanol defects.

IR spectroscopy

Figure 5.18 reports a selected region of the IR spectra of Na-MOR+gly sample, of the same sample in deuterated form (H/D) and of the activated (500 °C) Na-MOR sample. The IR spectra of the Na-MOR+gly sample shows the characteristic bands of the amide bond, in particular the amide I (ν C=O) at 1654 cm^{-1} and the amide II (ν C-N + δ CNH) as a weak shoulder under 1600 cm^{-1}. The peak at 1414 cm^{-1} can be associated to the νCOO^- of the carboxylate group of zwitterion glycine.

The isotopic exchange H/D leaves unchanged the C=O contribution of the glycine, shifting the δNH_3^+ and δH_2O at lower frequency (below 1200 cm^{-1}).

The H/D exchange is shown by the red curve in figure 5.18. In this spectrum the band at about 1630 cm^{-1} includes the C=O modes of different glycine forms (non-ionic glycine and zwitterion glycine). The contributions to the profile below 1500 cm^{-1} are shifted in the unique 1423 cm^{-1}

band. Such behavior has been reported (Martra *et al.*, 2014) to be compatible with the Amide II band (combination of νCN+δCNH), influenced by the isotopic exchange H/D.

The band at 1702 cm^{-1}, shifted after H/D exchange, can be associated or to a C=O stretching of an isolated glycine, in which the carboxyl group does not interact with cations or H_2O molecules, or to a cyclic glycine dimer (diketopiperazine, figure 5.19) as reported by Cheam *et al*. (1984). This species is formed by the reaction of two glycine molecules, and it cannot be excluded that the signals above attributed to the amide bond are related to this species.

Thus, it can be assumed that glycine molecules react in different ways when incapsulated in mordenite, some molecules react forming peptide or cyclic dimers, while other ones become zwitterions.

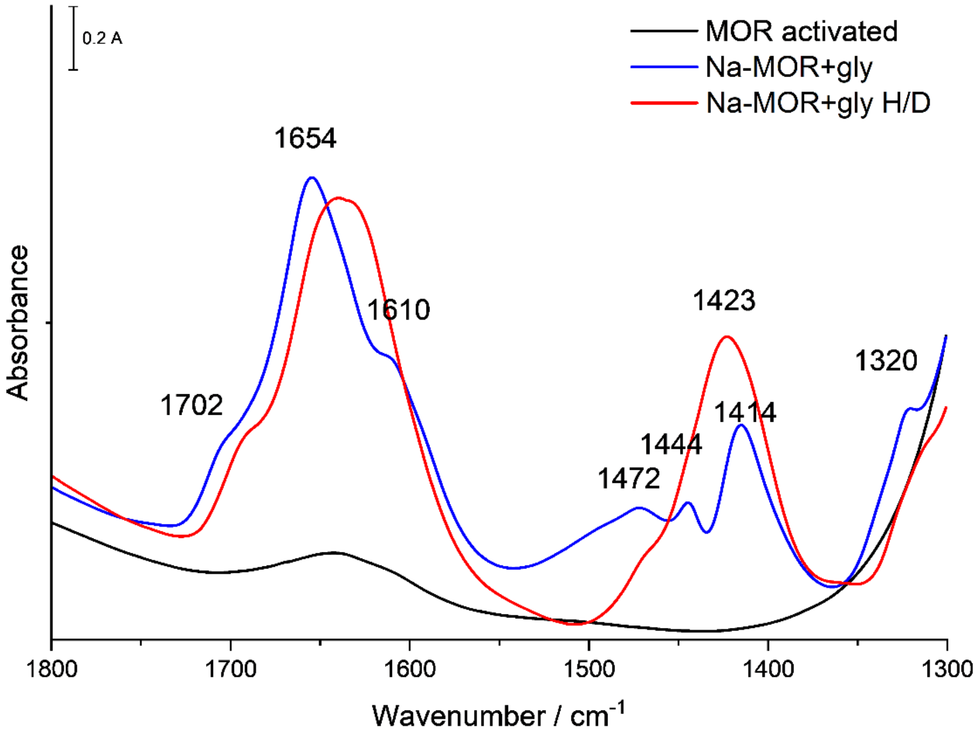

Figure 5.18: IR spectra of Na-MOR+gly sample (blue), Na-MOR+gly sample in deuterated form (H/D) (red) and activated at 500 °C Na-MOR sample (black).

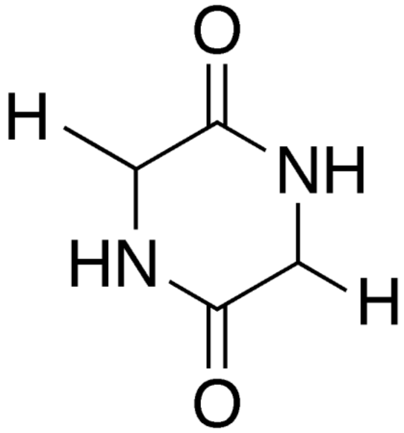

Figure 5.19: Diketopiperazine molecule formed by the reaction two glycine molecules.

Structural refinement

The structural refinement parameters of Na-MOR+gly at ambient conditions are reported in table 5.2. Atom coordinates and interatomic distances are reported in tables T3b and T4 in appendix. Figures 5.20 and 5.21 show the structure and the disposition of the glycine molecule inside the MOR channel. In order to simplify the system and facilitate the structural refinement, the framework oxygen O8 (divided over four sites in Na-MOR refinement) was set on a single position, averaging the previous O8 positions, with a higher $U_{iso,}$ respect to the other framework oxygen atoms.

The inspection of the difference Fourier map allowed localizing glycine molecules inside the 12MR channel. The glycine atoms occupy five crystallographycally independent partially occupied sites, all lying on the (100) plane. On the basis of the occupancy factor of these atoms (~0.32) and of the multiplicity of the positions (4) it is possible to calculate that 1.3 molecules p.u.c are hosted in Na-MOR, in agreement with both TG and elemental analysis.

Based on the Fourier map, Na3 cations are sited in the 8MR window of the side pocket, on the (100) mirror plane, differently from what observed in the pristine sample, while Na1 remains in the same position found in Na-MOR. Each glycine molecule coordinates one Na3 cation via the carboxyl group and the framework oxygen atom O10 via the amino group (figure 5.21, distances reported in table T4 in appendix).

The structural refinement shows a disposition of glycine molecules promising for the promotion of the condensation reaction. In fact, considering a full occupancy of each site and the steric hindrance of the atoms, two glycine molecules could be hosted in each channel of a unit cell (see figure 5.22), accounting for a total of 4 glycine molecules p.u.c. In this configuration, the distance between two equivalents glycine molecules in the channels is suitable for the peptide formation. However, as stated above, the amount of glycine inside the channels after vapor loading is about 1.3 molecules p.u.c., this means that the probability of finding two neighbor glycine molecules simultaneously present in the same channel is too low.

This indicates that further molecules could have been loaded in the zeolite cavities, but probably under these conditions of loading (see experimental section) this is the maximum filling achievable.

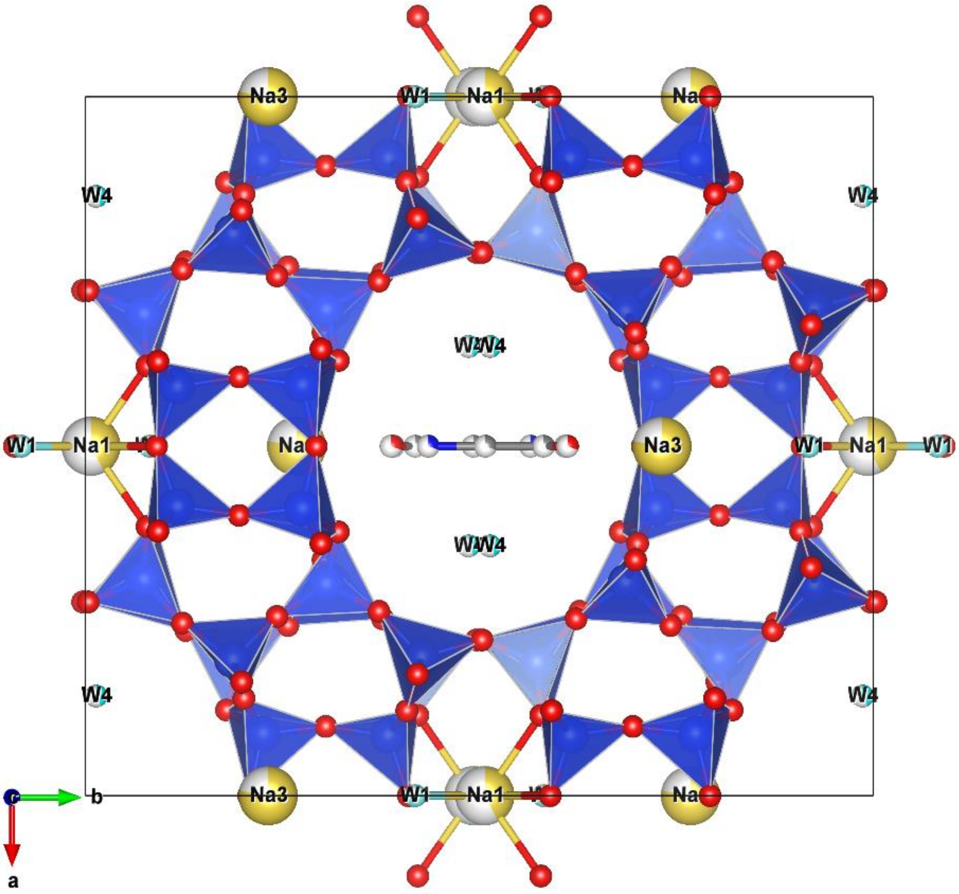

Figure 5.20: View along [001] of the Na-MOR+gly at $P_{amb.}$ Structural model is shown considering the full occupancy of the extraframework sites.

Although the sample was dehydrated before glycine loading and always manipulated in dry atmosphere, a small amount of H_2O molecules (6.7 molecules p.u.c. against the 26.6 in the original sample) was found in the sites W1 and W4 of the Na-MOR sample (figure 5.20).

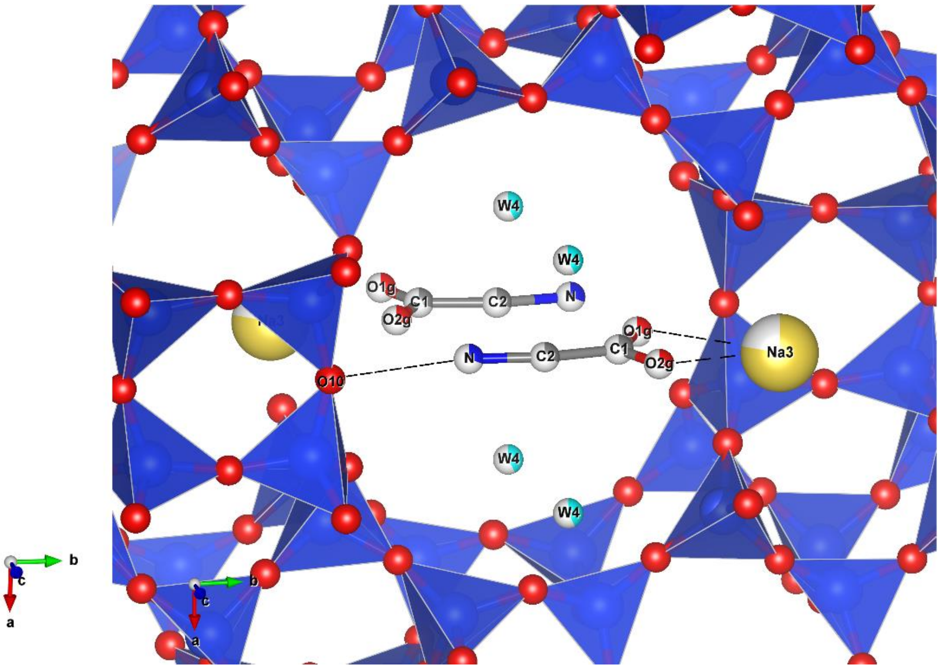

Figure 5.21: View of the 12MR channel containing the glycine molecules. Structural model is shown considering the full occupancy for the extraframework sites.

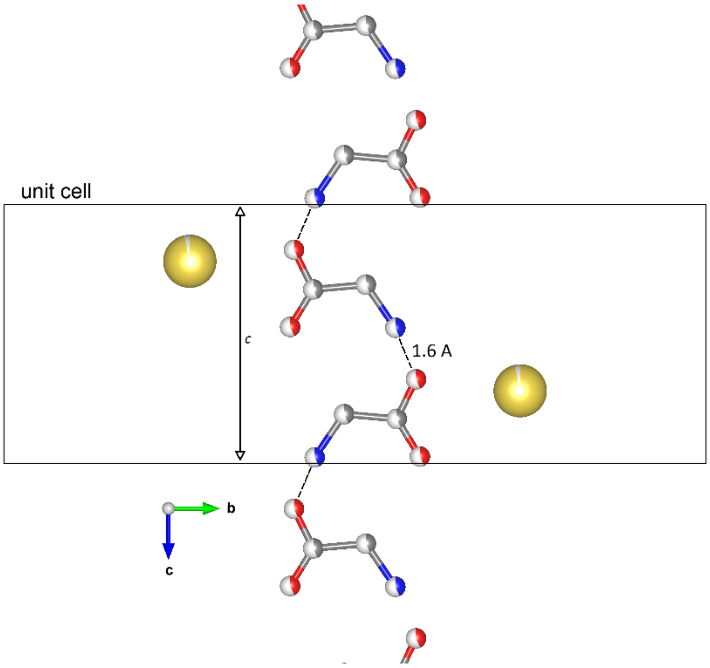

Figure 5.22: Disposition along the MOR channel of the glycine molecules assuming a full occupancy of the sites. MOR framework is not shown for sake of clarity. Yellow atoms are Na3 cations.

HP XRPD experiment: Na-MOR+gly compressed in Daphne oil

The structural refinement was possible only on the patterns collected on Na-MOR+gly in the non-penetrating PTM Daphne oil at P_{amb} (Na-MOR+gly_P_{amb}) and after pressure release (Pmax 2.7 GPa) (Na-MOR+gly_P_{amb}R). The refinement results are reported in tables T3c, T3d and T4 in appendix. The pressure treatment only induces slight variations on the glycine molecules and framework position. Specifically, the pressure induces the deformation of the 12MR channel along the *b* axis and reduces the coordination distances between the carboxyl group of the glycine and the sodium cation Na3 (glycine-Na3 distances in fig. 5.23), because of a slight shift of the molecules.

Due to the bad quality of the data, consequence of a slight pressure-induced loss of crystallinity of zeolite during the pressure treatment, it was impossible to follow the structural evolution of the system at high pressure. However, even if the quality of the Na-MOR+gly_P_{amb}R pattern (figure S2-d in appendix) is lower than Na-MOR+gly_P_{amb} (figure S2-c in appendix), it is possible to state that, whatever the structural modifications the system underwent at HP, they resulted quite reversible after the pressure release, in fact the amino acid molecules disposition is not far from the initial one.

Unit cell parameters and volume for all refinements are reported in table T5a in appendix. Fig. 5.24 shows the unit cell parameters trend up to 2.06 GPa; the quality of the data at the highest pressure (2.7 GPa) is too low for cell parameters determination. The unit cell volume at 2.06 GPa is reduced of about 12% respect to the original one and the *b* parameter is the more compressible axe, in accordance with previous HP studies on mordenite, where a strong anisotropic behaviour was observed (Gatta and Lee 2006).

Contrarily to what observed by Gatta and Lee (2006) a softening of the material is observed below 1.5 GPa for both experiments on Na-MOR+gly sample (fig. 5.24). As reported by Gatta and Lee (2014) and Quartieri *et al.* (2012), the compressional behaviour of zeolites under pressure is strongly influenced by the extraframework content.

The lack of structural refinements of the high-pressure experiments does not allow to properly understand the reason behind this trend, but the difference in the type and the amount of extraframework content (glycine molecules and H_2O molecules), respect to the sample reported by Gatta and Lee (2006) (only H_2O molecules), could influence the structural deformation of the framework under pressure.

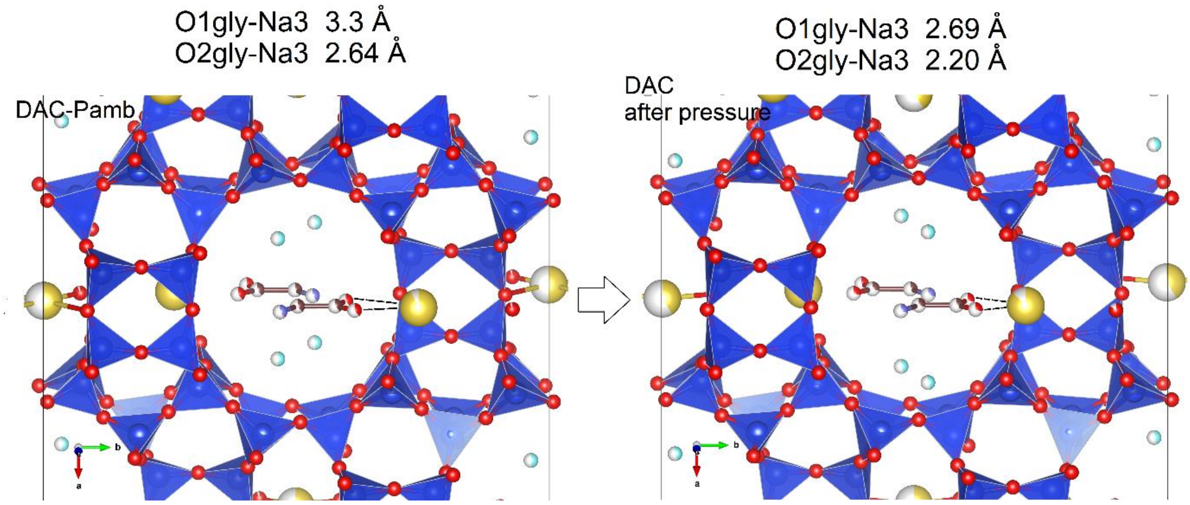

Figure 5.23: Glycine molecule inside 12MR channel at P_{amb} in DAC using Daphne oil (left) and in DAC after the pressure treatment (right).

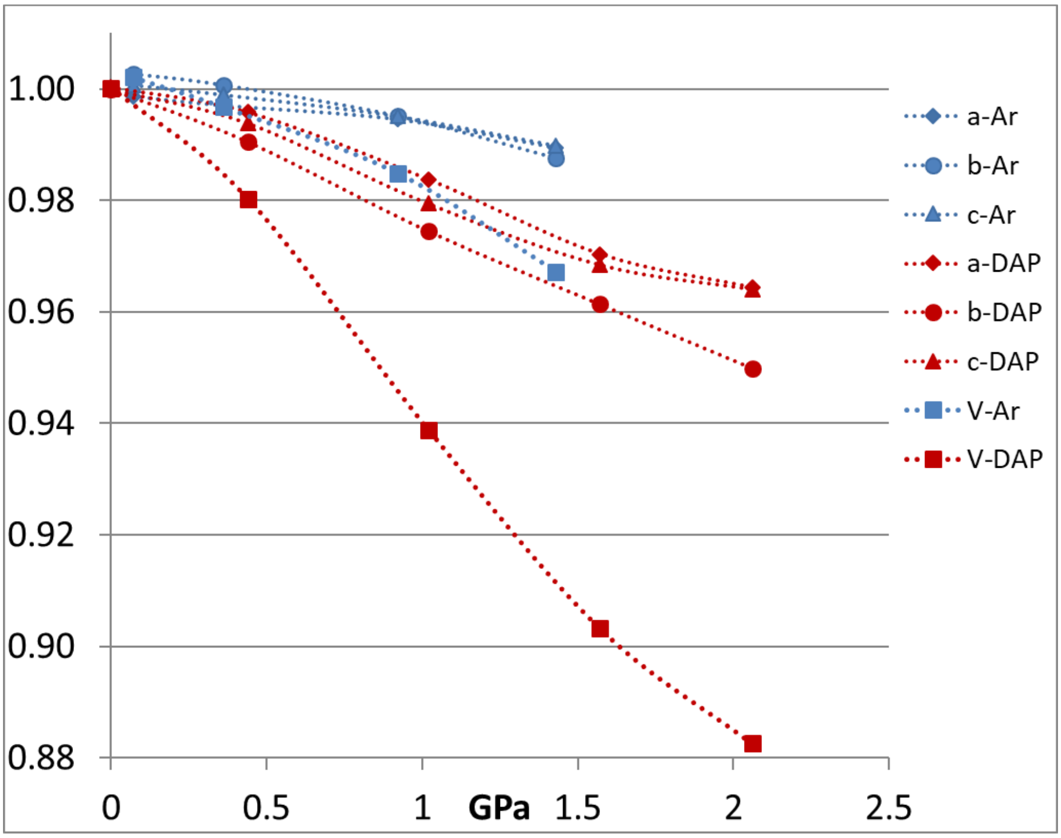

Fig. 5.24: Unit cell parameters (normalized to P_{amb} sample measured in capillary) vs. *P* of Na-MOR+gly sample. In red DAPHNE experiment (DAP) and in blue argon experiment (Ar).

The most interesting variation in the unit cell parameters to be considered, is the variation of the *c*-axis, since we can suppose that the glycine molecules should approach in the [001] direction to induce the oligomerization. The variation of the *c* parameter, at the highest-investigated pressure, is about 3.6% (table T5a in appendix) and if we exclude a rotation of the molecules, this shortening is too slight to promote a mechanical approach of the molecules at this degree of filling (figure 5.25).

In conclusion, the glycine loading in the Na-MOR+gly sample, performed by vapor phase, is insufficient to allow the formation of detectable peptide chains at HP.

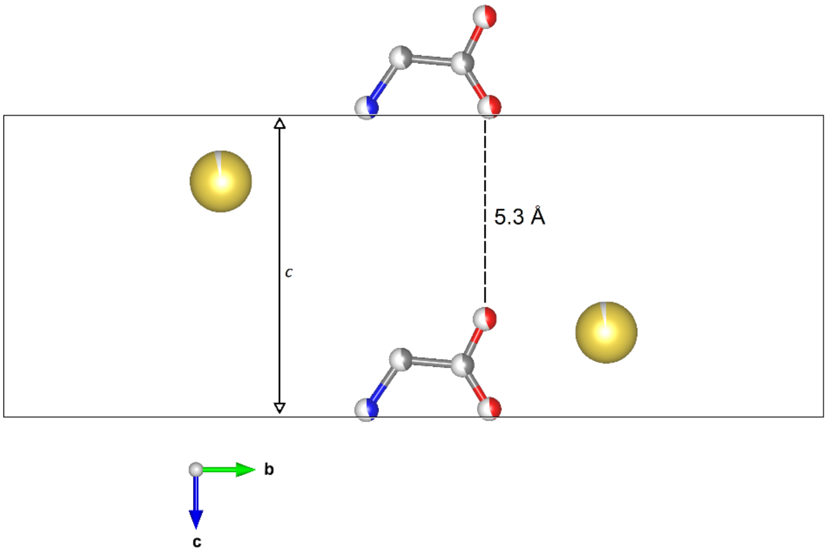

Figure 5.25: Real situation of the glycine molecule disposition along the MOR channel. MOR framework is not shown for sake of clarity. Yellow atoms are Na3 cations.

HP XRPD experiment: Na-MOR+gly compressed in argon

Concerning the HP experiment using Ar as penetrating PTM, a higher electronic density was found in the channels, even in the first pressure point investigated (0.07 GPa) suggesting the penetration of Ar inside the pores. Specifically, higher occupancy factors for the extraframework sites W4 and O1g (H_2O molecule and glycine oxygen respectively, both sited in the 12MR channel) were found, with respect to those of the original Na-MOR+gly. This indicates a mixed occupancy for these two sites. The amount of Ar increases with the pressure, hindering a straightforward interpretation of the difference Fourier maxima, due to the high scattering factor of the Ar atoms in comparison with that of the organic molecules. Because of the complexity of the system, the structural analysis on these X-ray diffraction data is really challenging and it not possible to evaluate if the penetration of Ar atoms in the zeolite porosity may induce an approach of the molecules or further hinders the diffusion of the glycine molecules.

Unit cell parameters and volume vs. *P* are reported in table T5b in appendix and shown in figure 5.24 of the previous paragraph. The unit cell volume at 1.43 GPa is reduced of about 3.3% respect to the original value.

HP RAMAN experiment: Na-MOR+gly_w compressed in fluorinert

Due to high fluorescence signal of the mordenite in the Na-MOR+gly sample, the HP Raman experiment was performed on Na-MOR+gly_w sample. The Raman spectra of Na-MOR+Gly_w loaded from aqueous phase (figure 5.26) show, with *P* increase, a slight weakening of the typical high intensity peak at 900 cm^{-1} of Glycine. The contributions assigned to the terminal groups are composed by two ill resolved bands at 1468 cm^{-1} and 1558 cm^{-1}. During the compression stage, and more evidently upon pressure release, these signals, become sharper and more intense (curve d, figure 5.26). Noticeably, the separation of the maxima of absorptions remains the same throughout the whole experiment. At high wavenumbers, between 2900 and 3000 cm^{-1}, the νCH signals seem to undergo the same process as the lower absorptions, although the low intensity of these bands does not allow a clear interpretation of the components behaviour. No peaks indicating the polymerization of the amino acid are visible in the Raman spectra.

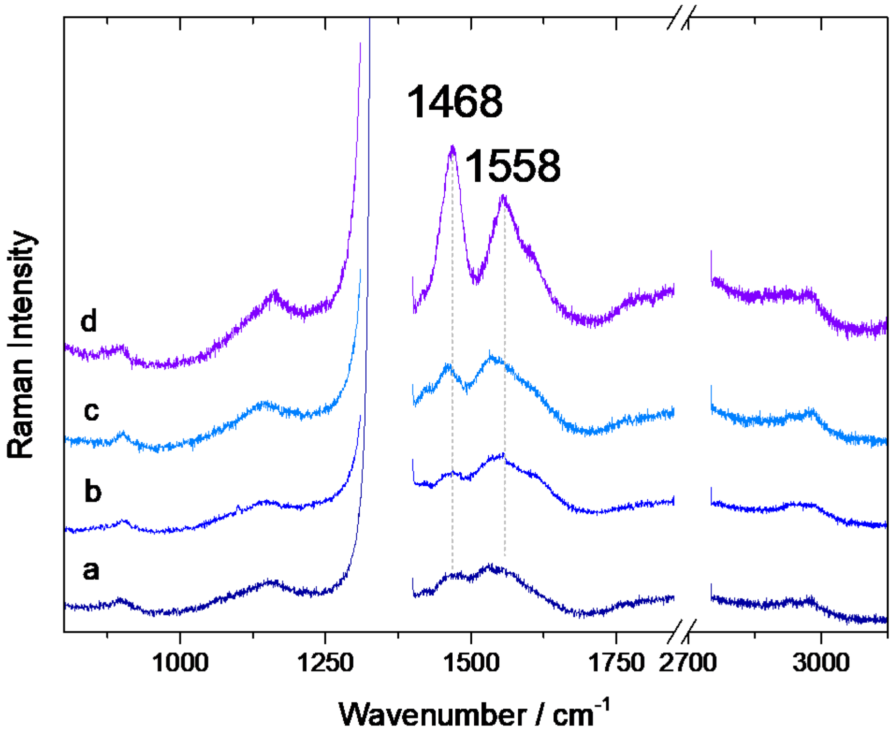

Figure 5.26: Raman spectra of Na-MOR+gly_w loaded from aqueous phase. a) 1.5 GPa, b) 3.4 GPa, c) 2.17 GPa during *P* release, d) 1.12 GPa during *P* release. The spectra are interrupted between 1300 and 1400 cm^{-1} due to the very intense signal of diamonds.

Large volume synthesis

To promote the diffusion of the glycine monomers through the zeolite pores in order to promote the formation of a detectable peptide in the MOR channel, a new sample was prepared in a “large volume cell”. Glycine and Na-MOR were put together at high pressure (0.44 GPa) and high temperature (150 °C) in order to promote the sublimation of glycine and its diffusion as vapor phase in the mordenite channels. The idea is that the pressure could facilitate penetration, diffusion and condensation of the molecules in form of vapour inside the zeolite channel system.

The sample recovered from HT/HP treatment was analysed with IR spectroscopy. The IR spectrum obtained (figure 5.27) is the sum of the signals of the pure glycine and of the zeolite. Despite the pressure value reached during the glycine loading, no amide signal is detected.

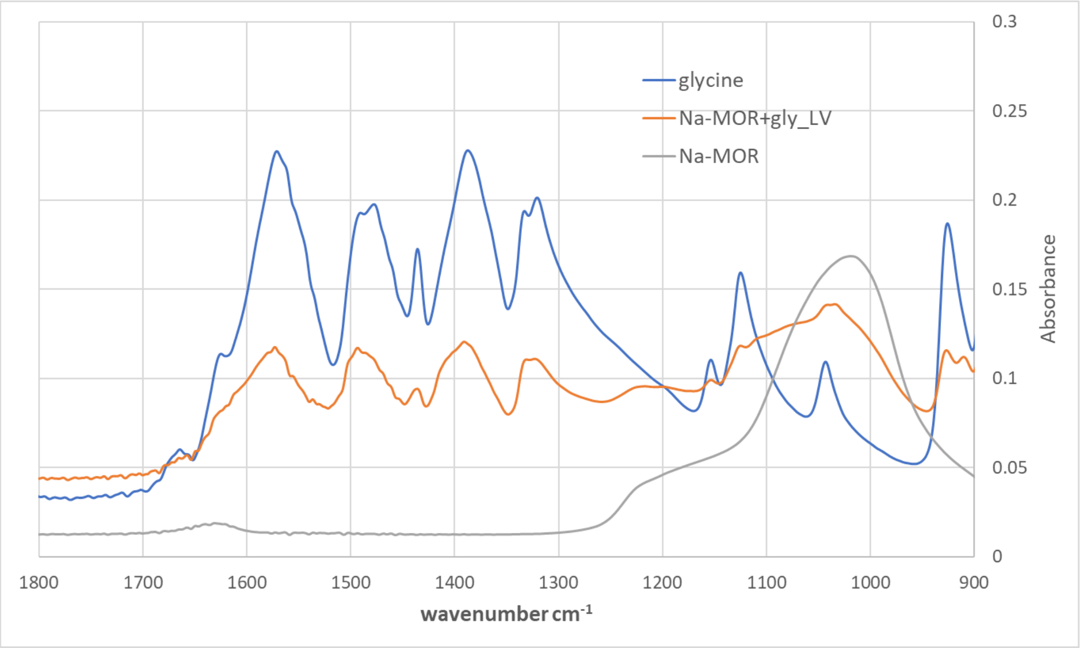

Figure 5.27: Selected region of IR spectrum of pure glycine, Na-MOR and large volume synthesized sample Na-MOR+gly_LV.

The reason of the missed formation of peptide could be related by the use of He PTM in the cell. He, as much as Ar in the in situ experiment, probably penetrates the zeolite pores hindering the diffusion of the glycine. Moreover, the presence of crystalline glycine, remained in the sample or re-crystallized after the sublimation, covers the signal of molecules entered into the zeolite cavities. Due to the presence of this crystalline amino acid, in the Na-MOR+gly_LV sample, a structural study with XRPD was not possible.

The results of the experiment have been probably compromised by the unfavourable experimental conditions. The factors that probably did not make effective the loading in the Large Volume experiments were, in addition to the molecules displacement operated by He, the too low ratio zeolite/amino acid.

5.4.3 Na-MOR+αala_w sample

TGA+ MSEGA and elemental analysis

TG and DTG curves of the Na-MOR+αala_w sample are shown in fig. 5.28a, the evolved gas masses spectrometry results are shown in figure 5.28b. The following species were identified from the MSEGA output: m/z= 17 (OH^-, NH_3), m/z= 18 (H_2O), m/z= 30 (NO, CH_3-CH_3), m/z= 44 (CO_2), m/z= 50 (C-C-CN).

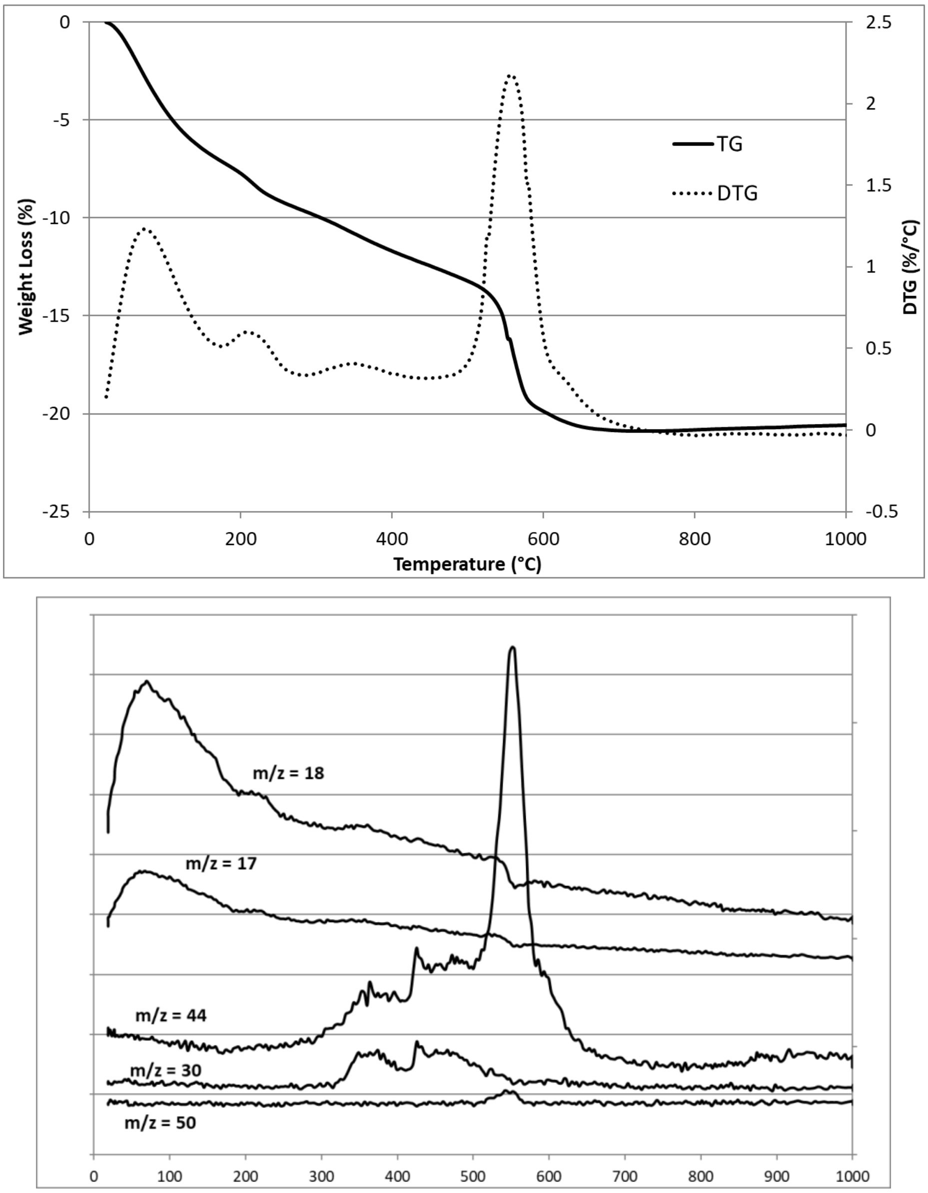

Figure 5.28: (top): TG and DTG curves of Na-MOR+αala_w sample; (bottom): evolved gas mass resulting from the MSEGA analysis.

The TG analysis shows a total weight loss of 20.9%. Five peaks are present in the DTG curve, the first two, at 80 °C and 200 °C, are ascribable to the water loss as visible from the curves of the masses 17 and 18 in figure 5.28b, the remaining loss, above 270 °C (11.6%), occurs in two main steps associated to two DTG peaks at 350 °C and 560 °C. The trend of the curves of the masses 30, 44 and 50 suggests that the remaining loss can be related to the alanine degradation. The amount of alanine calculated from the TG is 4.8 molecules p.u.c.

The elemental analysis performed on the sample, indicates the following weight %: N= 0.93%; C= 4.37%; H= 1.51%. Since H cannot be taken into account for the quantification of alanine in the channels, being it related to water molecules and to silanols of the framework, only C and N should be considered. On the basis of the C content the amount of alanine should be 4.5 molecules p.u.c. while on the basis of N 2.4 molecules p.u.c. To explain the very high difference between these two results, a hypothesis could be that the sample have been contaminated by vacuum grease with whom it came into contact during the dehydration of the sample in the vacuum tube. The presence of grease can alter the results of the TG analysis and the C content in the sample (being the grease constituted by hydrocarbon polymers). The huge peak in the gas mass curves of CO_2 (m/z= 44) at 600 °C, can be related to the grease decomposition, in fact, despite the constant He flux on the sample during the analysis, the oxidation of the degradation products can form carbon dioxide, whose oxygen derive from remaining atmospheric oxygen.

Considering the abovementioned issues, it is difficult to establish the loss related to the alanine molecules in the TG analysis and the only reliable result to estimate the amino acid content of the sample is the N% from elemental analysis. In conclusion, 2.4 molecules of alanine p.u.c. are hosted in Na-MOR.

IR spectroscopy

IR spectra of Na-MOR+αala_w sample outgassed at room temperature, outgassed at 150 °C and deuterated form are reported in figure 5.29. The spectra show the characteristic bands of the carboxylate group, the $\nu_{sym}COO^-$ and the $\nu_{asym}COO^-$ at 1414 cm^{-1} and 1630 cm^{-1}, respectively and also the peak of the $\delta_{sym}NH_3^+$ at 1515 cm^{-1}, all these peaks are related to alanine molecule in zwitterion form. No signal of amide bond is present.

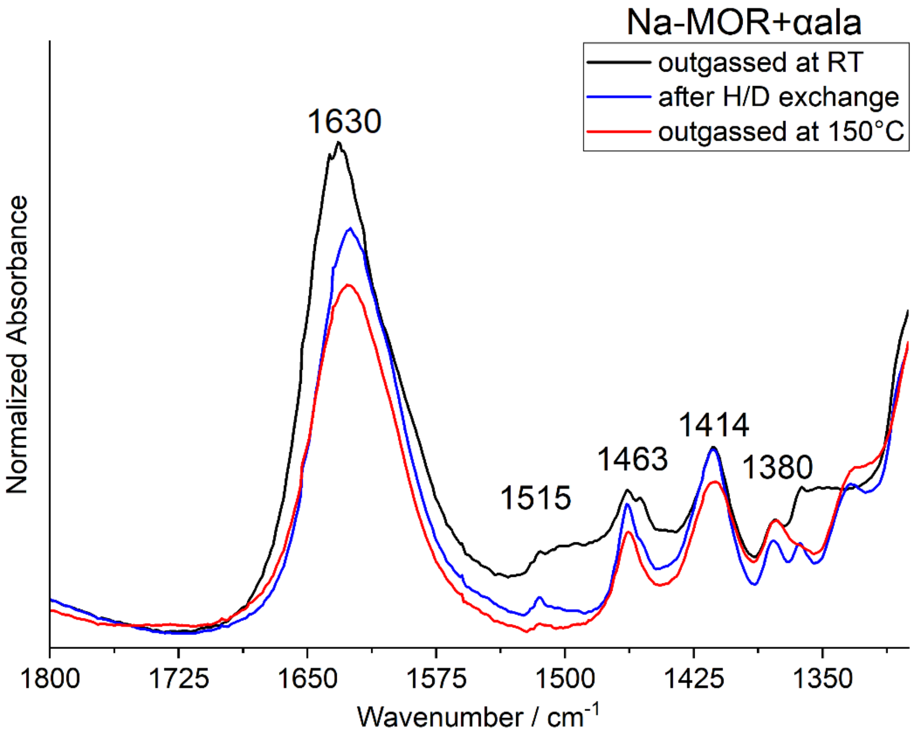

Figure 5.29: IR spectra of Na-MOR+αala_w sample outgassed at room temperature (black), outgassed at 150 °C (red), and deuterated ones (blue).

Structural refinement at P_{amb}

The Rietveld refinement of Na-MOR+αala_w sample was very challenging, due to the presence of maxima in the difference electron density map attributable to alanine molecules and/or to H_2O molecules strongly correlating each other. For the above-mentioned reasons, an accurate localization and quantification of the amino acid molecules was not possible. Overall, it is possible to asses, with a certain degree of confidence, that α-alanine molecules are located in the 12MR channel coordinating Na3 cations, similarly to the glycine molecule in the previous sample.

The presence of H_2O inside the MOR channels (probably consequence of involuntary re-adsorption or of a not complete dehydration after loading) together with alanine in zwitterion form indicate that loading from aqueous solution is non-effective to target polymerization. All the results available on this system suggest that no condensation can occur adsorbing the amino acid molecules from aqueous phase, being the molecules in the ionic form.

HP XRPD experiments: Na-MOR+αala_w compressed in Daphne oil and Ar

The variation of the unit cell parameters as a function of *P* are reported for both HP experiments in tables T5c and T5d in appendix and plotted in figure 5.30 after normalization to P_{amb} values measured in capillary. The data were refined with the Le Bail method for both experiments in the whole pressure range. When compressed in Daphne oil, Na-MOR+αala_w volume cell experiences a maximum variation at 3 GPa of 14.2%, while when compressed in Ar, the maximum variation at 2.1 GPa is 2.8%.

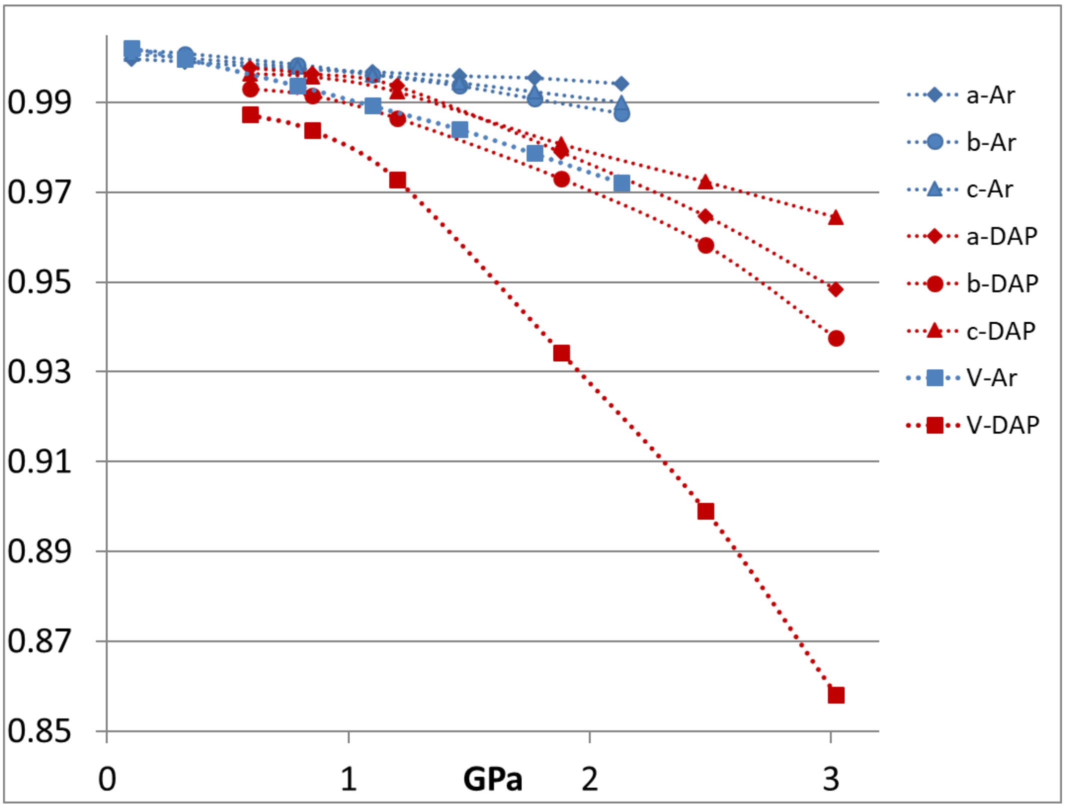

Figure 5.30: Unit cell parameters (normalized to P_{amb} sample measured in capillary) vs. *P* of MOR+αala_w sample. In red DAPHNE experiment (DAP) and in blue argon experiment (Ar).

Comparing the unit cell volume behaviour in the various HP experiments (figure 5.31), the Na-MOR+gly sample results in both experiments more compressible than the Na-MOR+αala_w sample in the respective PTM. This behaviour well agrees with a higher degree of pores filling in Na-MOR+αala_w sample.

Similar to what observed for the Na-MOR+gly sample, also the Na-MOR+αala_w presents a marked softening behaviour when compressed in both PTM above 1GPa. The interpretation of the structural mechanism responsible of this behaviour is hindered by the lack of a detailed structural analysis, but it can be supposed that the origin of this softening lies on the extraframework amount and type in the sample (alanine molecules and H_2O molecules).

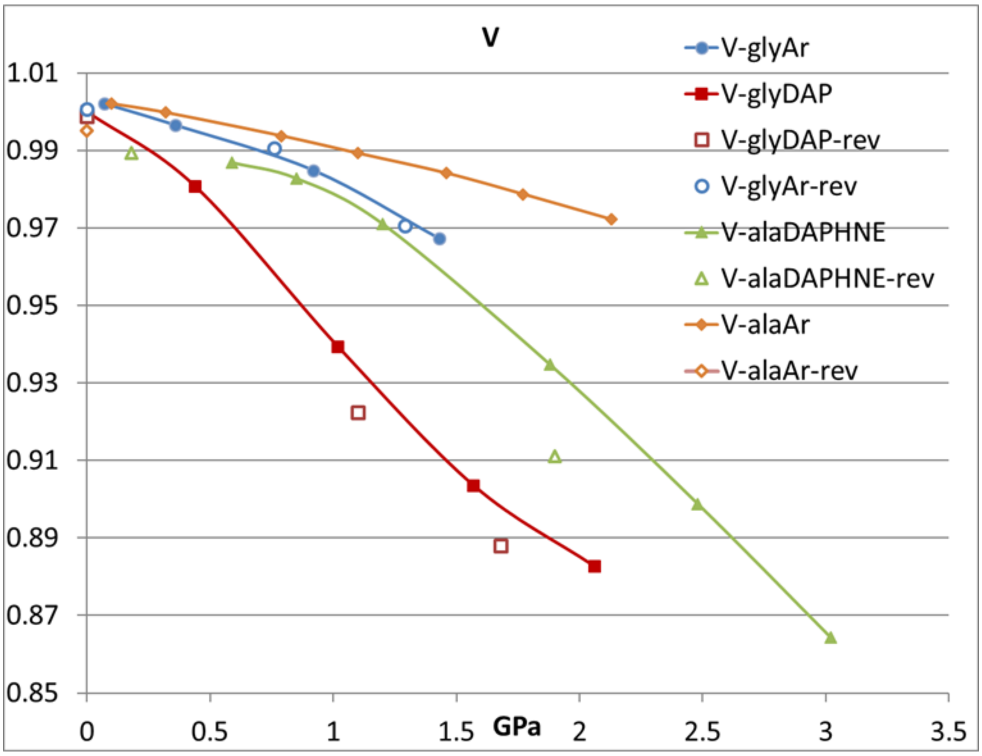

Figure 5.31: Unit cell volume behaviour of the Na-MOR+gly and the Na-MOR+αala_w samples during the various HP experiments. Empty markers represent the steps during pressure release.

5.4.4 Na-MOR+βala sample

TGA and elemental analysis

Figure 5.32 shows the TG and DTG analyses of MOR+βala sample.

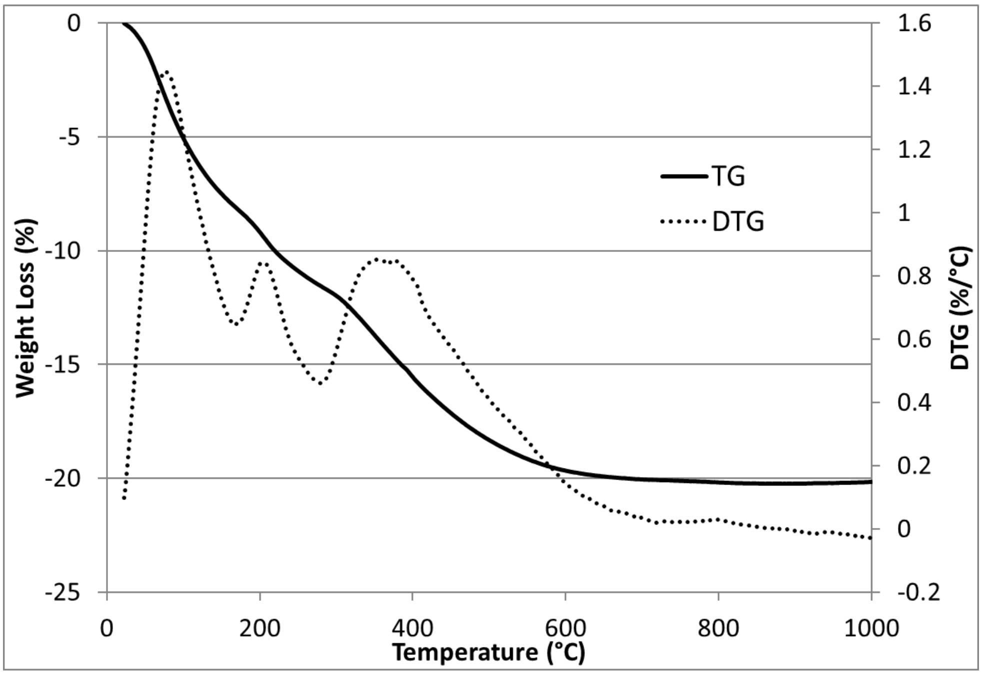

Figure 5.32: TG and DTG curves of Na-MOR+βala sample.

The total weight loss of the sample up to 800 °C is 20.1%. Considering the DTG curve, the loss ascribable to H_2O is about 11.2%, while that referable to the organic species is 8.9%. accounting for 3.7 β-alanine molecules hosted in each unit cell.

The elemental analysis performed on the sample indicates the following weight%: N= 1.42%; C= 4.75%; H= 2.08%. On the basis of the C content the amount of alanine should be 5.1 molecules p.u.c, while on the basis of N the amount of alanine is 3.8 molecules p.u.c.

Similar to what observed for the α-alanine loaded sample, the amount C wt. % would indicate a higher amino acid content with respect to that corresponding to N wt%. Since a contamination of the vacuum grease could be at the origin of this discrepancy, N% will be taken into account to estimate the β-alanine molecules inside the zeolite pores, that is 3.8 molecules p.u.c, in agreement with the result obtained by TG.

IR spectroscopy

The infrared spectra of the sample Na-MOR+βala are reported in figure 5.33. The spectrum of the loaded sample (black curve) shows the presence of a signal at 1641 cm^{-1} that is compatible with an Amide I type band (νC=O), accompanied by another signal at 1550 cm^{-1} assigned to the Amide II band (combination of νCN+δCNH). Another signal at 1604 cm^{-1} is related to the antisymmetric stretching of carboxylate moieties ($\nu_{asym}COO^-$), which is accompanied by the symmetric stretching ($\nu_{sym}COO^-$) at 1431 cm^{-1}, indicating that some of the molecules could be deprotonated.

Compared to the Gly vapor loading, the Na-MOR+βala sample (black curve fig. 5.33) clearly shows the presence of the additional component at 1550 cm^{-1} that is partially consumed by the H/D isotopic exchange (blue curve), accompanied by the rise in intensity of the band at 1431 cm^{-1} and of the higher frequency shoulder at 1468 cm^{-1}. This is the effect of the hydration of the amino acids, which are therefore converted into the zwitterionic form, causing the rise of the band at 1431 cm^{-1} of ($\nu_{sym}COO^-$), while the shoulder is compatible with the Amide II band that is being influenced by the isotopic exchange H/D (Martra *et al.*, 2014).

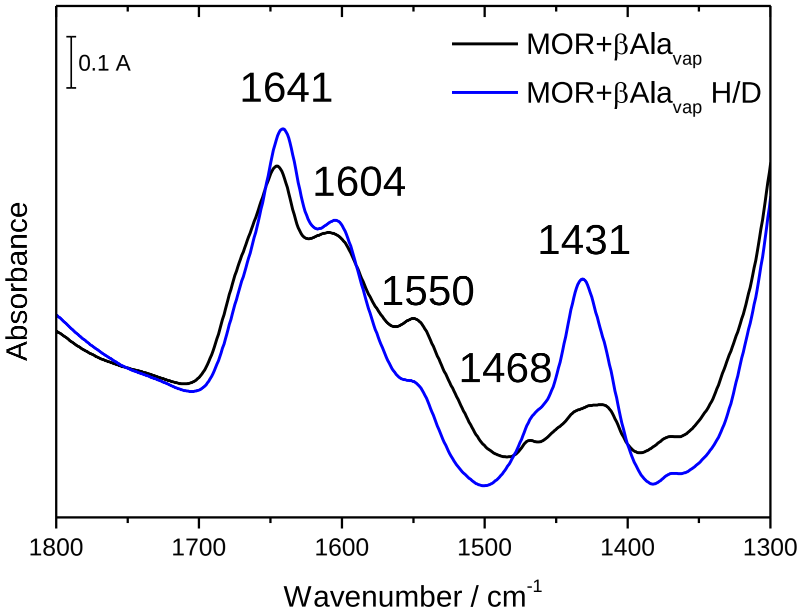

Figure 5.33: IR spectra of Na-MOR+βala sample outgassed at RT (black curve) and after H/D isotopic exchange (blue curve).

HP RAMAN experiment: Na-MOR+βala_w compressed in fluorinert

Due to high fluorescence signal of the mordenite in the Na-MOR+βala sample, the HP Raman experiment was performed only on Na-MOR+βala_w sample. The Raman spectra collected on Na-MOR+βala_w compressed in fluorinert (non-penetrating PTM) are shown in figure 5.34. The spectra clearly show the Raman signal of fluorinert in the region between 200 and 800 cm$^-$

^{1} and in the region between 1100 and 1400 cm^{-1} (Misopoulos *et al.*, 2017). Weaker is the signal of the mordenite, visible in the region between 400 and 500 cm^{-1} (Yu *et al.*, 2001). The spectra are interrupted between 1300 and 1400 cm^{-1} due to the very intense signal of diamonds. The amino acid molecules signals are visible in the region between 1400 and 1600 cm^{-1} and in the region at about 3000 cm^{-1}.

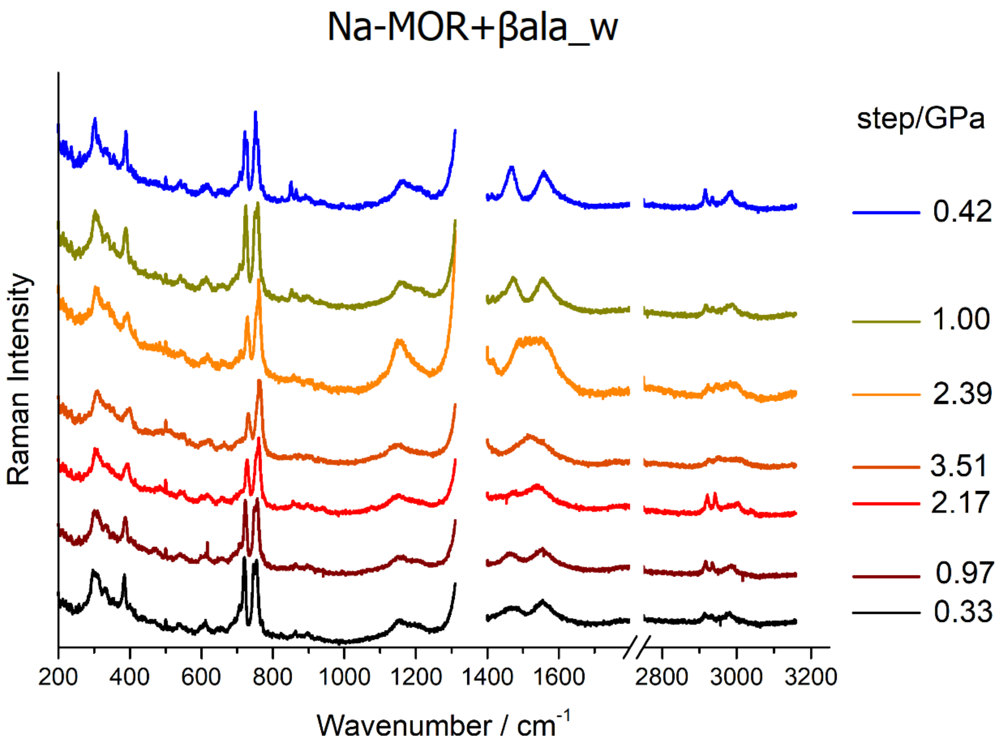

Figure 5.34: Raman spectra of the Na-MOR+ βala_w sample at different pressure values.

The increase in pressure (from black to dark orange curves) induces some modifications on the spectra. In fact, the two peaks at 1470 and 1550 cm^{-1} become one large peak in the spectra collected at the highest investigated pressure, probably indicating some changes in amino acid molecules inside the zeolite. The process is almost completely reversible, as visible in the spectra collected after pressure release (from red to blue curves). The 0.42 GPa spectrum is similar to the initial one (at 0.33 GPa), although the two mentioned peaks are sharper, probably indicating a more ordered arrangement of the molecules within the channels. In the C-H stretching zone between 2900 and 3000 cm^{-1} no visible changes occur with the pressure treatment. No peaks indicating the polymerization of the amino acid are visible in the Raman spectra, once again confirming that the loading in aqueous medium hinder the formation of amides.

Large volume synthesis

On the basis of the promising results obtained on the system mordenite + β-alanine loading via vapor phase, this system was also tested using large volume synthesis. The IR spectra collected on the Na-MOR+βala_LV sample (figure 5.35) show a strong signal of the β-alanine together with the signal of the mordenite sample. Even in this case, the high pressure does not seem to induce the formation of peptides. No amide signal is detected on the IR spectra of this sample, but it is worth noting that the signal of crystalline glycine -remained in the sample or re-crystallized after the sublimation- is very high, then can mask the signal of the molecules entered within the zeolite cavities.

The presence of crystalline amino acid on the surface of the Na-MOR+βala_LV sample, demonstrated even from the XRPD pattern collected on the recovered sample, hindered a detailed structural study.

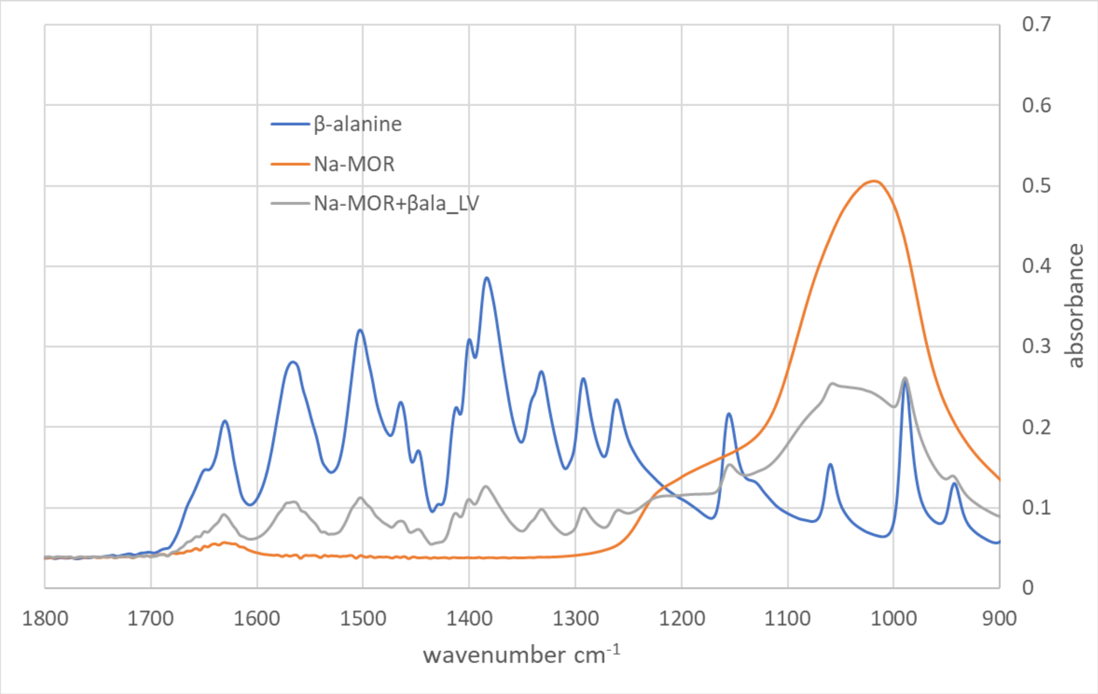

Figure 5.35: IR spectra in a selected region of pure β-alanine, Na-MOR sample, and Na-MOR+ βala_LV.

5.5 Concluding remarks

The experiments on amino acid polymerization in mordenite channels carried out in this thesis point to a new route in peptide synthesis, that can be exploited in a number of applications ranging from green chemistry synthesis to prebiotic chemistry research. The characterization of the obtained materials sheds light on crucial aspects and factors playing an important role in the formation of peptide molecules inside zeolite channels:

- The Na-MOR sample used in this thesis has the appropriate features required for peptide oligomerization experiments. In fact: i) the channel dimensions and shape are suitable to accommodate a peptide; ii) the Na^+ atoms position does not hinder the penetration of the amino acid molecules in the 12MR channel; iii) the penetration of the amino acid – and its interactions with the host material – seems to be strictly related to the presence of Na^+ cations in the side pockets. Hence, the Na^+ content (strictly linked to the Si/Al ratio) could influence the degree of filling of the zeolite. However, a limitation in the use of this Na-MOR can be related to its hydrophilicity: being its Si/Al ratio ~10, it has been very hard to maintain its dehydrated form during all the treatments. This is a crucial point since the unintentional penetration of water inside the zeolite hinders the formation of peptides under atmospheric conditions.
- The different amino acids enter in different amount into the zeolite channels, even using the same loading method. In particular, β-alanine vapor loading > α-alanine water loading > glycine in vapor loading. The loading from vapour phase is the only effective method able to leave the amino acid in the non-ionic form. The loading by adsorption from aqueous solution modifies the amino acid into its zwitterion form. This hinders the direct formation of the amide bonds, which can be formed only upon restabilising the non-ionic form.
- IR data have demonstrated the formation of the amide bonds at ambient conditions in the systems loaded by vapour phase. The IR spectra of Na-MOR+βala sample indicate the formation of a peptide. Otherwise, in the Na-MOR+gly sample, the presence of amide bonds can be related to the formation of a peptide or a cyclic dimer (diketopiperazine), by interaction between two glycine molecules.

- The main obstacle in obtaining a long peptide chain is linked to the degree of filling of the zeolite pores. Attempts to improve the filling were made by sublimating the amino acid molecules in a large volume cell under pressure. The results were not satisfactory, possibly in consequence of a wrong zeolite/amino acid ratio in the cells.

Overall, glycine and β-alanine vapour loaded mordenites seem to be the most promising systems, but further improvements in the experimental design and conditions must be done to obtain peptide chains within the zeolite channels. In the case of the Na-MOR+gly sample, the too low loading could be related to the insufficient diffusion of the glycine molecules into the zeolite channels during the vapor loading and to the formation of a barrier on the channel edges that can hinder the penetration of the molecules in the inner part. This hypothesis could explain why the IR technique records the presence of the peptide bond, while the average view provided by XRPD, requiring the presence of a long-range order, does not allow identifying unambiguously any peptide.

An alternative strategy could consist in loading the zeolite in DAC by injection of the amino acid dissolved in a PTM. The selected solvent should have the following characteristics: 1) be polar and able to dissolve the amino acid molecules keeping them in non-ionic form; 2) be water free; 3) be formed by molecules large enough not to penetrate the zeolite pores; 4) have IR (or Raman) signals not overlapped to the signals of the amino acid and of the peptide.

To obtain a possible condensation process inside a zeolite, and to study it by means of an in situ approach, all these conditions should be fulfilled at the same time. A combination of spectroscopic methods, necessary to monitor the formation of the peptide, and diffraction, unravelling the final structure of the hybrids, will be mandatory.

6 CONCLUSIONS

This PhD thesis is focused on the host-guest interactions in different systems constituted by zeolites hosting molecules within their cavities. Although the two topics described in this thesis are aimed to different purposes, for both the key factor is how the guest molecules react when restricted in the confined environment provided by zeolite pores and subjected to non-ambient conditions.

In the first project (CO_2 entrapment in FAU zeolites), it has been observed how the extraframework content (Na cations, H_2O molecules) of the Na-X and Na-Y zeolites can influence the physisorption and chemisorption of the CO_2 molecules, one of the main factors regulating the possible storage of the carbon dioxide in porous materials. In the second work (amino acids condensation in mordenite), the importance of the geometrical constraint imposed by the MOR framework on amino acid molecules and the influence of the Na cations and H_2O on the molecules arrangement and on the condensation reaction has been determined.

From both studies it is clear that the zeolite cavities can be exploited for inducing reactions as a small chemical laboratory, and the results may change depending on the crystal-chemical features of the host material and on environmental conditions.

The re-organization of the guest molecules in zeolitic hosts, promoted by pressure is one of the most fascinating discoveries in material science, with potential technological and geological implications. This thesis contributed to shed light on new knowledge of this growing branch of science.

Appendix: Tables

Tables T1. Atomic fractional coordinates, occupancy factors and thermal isotropic parameters ($Å^2$) for Na-X (T1a) and Na-Y (T1b) structures under the different experimental conditions.

T1a

Na-X RT						
atoms	**x**	**y**	**z**	**frac**	**Uiso**	**mult**
T1	-0.0488(2)	0.1282(3)	0.0309(3)	1	0.0038(7)	96
T2	-0.0598(2)	0.0409(2)	0.1222(3)	1	0.0038(7)	96
O1	-0.1089(4)	-0.0010(4)	0.1059(5)	1	0.0085(12)	96
O2	-0.0086(3)	0.0052(4)	0.1384(3)	1	0.0085(12)	96
O3	-0.0365(3)	0.0761(3)	0.0703(3)	1	0.0085(12)	96
O4	-0.0739(3)	0.0761(1)	0.1801(4)	1	0.0085(12)	96
Na2	0.0332(4)	0.0332(4)	0.0332(4)	0.593(8)	0.04	32
Na2'	0.0743(6)	0.0743(6)	0.0743(6)	0.407(8)	0.04	32
Na3	0.2348(2)	0.2348(2)	0.2348(2)	0.946(14)	0.036(4)	32
Na6	0.4513(9)	0.2709(9)	0.1937(8)	0.360(3)	0.041(7)	96
W2	0.1771(5)	0.0729(5)	-0.3229(5)	1	0.043(3)	32
W3	0.2678(5)	0.0379(5)	-0.3896(5)	0.873(5)	0.043(3)	96
W4	0.4095(10)	0.3151(12)	0.1845(9)	0.59(1)	0.043(3)	96
W5	0.151(5)	0.0136(28)	-0.406(5)	0.127(5)	0.043(3)	96
W6	-0.0890(1)	-0.0890(1)	-0.1611(1)	0.769(9)	0.043(3)	32
W8	0.0878(17)	-0.0514(14)	-0.3907(20)	0.410(1)	0.043(3)	96
Na-X D-RT						
T1	-0.0519(2)	0.1289(2)	0.0346(2)	1	0.08	96
T2	-0.0534(2)	0.0373(2)	0.1191(2)	1	0.08	96
O1	-0.1086(4)	-0.0009(5)	0.1055(5)	1	0.016(14)	96
O2	-0.0078(3)	-0.0073(3)	0.1384(3)	1	0.016(14)	96
O3	-0.0338(3)	0.0759(3)	0.0692(3)	1	0.016(14)	96
O4	-0.0668(3)	0.0732(3)	0.1747(3)	1	0.016(14)	96
Na2	0.0369(4)	0.0369(4)	0.0369(4)	0.652(11)	0.04	32
Na2'	0.0624(7)	0.0624(7)	0.0624(7)	0.348(11)	0.04	32
Na3	0.2360(2)	0.2360(2)	0.2360(2)	1	0.033(16)	32
Na6	0.4462(8)	0.2588(11)	0.1624(7)	0.307(4)	0.04	96
W3	0.2725(8)	-0.0901(5)	-0.2878(6)	0.699(8)	0.08	96
W6	-0.0819(4)	-0.0819(4)	-0.1682(6)	0.833(10)	0.08	32
W8	0.1105(23)	-0.0345(9)	-0.3794(24)	0.335(8)	0.08	96

Na-X CO_2						
T1	-0.0576(2)	0.1263(3)	0.0389(2)	1	0.012(1)	96
T2	-0.0497(2)	0.0358(3)	0.1214(3)	1	0.012(1)	96
O1	-0.1025(4)	-0.0030(4)	0.1097(5)	1	0.022	96
O2	-0.0021(3)	-0.0053(3)	0.1390(3)	1	0.022	96
O3	-0.0291(2)	0.0755(3)	0.0725(3	1	0.022	96
O4	-0.0716(2)	0.0689(3)	0.1758(3)	1	0.022	96
Na2	0.0355(3)	0.0355(3)	0.0355(3)	0.534(8)	0.040(6)	32
Na2'	0.0628(3)	0.0628(3)	0.0628(3)	0.466(8)	0.021(6)	32
Na3	0.2377(2)	0.2377(2)	0.2377(2)	0.969(10)	0.034(3)	32
Na6	0.4810(3)	0.2931(5)	0.1592(5)	0.320(3)	0.06	96
W6	-0.08893(4)	-0.08893(4)	-0.16117(4)	0.804(7)	0.088(11)	32
W7	0.2157(2)	0.0343(2)	-0.2843(2)	0.517(10)	0.084(12)	32
W9	0.0277(2)	0.1191(5)	-0.3222(3)	0.491(4)	0.11(1)	96
W10	0.0439(8)	-0.0212(6)	-0.3598(8)	0.509(4)	0.071(9)	96
C1	0.3143(13)	-0.0962(11)	-0.3253(13)	0.274(2)	0.06	96
O11	0.2879(8)	-0.0517(3)	-0.3309(6)	0.335(2)	0.10(1)	96
O12	0.1682(3)	-0.0347(5)	-0.3396(7)	0.284(2)	0.06	96
O13	0.1037(13)	-0.0799(9)	-0.3328(10)	0.343(2)	0.068(12)	96
Na-X AP						
T1	-0.0497(3)	0.1270(4)	0.0350(4)	1	0.011(1)	96
T2	-0.0586(3)	0.0393(3)	0.1218(4)	1	0.011(1)	96
O1	-0.1068(6)	-0.0042(7)	0.1067(9)	1	0.014(2)	96
O2	-0.0061(4)	0.0053(4)	0.1341(4)	1	0.014(2)	96
O3	-0.0294(4)	0.0772(5)	0.0753(5)	1	0.014(2)	96
O4	-0.0749(4)	0.0750(5)	0.1768(5)	1	0.014(2)	96
Na2	0.0348(6)	0.0348(6)	0.0348(6)	0.55(1)	0.02(1)	32
Na2'	0.0622(5)	0.0622(5)	0.0622(5)	0.45(1)	0.02(1)	32
Na3	0.2382(4)	0.2382(4)	0.2382(4)	0.94(2)	0.034(5)	32
Na6	0.4806(8)	0.2864(6)	0.1622(7)	0.311(5)	0.09(1)	96
W6	-0.0897(7)	-0.0897(7)	-0.1604(6)	0.85(1)	0.08	32
W7	0.1928(6)	0.0572(5)	-0.3072(6)	0.35(2)	0.08	32
W9	0.0327(7)	0.1053(8)	-0.3220(8)	0.171(7)	0.07(4)	96
W10	0.0490(9)	-0.0429(9)	-0.3501(8)	0.53(1)	0.06(1)	96
C1	0.3212(16)	-0.0871(17)	-0.3262(16)	0.262(3)	0.06	96
O11	0.2805(17)	-0.0584(20)	-0.3227(18)	0.331(3)	0.06	96
O12	0.1704(6)	-0.0255(15)	-0.3265(24)	0.234(3)	0.06	96
O13	0.1170(20)	-0.0775(17)	-0.3432(15)	0.255(3)	0.06	96

T1b

Na-Y RT						
atoms	**x**	**y**	**z**	**frac**	**Uiso**	**mult**
T1	-0.05449(9)	0.1261(1)	0.0367(1)	1	0.0041(6)	192
O1	-0.1113(2)	0	0.1113(2)	1	0.0065(9)	96
O2	-0.0038(2)	-0.0038(2)	0.1438(2)	1	0.0065(9)	96
O3	-0.0324(3)	0.0752(2)	0.0752(2)	1	0.0065(9)	96
O4	-0.0770(3)	0.0718(2)	0.1781(2)	1	0.0065(9)	96
Na2'	0.0819(4)	0.0819(4)	0.0819(4)	0.455(6)	0.0380(3)	32
Na2	0.0413(4)	0.0413(4)	0.0413(4)	0.417(8)	0.0380(3)	32
Na3	0.2434(2)	0.2434(2)	0.2434(2)	0.82(1)	0.0380(3)	32
W1	-0.1491	-0.1491	-0.2255	0.196(4)	0.072(4)	96
W2	0.1960(6)	-0.0363(4)	-0.2137(4)	0.545(5)	0.072(4)	96
W3	0.1445(3)	-0.0081(4)	0.4505(4)	0.524(4)	0.072(4)	192
W4	0.3323(5)	-0.0823(5)	-0.2982(7)	0.5	0.072(4)	96
W5	0.1652(5)	0.0848(5)	-0.3348(5)	0.618(7)	0.072(4)	32
Na-Y D-RT						
T1	-0.551(1)	0.1252(1)	0.0358(2)	1	0.092(7)	192
O1	-0.1082(2)	0	0.1082(2)	1	0.015	96
O2	-0.0004(3)	-0.0004(3)	0.1382(3)	1	0.015	96
O3	-0.0351(3)	0.0739(2)	0.0739(2)	1	0.015	96
O4	-0.0736(3)	0.0736(3)	0.1765(3)	1	0.015	96
Na2'	0.0745(1)	0.0745(1)	0.0745(1)	0.198(8)	0.012(16)	32
Na2	0.0420(4)	0.0420(4)	0.0420(4)	0.70(1)	0.096(10)	32
Na3	0.2333(2)	0.2333(2)	0.2333(2)	1.00(1)	0.019(4)	32
W2	0.1837(14)	-0.0637(17)	-0.2745(18)	0.165(3)	0.04(2)	192
W6	-0.0797(28)	-0.0797(28)	-0.1704(28)	0.100(7)	0.07	32

Na-Y CO_2						
T1	-0.0540(1)	0.1246(1)	0.0361(1)	1	0.0098(7)	192
O1	-0.1083(2)	0	0.1083(2)	1	0.015(1)	96
O2	-0.0019(2)	-0.0019(2)	0.1406(2)	1	0.015(1)	96
O3	-0.0330(3)	0.0756(2)	0.0756(2)	1	0.015(1)	96
O4	-0.0717(3)	0.0740(3)	0.1759(3)	1	0.015(1)	96
Na2'	0.0650(6)	0.0650(6)	0.0650(6)	0.352(9)	0.016(9)	32
Na2	0.0414(4)	0.0414(4)	0.0414(4)	0.51(1)	0.078(11)	32
Na3	0.2373(1)	0.2373(1)	0.2373(1)	1.00(1)	0.034(4)	32
W3	0.1445(6)	-0.0101(6)	-0.4643(6)	0.248(8)	0.056(14)	192
W6	-0.0822(11)	-0.0822(11)	-0.1679(11)	0.236(8)	0.09(4)	32
C2	0.0769(13)	0.0339(16)	-0.3269(13)	0.141(2)	0.07(2)	96
O21	0.0551(2)	-0.0024(8)	-0.3051(2)	0.191(2)	0.07(2)	96
O22	0.0643(17)	0.1028(12)	-0.3528(12)	0.141(2)	0.07(2)	96
C3	0.2927(6)	0.0594(11)	-0.2073(6)	0.363(2)	0.08	96
O31	0.2640(7)	-0.0140(7)	-0.3336(12)	0.363(2)	0.10(1)	96
O32	0.1759(5)	-0.0415(8)	-0.3241(5)	0.363(2)	0.08	96
C4/O41	0.1082(1)	-0.0565(9)	-0.3582(1)	0.37(1)	0.09(1)	96
O42	0.1754(2)	-0.0516(2)	-0.4254(2)	0.18(1)	0.08	96
Na-Y AP						
T1	-0.0541(1)	0.1250(1)	0.0363(1)	1	0.011(1)	192
O1	-0.1082(2)	0	0.1082(2)	1	0.013(1)	96
O2	-0.0021(2)	-0.0021(2)	0.1421(3)	1	0.013(1)	96
O3	-0.0324(3)	0.0749(2)	0.0749(2)	1	0.013(1)	96
O4	-0.0714(3)	0.0734(3)	0.1765(3)	1	0.013(1)	96
Na2'	0.0657(5)	0.0657(5)	0.0657(5)	0.359(7)	0.002(8)	32
Na2	0.0395(4)	0.0395(4)	0.0395(4)	0.47(1)	0.074(11)	32
Na3	0.2346(2)	0.2346(2)	0.2346(2)	1.00(1)	0.031(3)	32
W3	0.1456(16)	-0.0113(13)	-0.4601(16)	0.113(5)	0.02(2)	192
W6	-0.0772(16)	-0.0772(16)	-0.1729(16)	0.161(8)	0.054(44)	32
C2	0.081(6)	0.030(10)	-0.331(6)	0.039(2)	0.08	96
O21	0.0513(17)	0.007(10)	-0.3013(17)	0.039(2)	0.082(80)	96
O22	0.061(5)	0.106(4)	-0.356(4)	0.039(2)	0.08	96
C3	0.2932(6)	0.0553(12)	-0.2068(6)	0.214(2)	0.08	96
O31	0.2650(8)	-0.0150(9)	-0.3316(17)	0.214(2)	0.08	96
O32	0.1744(5)	-0.0422(13)	-0.3256(5)	0.214(2)	0.11(3)	96
C4/O41	0.1082(1)	-0.0644(2)	-0.3582(1)	0.142(6)	0.11(3)	96
O42	0.1754(3)	-0.062(5)	-0.4254(3)	0.068(3)	0.08	96

Table T2. Selected framework and extraframework distances (Å) for Na-X (T2a) and Na-Y (T2b) structures under different experimental conditions (only distances shorter than 3.2 Å are reported).
T2a

RT				D-RT				CO₂				AP			
T1	**O1**	1.680(9)		**T1**	**O1**	1.662(4)		**T1**	**O1**	1.687(8)		**T1**	**O1**	1.69(2)	
	O2	1.694(9)			**O2**	1.556(4)			**O2**	1.690(8)			**O2**	1.72(1)	
	O3	1.664(5)			**O3**	1.644(4)			**O3**	1.679(5)			**O3**	1.68(8)	
	O4	1.696(5)			**O4**	1.614(4)			**O4**	1.664(5)			**O4**	1.66(8)	
T2	**O1**	1.668(5)		**T2**	**O1**	1.713(4)		**T2**	**O1**	1.662(5)		**T2**	**O1**	1.662(8)	
	O2	1.614(5)			**O2**	1.664(4)			**O2**	1.630(6)			**O2**	1.592(9)	
	O3	1.673(5)			**O3**	1.651(4)			**O3**	1.654(5)			**O3**	1.664(8)	
	O4	1.686(5)			**O4**	1.686(4)			**O4**	1.683(5)			**O4**	1.685(8)	
Na2	**O2**	2.954(3)	X3	**Na2**	**O2**	2.983(7)	x3	**Na2**	**O2**	2.931(7)	x3	**Na2**	**O2**	2.822(3)	x3
	O3	2.237(1)	X3		**O3**	2.172(7)	x3		**O3**	2.110(6)	x3		**O3**	2.141(3)	x3
Na2'	**O3**	2.77(1)	X3	**Na2'**	**O3**	2.432(7)		**Na2'**	**O2**	3.021(7)	x3	**Na2'**	**O2**	2.897(6)	x3
	W6	2.23(2)	X3		**W6**	2.73(2)	X3		**O3**	2.329(6)	X3		**O3**	2.33(1)	X3
									W6	2.623(12)	x3		**W6**	2.64(2)	x3
Na3	**O2**	2.466(3)	X3	**Na3**	**O2**	2.553(7)	x3	**Na3**	**O2**	2.530(7)	x3	**Na3**	**O2**	2.611(5)	x3
	O4	2.971(1)	X4		**O4**	2.931(9)	x3		**O4**	2.962(7)	x3		**O4**	3.058(2)	x3
					W6	2.94(1)									
Na6	**W3**	2.66(2)		**Na6**	**O1**	2.616(8)		**Na6**	**O1**	2.863(9)		**Na6**	**O1**	3.07(3)	
	W4	2.83(2)			**O4**	2.950(8)			**O4**	2.633(4)			**O4**	2.74(2)	
	W8	2.26(2)			**W3**	2.51(2)			**W7**	2.738(12)			**W7**	3.11(2)	
									W9	3.053(10)			**W9**	3.19(1)	
									W10	2.073(8)			**W10**	2.31(4)	
									C1	3.030(12)			**C11**	3.04(3)	
									C1	3.060(7)			**C11**	2.87(1)	
									O11	2.726(12)			**O11**	2.26(3)	
									O11	2.399(8)			**O11**	2.575(9)	
									O12	2.448(9)			**O12**	2.370(8)	
									O12	2.526(7)			**O12**	2.50(2)	
									O13	3.041(11)			**O12**	2.83(1)	
													O13	3.05(2)	
W2	**W3**	2.95(1)	X3												
	W5	2.63(11)	X3												

	W5	2.52(12)	X3												
W3	**O4**	3.16(1)		**W3**	**O1**	2.981(9)									
	Na6	2.66(2)			**Na6**	2.51(2)									
	W4	2.58(4)			**W8**	2.94(7)									
	W5	3.00(13)			**W8**	2.51(6)	X3								
	W8	2.76(4)													
	W8	2.36(6)													
W4	**O1**	2.84(3)													
	O4	2.82(2)													
	Na6	2.83(2)													
	W3	2.58(4)													
	W5	2.93(11)													
	W5	2.70(12)													
	W8	2.76(3)													
W5	**W4**	2.93(11)													
	W4	2.70(12)													
	W5	2.93(14)	X2												
W6	**Na2'**	2.23(2)		**W6**	**Na2'**	2.73(2)		**W6**	**Na2'**	2.623(12)		**W6**	**Na2'**	2.64(2)	x3
	W6	2.550(4)	X3		**Na3**	2.94(1)			**W6**	2.551(3)	x2		**W6**	2.495(34)	x2
					W6	3.05(3)			**W6**	2.547(3)			**W6**	2.491(34)	
								W7	**Na6**	2.738(12)	x3	**W7**	**Na6**	3.11(2)	x3
									W7	2.96(2)			**W9**	2.30(9)	x3
									W9	2.598(5)	x3		**O12**	2.19(5)	x3
									W10	3.00(2)	x3				
									O11	2.910(3)	x3				
									O11	3.034(2)	x3				
									O12	2.507(2)	x3				
W8	**Na6**	2.26(2)		**W8**	**W3**	2.94(7)						**W8**	**O1**	2.75(3)	
	W3	2.76(4)			**W3**	2.51(6)							**Na6**	2.31(4)	
	W3	2.36(6)											**C11**	3.05(5)	
	W4	2.76(3)											**C11**	2.33(3)	
	W5	2.31(10)											**O11**	3.08(4)	
													O11	2.79(3)	
													O12	3.12(3)	
													O13	2.67(5)	
								W9	**Na6**	3.053(10)		**W9**	**Na6**	3.19(1)	
									W7	2.598(5)			**W9**	2.82(13)	x2
									W9	2.79(1)	x2		**O12**	2.94(4)	
									W9	3.17(2)	x2		**O12**	3.12(4)	
									O12	2.953(3)			**O13**	2.99(4)	
									O13	2.943(8)					
								W10	**O1**	3.149(13)					
									Na6	2.073(8)					
									W7	3.00(2)					

			C1	2.66(2)							
			O11	2.96(5)							
			O11	2.64(2)							
			O12	3.16(2)							
		C11	**O1**	2.699(8)			**C11**	**O1**	2.88(4)		
			O4	2.635(4)				**O4**	2.50(4)		
			Na6	3.030(12)				**Na6**	3.04(3)		
			Na6	3.060(7)				**Na6**	2.87(1)		
			W10	2.66(2)				**W10**	3.05(5)		
			O11	1.300(5)				**W10**	2.33(3)		
			O12	1.25(5)				**O11**	1.25(2)		
			O13	1.34(2)				**O12**	1.29(5)		
								O13	1.27(4)		
		O11	**O1**	2.950(8)			**O11**	**O1**	2.87(4)		
			O4	2.615(3)				**O4**	2.81(4)		
			Na6	2.726(12)				**Na6**	2.26(3)		
			Na6	2.399(8)				**Na6**	2.575(9)		
			W7	3.034(5)				**W10**	3.08(4)		
			W7	2.910(5)				**W10**	2.79(3)		
			W10	2.96(5)				**C11**	1.25(2)		
			W10	2.64(2)				**O11**	2.48(3)		
			C11	1.300(5)				**O12**	1.73(3)		
			O11	2.59(2)	x2			**O12**	2.87(4)	x2	
			O12	1.89(2)				**O13**	2.43(5)		
			O13	2.62(3)							
		O12	**Na6**	2.448(9)			**O12**	**Na6**	2.370(8)		
			Na6	2.526(7)				**Na6**	2.50(2)		
			W7	2.507(2)				**Na6**	2.83(1)		
			W9	2.953(3)				**W9**	2.94(4)		
			W10	3.16(2)				**W9**	3.12(4)		
			C1	1.25(5)				**W10**	3.12(3)		
			O11	1.89(2)				**C11**	1.29(5)		
			O12	2.79(2)				**O11**	1.73(3)		
			O13	1.96(5)				**O11**	2.87(4)		
								O13	1.91(6)		
		O13	**O1**	2.731(9)			**O13**	**O1**	2.94(3)		
			O1	2.971(9)				**O4**	2.89(4)		
			O4	3.067(8)				**Na6**	3.05(2)		
			Na6	3.041(11)				**W9**	2.99(4)		
			W9	2.943(8)				**W10**	2.67(5)		
			C1	1.34(2)				**C11**	1.27(4)		
			O11	2.62(3)				**O11**	2.43(5)		
			O12	1.96(5)				**O12**	1.91(6)		

T2b

RT				D-RT				CO$_2$				AP			
T1	**O1**	1.714(3)		**T1**	**O1**	1.647(4)		**T1**	**O1**	1.666(4)		**T1**	**O1**	1.671(4)	
	O2	1.666(3)			**O2**	1.661(4)			**O2**	1.649(3)			**O2**	1.660(4)	
	O3	1.671(3)			**O3**	1.665(3)			**O3**	1.646(3)			**O3**	1.661(4)	
	O4	1.652(3)			**O4**	1.648(4)			**O4**	1.640(3)			**O4**	1.632(2)	
Na2'	**O3**	2.839(7)	x3	**Na2'**	**O2**	3.071(8)	x3	**Na2'**	**O2**	2.999(6)	x3	**Na2'**	**O2**	3.043(7)	x3
	W1	2.239(3)	x6		**O3**	2.724(8)	x3		**O3**	2.457(6)	x3		**O3**	2.456(7)	x3
					W6	2.39(3)	x3		**W6**	2.62(2)	x3		**W6**	2.69(1)	x3
Na2	**O2**	2.990(5)	x3	**Na2**	**O2**	2.818(6)	x3	**Na2**	**O2**	2.888(6)	x3	**Na2**	**O2**	2.935(7)	x3
	O3	2.177(6)	x3		**O3**	2.220(7)	x3		**O3**	2.199(6)	x3		**O3**	2.175(7)	x3
	W1	3.08(1)	x6												
Na3	**O2**	2.492(5)	x3	**Na3**	**O2**	2.437(7)	x3	**Na3**	**O2**	2.450(6)	x3	**Na3**	**O2**	2.377(7)	x3
	O4	3.082(7)	x3		**O4**	3.005(9)	x3		**O4**	3.001(8)	x3		**O4**	2.966(8)	x3
	W3	3.106(1)	x6		**W6**	2.71(1)			**W6**	2.98(1)			**W6**	2.656(7)	
W1	**T1**	2.583(2)	x2						**O21**	2.39(1)			**O21**	2.41(1)	x3
	O2	2.688(6)	x2						**O42**	3.21(1)			**O42**	3.36(1)	x3
	O3	2.396(7)	x2												
	O4	2.710(7)													
	Na2'	2.239(3)													
	Na2	3.08(1)													
	W1	2.7(2)													
W2	**W2**	3.16(2)	x2	**W2**	**O1**	2.767(8)									
	W3	3.17(2)	x2		**O4**	3.059(9)									
	W3	2.93(1)	x2		**W2**	2.46(3)	x2								
	W4	3.03(1)	x2												
W3	**Na3**	3.106(1)						**W3**	**W3**	2.45(1)		**W3**	**W3**	2.26(7)	
	W2	3.17(2)							**C2**	2.98(1)			**C2**	3.12(3)	
	W2	2.93(1)							**O21**	3.16(2)			**O21**	2.89(4)	
	W4	3.14(2)							**O22**	2.49(1)			**O22**	2.44(3)	
	W5	2.87(1)							**O22**	2.89(1)			**O22**	2.97(3)	
									C3	2.98(1)			**C3**	3.15(3)	
									C3	2.81(2)			**C3**	2.77(4)	
									O42	3.11(2)			**C4/O41**	3.00(5)	
									C4/O41	3.01(2)					
W4	**O4**	3.112(8)													
	W2	3.03(1)	x2												
	W3	3.14(2)	x2												
	W4	2.99(3)													
W5	**W3**	2.87(1)	x6												
	W5	2.82(4)	x3												
				W6	**O2**	2.925(9)	x3	**W6**	**O2**	3.02(3)	x3	**W6**	**O2**	2.89(1)	x3

	Na2'	2.39(2)	x3		**Na2'**	2.62(2)	x3		**Na2'**	2.69(1)	x3
	Na3	2.71(1)			**Na3**	2.98(1)			**Na3**	2.656(7)	
	W6	3.19(2)	x3		**W6**	3.01(7)	x3				
				C2	**W3**	2.98(1)		**C2**	**W3**	3.12(3)	x2
					O21	1.180(3)			**O21**	1.18(1)	
					O22	1.181(3)			**O22**	1.18(1)	
					O32	3.09(5)	x2		**O32**	2.91(20)	x2
				O21	**Na3**	2.39(1)		**O21**	**Na3**	2.41(1)	
					W3	3.16(2)			**W3**	2.89(4)	x2
					C2	1.180(3)			**C2**	1.18(1)	
					O22	2.35(1)			**O22**	2.83(10)	x2
									O22	2.35(11)	
				O22	**W3**	2.49(1)		**O22**	**W3**	2.44(3)	
					W3	2.89(1)			**W3**	2.97(3)	
					C2	1.181(3)			**C2**	1.18(1)	
					O21	2.35(1)			**O21**	2.35(11)	
					O22	2.52(2)	x2		**O21**	2.83(10)	
					O22	2.91(3)	x2		**O22**	2.52(7)	x2
					O42	3.04(5)			**O22**	2.91(7)	x2
				C3	**O4**	3.14(1)		**C3**	**W3**	3.15(3)	x2
					W3	2.98(1)			**W3**	2.77(4)	x2
					W3	2.81(2)			**O31**	1.184(7)	
					O31	1.17(1)			**O32**	1.184(7)	
					O32	1.185(3)					
				O31	**O4**	3.15(1)		**O31**	**O4**	3.16(1)	
					C3	1.17(1)			**C3**	1.184(7)	
					O31	2.54(4)	x2		**O31**	2.45(5)	x2
					O32	2.35(1)			**O32**	2.34(2)	
				O32	**C2**	3.09(5)		**O32**	**C2**	2.91(20)	x2
					C3	1.185(3)			**C3**	1.184(7)	
					O31	2.35(1)			**O31**	2.34(2)	x3
					O42	2.52(1)			**O42**	2.53(3)	x2
				C4/O41	**W3**	3.01(2)		**C4/O41**	**W3**	3.00(5)	
					C4/O41	1.181(5)			**C4/O41**	1.181(7)	
					O42	2.36(1)			**O42**	2.36(1)	
					O42	1.182(5)			**O42**	1.181(2)	
				O42	**O1**	3.02(1)	x2	**O42**	**O1**	2.838(2)	x2
					O2	2.93(1)			**O2**	2.79(1)	
					Na3	3.21(1)			**Na3**	3.36(1)	
					W3	3.11(2)			**O32**	2.53(3)	x2
					O22	3.04(5)			**C4/O41**	2.36(1)	
					O32	2.52(1)	x2		**C4/O41**	1.181(7)	
					C4/O41	2.36(1)					
					C4/O41	1.182(5)					

Figures S1: Observed (red dash marks), calculated (green line) diffraction patterns and final difference curve (purple line) from Rietveld refinements for Na-X-RT (S1a); Na-Y-RT(S1b); Na-X-D-RT (S1c); Na-Y-D-RT (S1d); Na-X-CO2 (S1e), Na-Y-CO2 (S1f); Na-X-AP (S1g); Na-Y-AP (S1h).

S1a:

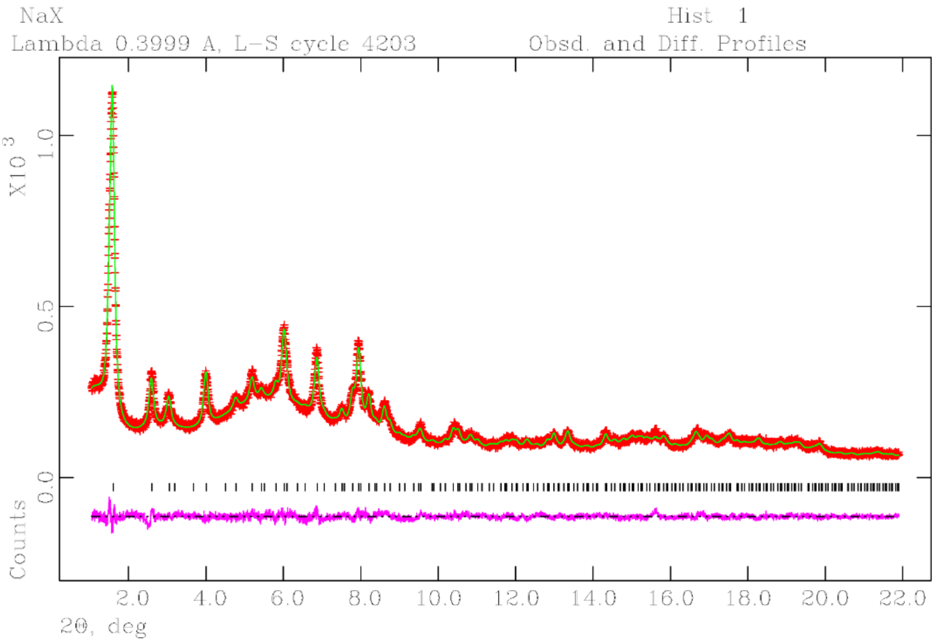

S1b:

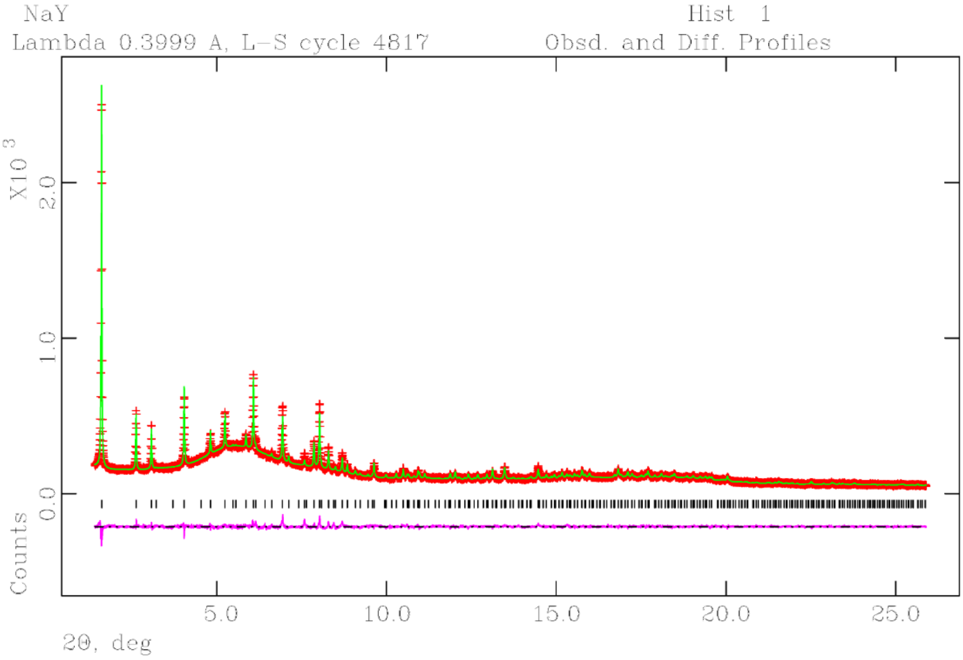

S1c:

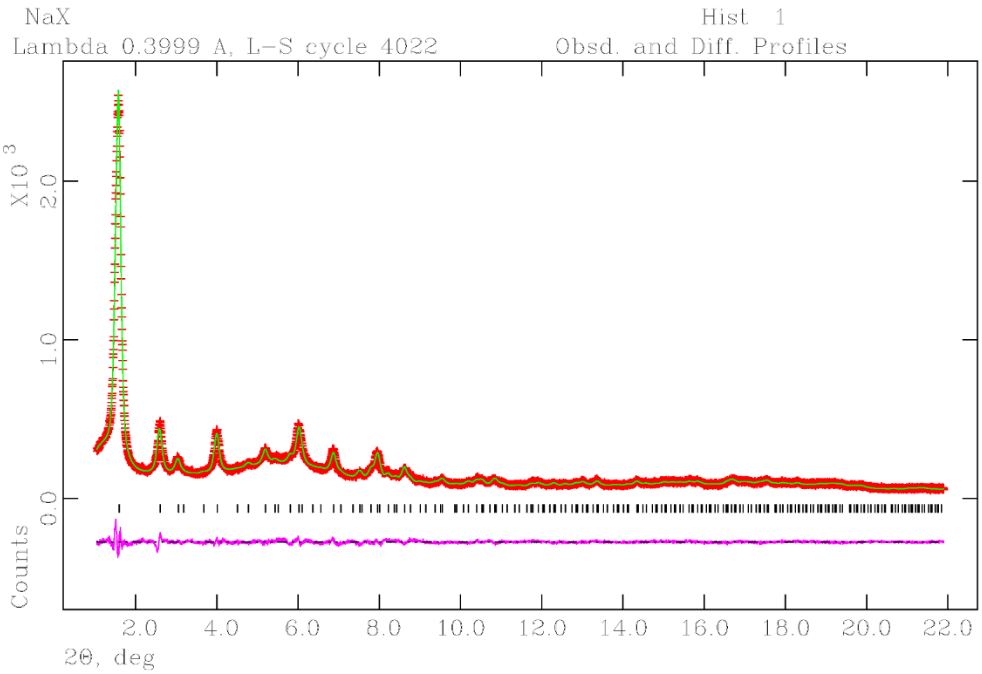
NaX
Lambda 0.3999 A, L-S cycle 4022
Hist 1
Obsd. and Diff. Profiles
X10 3
Counts
0.0
1.0
2.0
2.0
4.0
6.0
8.0
10.0
12.0
14.0
16.0
18.0
20.0
22.0
2Θ, deg

S1d:

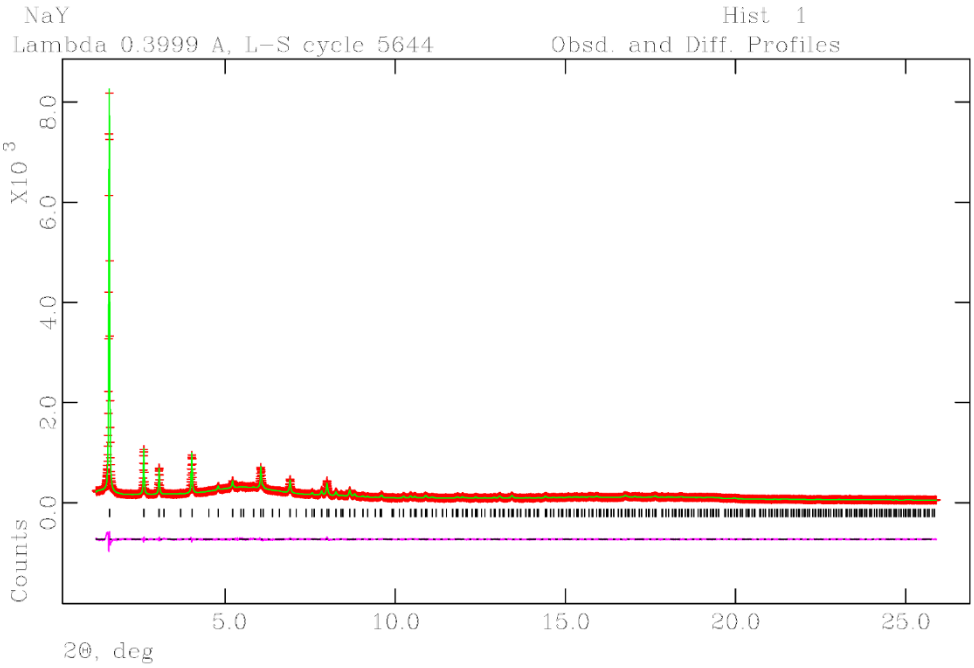
NaY
Lambda 0.3999 A, L-S cycle 5644
Hist 1
Obsd. and Diff. Profiles
X10 3
Counts
0.0
2.0
4.0
6.0
8.0
5.0
10.0
15.0
20.0
25.0
2Θ, deg

S1e:

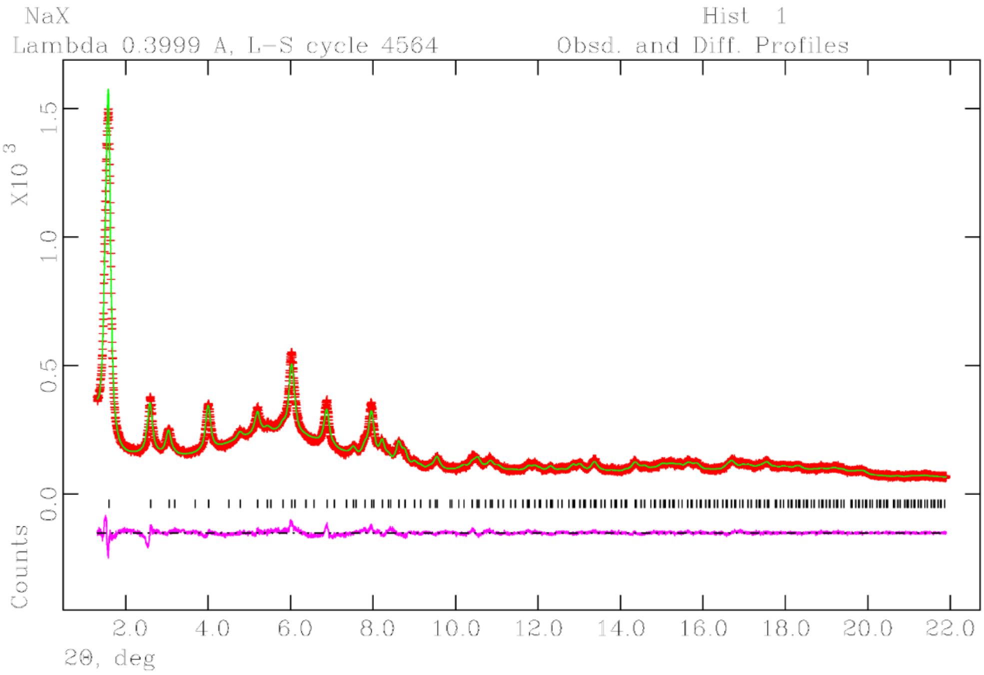
NaX
Hist 1
Lambda 0.3999 A, L-S cycle 4564
Obsd. and Diff. Profiles
X10 3
Counts
0.0
0.5
1.0
1.5
2.0
4.0
6.0
8.0
10.0
12.0
14.0
16.0
18.0
20.0
22.0
2Θ, deg

S1f:

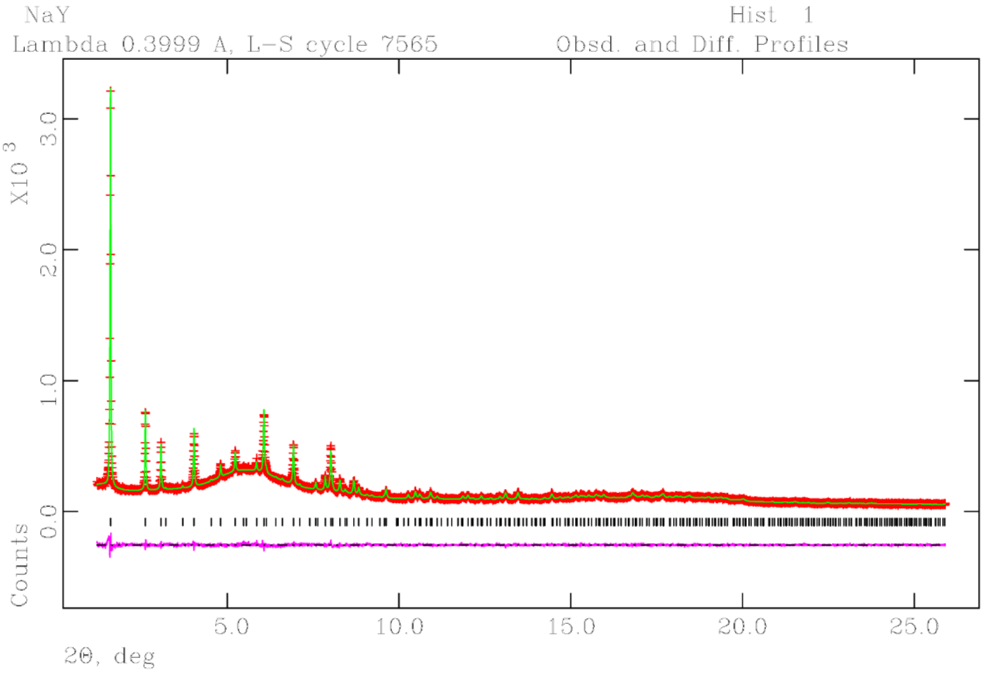
NaY
Hist 1
Lambda 0.3999 A, L-S cycle 7565
Obsd. and Diff. Profiles
X10 3
Counts
0.0
1.0
2.0
3.0
5.0
10.0
15.0
20.0
25.0
2Θ, deg

S1g:

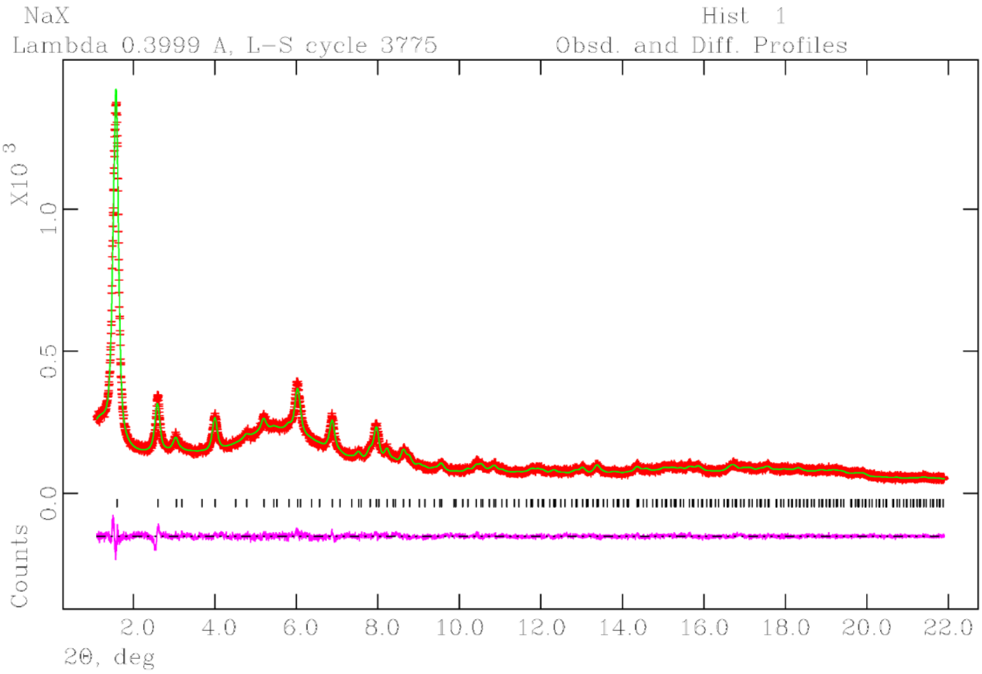
NaX
Lambda 0.3999 A, L-S cycle 3775
Hist 1
Obsd. and Diff. Profiles
X10 3
Counts
1.0
0.5
0.0
2.0
4.0
6.0
8.0
10.0
12.0
14.0
16.0
18.0
20.0
22.0
2Θ, deg

S1h:

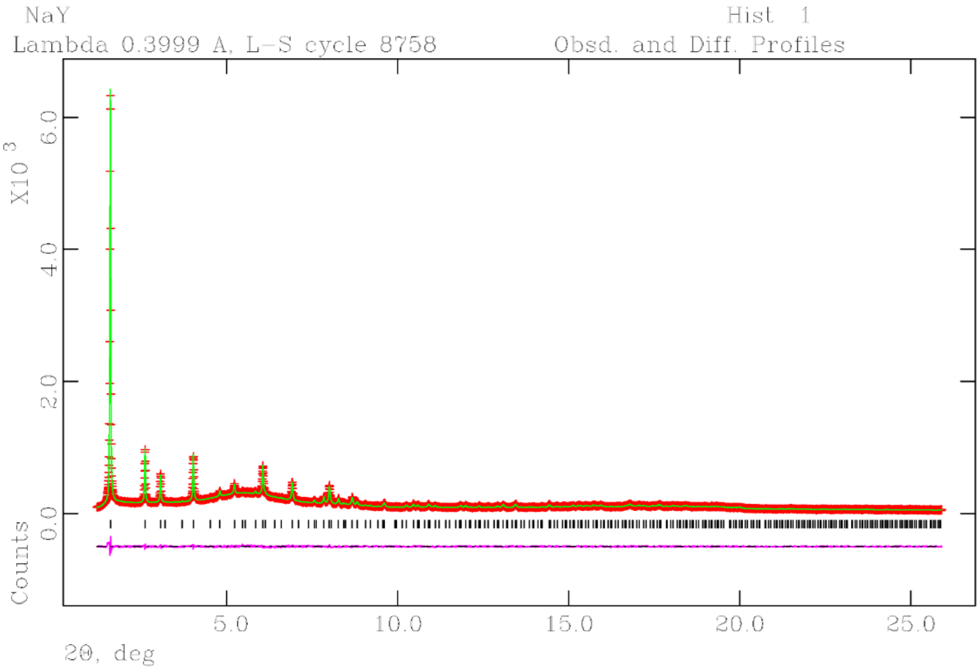
NaY
Lambda 0.3999 A, L-S cycle 8758
Hist 1
Obsd. and Diff. Profiles
X10 3
Counts
6.0
4.0
2.0
0.0
5.0
10.0
15.0
20.0
25.0
2Θ, deg

Tables T3: Atomic fractional coordinates, occupancy factors and thermal isotropic parameters (Å^2) of Na-MOR (T3a), Na-MOR+gly in capillary (T3b), Na-MOR+gly_P_{amb} in DAC (T3c) and Na-MOR+gly_P_{amb}R. * symbols in framework coordinates indicate position generated by symmetry lowering the symmetry from *Cmcm* to $Cmc2_1$. Letter "g" identifies oxygen atoms of glycine molecule.

T3a

Na-MOR						
atoms	**x**	**y**	**z**	**frac**	**Uiso**	**mult**
T1	0.304(1)	0.0685(9)	0.026(3)	1	0.018(1)	8
T1*	-0.307(1)	-0.0753(9)	-0.063(3)	1	0.018(1)	8
T2	0.3080(7)	0.3083(6)	0.045(3)	1	0.018(1)	8
T2*	-0.3027(8)	-0.3116(5)	-0.049(3)	1	0.018(1)	8
T3	0.0916(6)	0.3841(5)	0.242(4)	1	0.018(1)	8
T4	0.0841(6)	0.2213(5)	0.212(3)	1	0.018(1)	8
O1	0.122(2)	0.410(2)	0.434(4)	1	0.028(2)	8
O1*	-0.121(2)	-0.413(2)	-0.449(4)	1	0.028(2)	8
O2	0.147(1)	0.196(2)	0.361(3)	1	0.028(2)	8
O2*	-0.114(1)	-0.195(2)	-0.486(4)	1	0.028(2)	8
O3	-0.241(2)	-0.124(1)	-0.987(5)	1	0.028(2)	8
O3*	0.238(2)	0.123(1)	0.025(5)	1	0.028(2)	8
O4	0.089(1)	0.3024(6)	0.260(5)	1	0.028(2)	8
O5	0.162(1)	0.190(2)	0.750(3)	1	0.028(2)	8
O6	0.163(1)	0.417(1)	0.729(3)	1	0.028(2)	8
O7	0.272(1)	-0.006(1)	0.010(5)	1	0.028(2)	8
O8a	0.2401	0.2602	0.532	0.25	0.028(2)	8
O8b	-0.2401	-0.2602	-0.532	0.25	0.028(2)	8
O8c	0.2446	0.2521	0.48	0.25	0.028(2)	8
O8d	-0.2446	-0.2521	-0.48	0.25	0.028(2)	8
O9	0	0.407(1)	0.227(8)	1	0.028(2)	4
O10	0	0.184(1)	0.198(6)	1	0.028(2)	4
Na1	0	-0.495(3)	0.492(8)	0.51(1)	0.04(1)	4
Na3	0.028(2)	0.198(1)	0.680(6)	0.353(7)	0.05(2)	8
W1	0	0.429(2)	0.719(5)	1	0.109(9)	4
W2	0.113(2)	-0.003(3)	0.296(5)	0.64(3)	0.109(9)	8
W3	0	0.095(1)	0.491(4)	1	0.109(9)	4
W4	0.111(3)	0.004(6)	-0.083(7)	0.36(3)	0.109(9)	8
W6	0.5	0.192(1)	0.22(2)	0.66(2)	0.109(9)	4
W7	0.5	0.482(1)	0.615(5)	1	0.109(9)	4
W10	0.5	0.4146(8)	0.323(4)	1	0.109(9)	4

T3b

Na-MOR+gly						
atoms	**x**	**y**	**z**	**frac**	**Uiso**	**mult**
T1	0.3015(7)	0.0732(7)	0.082(3)	1	0.017(1)	8
T1*	-0.3093(7)	-0.0734(6)	0.002(3)	1	0.017(1)	8
T2	0.3054(7)	0.3135(7)	0.110(4)	1	0.017(1)	8
T2*	-0.3031(7)	0.3054(7)	0.008(3)	1	0.017(1)	8
T3	0.0859(5)	0.3843(4)	0.295(4)	1	0.017(1)	8
T4	0.0886(4)	0.2250(5)	0.278(4)	1	0.017(1)	8
O1	0.122(1)	0.408(1)	0.484(4)	1	0.025	8
O1*	-0.115(1)	-0.422(1)	-0.383(4)	1	0.025	8
O2	0.139(1)	0.201(1)	0.446(4)	1	0.025	8
O2*	-0.123(1)	-0.179(1)	-0.380(4)	1	0.025	8
O3	0.236(1)	0.128(1)	0.073(4)	1	0.025	8
O3*	-0.247(1)	-0.123(1)	-0.921(4)	1	0.025	8
O4	0.099(1)	0.3050(4)	-0.281(7)	1	0.025	8
O5	0.1625(7)	0.198(1)	0.809(3)	1	0.025	8
O6	0.1735(7)	0.4214(5)	0.790(3)	1	0.025	8
O7	0.2772(6)	-0.004(8)	0.073(3)	1	0.025	8
O8	0.257(1)	0.243(1)	0.580(4)	1	0.04	8
O9	0	0.410(1)	0.29(1)	1	0.025	4
O10	0	0.207(2)	0.296(6)	1	0.025	4
Na1	0	-0.493(5)	0.518(9)	0.43(1)	0.03(2)	4
Na3	0	0.232(1)	0.762(6)	0.78(1)	0.05(2)	4
W4	0.357(1)	0.514(4)	-0.033(8)	0.43(2)	0.05(3)	8
C1	0	-0.082(2)	0.16(1)	0.32(1)	0.08	4
O1g	0.5	0.391(6)	0.01(1)	0.32(1)	0.08	4
O2g	0	0.112(6)	-0.19(1)	0.32(1)	0.08	4
C2	0	-0.007(3)	0.20(2)	0.32(1)	0.08	4
N	0.5	0.435(4)	0.68(2)	0.32(1)	0.08	4
W1	0.5	0.918(2)	0.75(1)	0.83(2)	0.11(3)	4

T3c

Na-MOR+gly_P_{amb}						
atoms	**x**	**y**	**z**	**frac**	**Uiso**	**mult**
T1	0.297(1)	0.0666(9)	0.070(4)	1	0.008(3)	8
T1*	-0.3133(9)	-0.0780(5)	-0.026(4)	1	0.008(3)	8
T2	0.2981(8)	0.3108(8)	0.069(5)	1	0.008(3)	8
T2*	-0.3053(7)	-0.308(1)	-0.032(5)	1	0.008(3)	8
T3	0.0846(5)	0.3853(5)	0.313(4)	1	0.008(3)	8
T4	0.0866(6)	0.2270(5)	0.268(5)	1	0.008(3)	8
O1	0.125(2)	0.404(2)	0.501(4)	1	0.018(4)	8
O1*	-0.134(1)	-0.415(1)	-0.351(4)	1	0.018(4)	8
O2	0.137(1)	0.190(2)	0.418(4)	1	0.018(4)	8
O2*	-0.117(1)	-0.204(3)	-0.427(5)	1	0.018(4)	8
O3	0.238(2)	0.1254(12)	1.031(5)	1	0.018(4)	8
O3*	-0.237(1)	-0.119(1)	-0.991(6)	1	0.018(4)	8
O4	0.096(1)	0.3065(6)	0.285(11)	1	0.018(4)	8
O5	0.1638(7)	0.1808(8)	0.765(5)	1	0.018(4)	8
O6	0.1645(9)	0.4204(12)	0.763(4)	1	0.018(4)	8
O7	0.2729(6)	-0.0083(9)	0.018(4)	1	0.018(4)	8
O8	0.247(2)	0.2474(12)	0.466(6)	1	0.018(4)	8
O9	0	0.4130(12)	0.466(6)	1	0.018(4)	4
O10	0	0.205(2)	0.278(14)	1	0.018(4)	4
Na1	0	-499(8)	0.506(15)	0.504(8)	0.07(3)	4
Na3	0	0.2414(9)	0.721(5)	0.93(1)	0.13(2)	4
W4	0.364(1)	0.536(3)	-0.056(13)	0.49(2)	0.09(8)	8
C1	0	-0.077(2)	0.170(10)	0.390(6)	0.15(4)	4
O1g	0.5	0.402(4)	0.011(12)	0.390(6)	0.15(4)	4
O2g	0	0.115(4)	-0.196(14)	0.390(6)	0.15(4)	4
C2	0	-0.003(2)	0.174(11)	0.390(6)	0.15(4)	4
N	0.5	0.468(5)	0.851(16)	0.390(6)	0.15(4)	4
W1	0.5	0.927(2)	0.769(18)	0.94(2)	0.04(2)	4

T3d

Na-MOR+gly_P_{amb}R						
atoms	**x**	**y**	**z**	**frac**	**Uiso**	**mult**
T1	0.2962(1)	0.0666(1)	0.0701(4)	1	0.007(4)	8
T1*	-0.3129(1)	-0.0782(1)	-0.0262(3)	1	0.007(4)	8
T2	0.2980(1)	0.3107(1)	0.0697(3)	1	0.007(4)	8
T2*	-0.3053(1)	-0.3083(1)	-0.0326(3)	1	0.007(4)	8
T3	0.0849(1)	0.3854(1)	0.3130(3)	1	0.007(4)	8
T4	0.0869(1)	0.2268(1)	0.2680(3)	1	0.007(4)	8
O1	0.1311(8)	0.394(1)	0.4984(9)	1	0.015(6)	8
O1*	-0.1344(5)	-0.4150(4)	-0.3505(8)	1	0.015(6)	8
O2	0.1379(4)	0.1896(4)	0.4166(8)	1	0.015(6)	8
O2*	-0.1174(3)	-0.1992(11)	-0.423(1)	1	0.015(6)	8
O3	0.2357(5)	0.1244(4)	1.031(2)	1	0.015(6)	8
O3*	-0.2364(2)	-0.1185(3)	-0.990(2)	1	0.015(6)	8
O4	0.0961(15)	0.3056(3)	0.305(7)	1	0.015(6)	8
O5	0.1634(3)	0.1815(6)	0.7652(3)	1	0.015(6)	8
O6	0.1651(3)	0.4198(6)	0.7630(3)	1	0.015(6)	8
O7	0.2727(3)	-0.0083(1)	0.0173(7)	1	0.015(6)	8
O8	0.2453(7)	0.2485(5)	0.4669(9)	1	0.015(6)	8
O9	0	0.4100(7)	0.345(4)	1	0.015(6)	4
O10	0	0.2049(13)	0.277(21)	1	0.015(6)	4
Na1	0	-0.499(7)	0.51(4)	0.41(2)	0.04(4)	4
Na3	0	0.220(2)	0.728(12)	0.88(3)	0.10(4)	4
W4	0.3302(2)	0.5265(2)	-0.2243(4)	0.44(2)	0.08	8
C1	0	-0.083(4)	0.210(34)	0.30(1)	0.1	4
O1g	0.5	0.395(8)	0.05(4)	0.30(1)	0.1	4
O2g	0	0.120(8)	-0.15(4)	0.30(1)	0.1	4
C2	0	-0.008(4)	0.212(29)	0.30(1)	0.1	4
N	0.5	0.473(9)	0.887(33)	0.30(1)	0.1	4
W1	0.5	0.898(2)	0.866(10)	0.84(4)	0.10(5)	4

Table T4: Selected framework and extraframework distances (Å) for Na-MOR in capillary, Na-MOR+gly in capillary, Na-MOR+gly at ambient pressure inside the DAC and Na-MOR+gly at ambient pressure inside the DAC after pressure release. Only distances shorter than 3.2 Å are reported.

Na-MOR				**Na-MOR+gly**				**Na-MOR+gly_P_{amb}**				**Na-MOR+gly_P_{amb}R**			
T1	**O1**	1.57(1)		**T1**	**O1**	1.618(5)		**T1**	**O1**	1.630(1)		**T1**	**O1**	1.630(1)	
	O3*	1.62(1)			**O3**	1.619(5)			**O3**	1.630(1)			**O3**	1.630(1)	
	O6	1.66(1)			**O6**	1.626(5)			**O6**	1.630(1)			**O6**	1.629(1)	
	O7	1.64(1)			**O7**	1.624(5)			**O7**	1.630(1)			**O7**	1.630(1)	
T1*	**O1***	1.57(1)		**T1***	**O1***	1.622(5)		**T1***	**O1***	1.629(1)		**T1***	**O1***	1.630(1)	
	O3	1.65(1)			**O3***	1.620(5)			**O3***	1.629(1)			**O3***	1.630(1)	
	O6	1.66(1)			**O6**	1.620(5)			**O6**	1.630(1)			**O6**	1.628(1)	
	O7	1.64(1)			**O7**	1.626(5)			**O7**	1.630(1)			**O7**	1.630(1)	
T2	**O2**	1.59(1)		**T2**	**O2**	1.615(5)		**T2**	**O2**	1.630(1)		**T2**	**O2**	1.630(1)	
	O3	1.66(1)			**O3***	1.619(5)			**O3***	1.629(1)			**O3***	1.630(1)	
	O5	1.63(1)			**O5**	1.617(5)			**O5**	1.630(1)			**O5**	1.629(1)	
	O8a	1.647(7)			**O8**	1.621(5)			**O8**	1.629(1)			**O8**	1.629(1)	
	O8b	1.672(7)													
	O8c	1.629(7)													
	O8d	1.631(7)													
T2*	**O2***	1.59(1)		**T2***	**O2***	1.618(5)		**T2***	**O2***	1.630(1)		**T2***	**O2***	1.628(1)	
	O3*	1.63(1)			**O3**	1.613(5)			**O3**	1.629(1)			**O3**	1.630(1)	
	O5	1.64(1)			**O5**	1.614(5)			**O5**	1.630(1)			**O5**	1.629(1)	
	O8a	1.657(7)			**O8**	1.615(5)			**O8**	1.630(1)			**O8**	1.629(1)	
	O8b	1.659(7)													
	O8c	1.618(7)													
	O8d	1.638(7)													
T3	**O1**	1.63(1)		**T3**	**O1**	1.624(5)		**T3**	**O1**	1.630(1)		**T3**	**O1**	1.630(1)	
	O1*	1.63(1)			**O1***	1.627(5)			**O1***	1.630(1)			**O1***	1.632(1)	
	O4	1.67(1)			**O4**	1.635(5)			**O4**	1.631(1)			**O4**	1.635(1)	
	O9	1.72(1)			**O9**	1.638(5)			**O9**	1.631(1)			**O9**	1.634(1)	
T4	**O2**	1.68(1)		**T4**	**O2**	1.628(5)		**T4**	**O2**	1.630(1)		**T4**	**O2**	1.631(1)	
	O2*	1.67(1)			**O2***	1.628(5)			**O2***	1.630(1)			**O2***	1.632(1)	
	O4	1.69(1)			**O4**	1.639(5)			**O4**	1.631(1)			**O4**	1.635(1)	
	O10	1.70(1)			**O10**	1.647(5)			**O10**	1.631(1)			**O10**	1.634(1)	
Na1	**O1**	2.96(4)	x2	**Na1**	**O1**	2.99(2)	x2	**Na1**	**O1**	3.00(4)	x2	**Na1**	**O1***	3.15(1)	x2
	O1*	2.80(4)	x2		**O1***	2.64(2)	x2		**O1***	3.14(3)	x2		**O9**	2.22(8)	
	O9	2.82(5)			**O9**	2.61(3)			**O9**	2.29(4)			**O9**	2.90(29)	

	O9	2.52(5)			**W1**	2.51(9)			**W1**	2.48(4)			**W1**	2.30(1)	
	W1	2.30(2)							**W1**	2.30(1)					
	W1	2.46(2)													
Na3	**O2***	2.94(3)		**Na3**	**O5**	3.04(3)	x2	**Na3**	**O2g**	2.64(2)		**Na3**	**O5**	3.07(1)	x2
	O5	2.47(2)	x2		**C1**	3.15(2)							**C1**	2.79(5)	
	W3	2.58(3)			**O1g**	3.12(3)							**O1g**	2.69(6)	
	W6	2.31(2)			**O2g**	2.46(2)							**O2g**	2.20(5)	
	W10	2.59(3)													
W1	**O1**	3.09(3)	x2												
	O6	2.95(2)	x2												
	Na1	2.3(2)													
	Na1	2.46(2)													
	W6	2.47(5)													
W2	**W4**	2.85(6)													
	W7	3.16(5)													
	W7	2.49(2)													
	W10	2.65(5)													
W3	**O10**	2.84(4)													
	Na3	2.58(3)	x2												
	W4	2.90(9)	x2												
	W7	2.49(2)													
	W10	2.50(1)													
W4	**O7**	3.00(2)		**W4**	**O3**	2.98(3)		**W4**	**O3**	2.66(3)		**W4**	**O3**	3.01(1)	
	W3	2.90(9)			**O7**	2.58(1)			**O7**	2.699(2)			**O3**	2.70(1)	
	W2	2.85(6)			**C2**	3.12(11)			**C2**	3.10(7)			**O5**	3.16(1)	
	W7	3.05(7)			**N**	3.2(1)			**N**	2.91(7)			**O7**	2.690(4)	
	W7	2.51(2)											**O7**	2.709(4)	
	W10	2.69(9)													
W6	**Na3**	2.31(2)	x2												
	W1	2.47(5)													
W7	**W3**	2.49(2)													
	W2	3.16(5)	x2												
	W2	2.49(2)	x2												
	W4	3.05(7)	x2												
	W4	2.51(2)	x2												
	W10	2.59(2)													
	W10	2.61(2)													
W10	**Na3**	2.59(3)	x2												
	W3	2.50(1)													
	W2	2.65(5)	x2												
	W4	2.69(9)	x2												
	W7	2.59(2)													

W7	2.61(2)												
		C1	**Na3**	3.15(2)		**C1**	**O1g**	1.265(1)		**C1**	**Na3**	2.79(5)	
			O1g	1.25(1)			**O2g**	1.267(1)			**O1g**	1.265(1)	
			O2g	1.25(1)			**C2**	1.516(1)			**O2g**	1.267(1)	
			C2	1.522(8)			**N**	2.56(1)			**C2**	1.516(1)	
											N	2.67(2)	
		O1g	**O10**	2.57(4)		**O1g**	**O10**	2.79(6)		**O1g**	**O10**	2.90(2)	
			Na3	3.12(3)			**C1**	1.265(1)			**Na3**	2.69(6)	
			C1	1.25(1)			**N**	1.80(11)			**C1**	1.265(1)	
			N	2.67(14)							**N**	2.00(21)	
		O2g	**Na3**	2.46(2)		**O2g**	**Na3**	2.64(2)		**O2g**	**O2***	3.17(2)	
			C1	1.25(1)			**W4**	3.12(7)	x2		**Na3**	2.20(5)	
			N	2.9(1)			**C1**	1.267(1)			**C1**	1.267(1)	
							N	3.02(1)			**N**	3.02(2)	
		C2	**W4**	3.1(1)	x2	**C2**	**W4**	3.10(7)	x2	**C2**	**C1**	1.516(1)	
			C1	1.52(1)			**C1**	1.516(1)			**N**	1.50(1)	
			N	1.482(8)			**N**	2.49(7)					
		N	**O10**	3.03(4)		**N**	**W4**	2.91(7)		**N**	**O1g**	2.00(21)	
			W4	3.2(1)	x2		**O2g**	3.02(1)			**O2g**	3.02(2)	
			O2g	2.9(1)			**C2**	2.9(7)			**C2**	1.50(1)	
			C2	1.482(8)									
		W1	**O1**	2.98(3)	x2	**W1**	**O1**	3.05(3)	x2	**W1**	**O6**	3.113(8)	x2
			O6	3.15(1)	x2		**O6**	2.98(2)	x2		**Na1**	2.300(1)	
			Na1	2.51(9)	x2		**Na1**	2.48(4)					
							Na1	2.30(1)					

Table T5: Unit cell parameters (Å) and unit cell volume (Å^3) for each pressure step in the four HP experiments in DAC: Na-MOR+gly in DAPHNE oil (T5a), Na-MOR+gly in Ar (T5b), Na-MOR+αala in DAPHNE oil (T5c), Na-MOR+ αala in Ar (T5d), (REV indicates data collected after pressure release).

T5a:

	P (Gpa)	***a***	***b***	***c***	***V***
P0	0	18.080(1)	20.348(1)	7.4908(4)	2755.9(4)
P1	0.44	17.999(5)	20.156(4)	7.445(1)	2701(1)
P2	1.02	17.781(2)	19.830(2)	7.337(1)	2587(1)
P3	1.57	17.539(8)	19.564(6)	7.255(2)	2489(2)
P4	2.06	17.43(1)	19.33(1)	7.222(4)	2432(3)
P5	2.7	-	-	-	-
P6REV	1.68	17.44(1)	19.42(1)	7.223(5)	2447(4)
P7REV	1.1	17.661(4)	19.718(3)	7.298(1)	2541(1)
P8REV	0	18.075(2)	20.337(2)	7.4877(6)	2752.4(6)

T5b:

	P (Gpa)	**a**	**b**	**c**	**V**
P0	0.07	18.051(1)	20.406(1)	7.4961(4)	2761.2(4)
P1	0.36	18.022(1)	20.365(1)	7.4831(4)	2746.5(4)
P2	0.92	17.977(3)	20.252(3)	7.4542(9)	2713.8(9)
P3	1.43	17.885(9)	20.097(8)	7.415(3)	2665(2)
P4REV	1.29	17.90(1)	20.126(9)	7.424(3)	2674(2)
P5REV	0.76	17.998(2)	20.312(2)	7.4684(7)	2730.3(7)
P6REV	0	18.080(1)	20.3681(9)	7.4926(3)	2759.2(3)

T5c:

	P (Gpa)	a	b	c	V
P1	0.59	18.022(3)	20.209(3)	7.4590(9)	2716.7(9)
P2	0.85	17.998(4)	20.177(4)	7.454(1)	2707(1)
P3	1.2	17.948(7)	20.075(8)	7.429(3)	2677(2)
P4	1.88	17.683(5)	19.801(9)	7.342(4)	2571(2)
P5	2.48	17.426(8)	19.50(1)	7.279(5)	2474(3)
P6	3.02	17.13(2)	19.08(2)	7.22(1)	2361(4)
P7REV	1.9	17.509(8)	19.58(1)	7.312(5)	2507(2)
P8REV	0.18	18.027(3)	20.233(3)	7.463(1)	2722(1)

T5d:

	P (Gpa)	a	b	c	V
P0	0.1	18.055(1)	20.382(1)	7.4926(4)	2757.3(4)
P1	0.32	18.044(2)	20.367(1)	7.4860(4)	2751.0(4)
P2	0.79	18.016(2)	20.317(2)	7.4703(6)	2734.4(6)
P3	1.1	18.005(2)	20.272(2)	7.4581(6)	2722.1(3)
P4	1.46	17.989(3)	20.221(2)	7.4440(8)	2707.9(4)
P5	1.77	17.981(4)	20.163(3)	7.429(1)	2693(1)
P6	2.13	17.959(8)	20.098(7)	7.411(3)	2675(2)
P7REV	0	18.056(4)	20.279(3)	7.478(1)	2738(1)

Figure S2: Observed (red dash marks) and calculated (green line) diffraction patterns and final difference curve (purple line) from Rietveld refinements for Na-MOR (S2a), Na-MOR+gly in capillary (S2b), Na-MOR+gly at ambient pressure inside the DAC (S2c) and Na-MOR+gly at ambient pressure inside the DAC after the pressure release (S2d).

S2a:

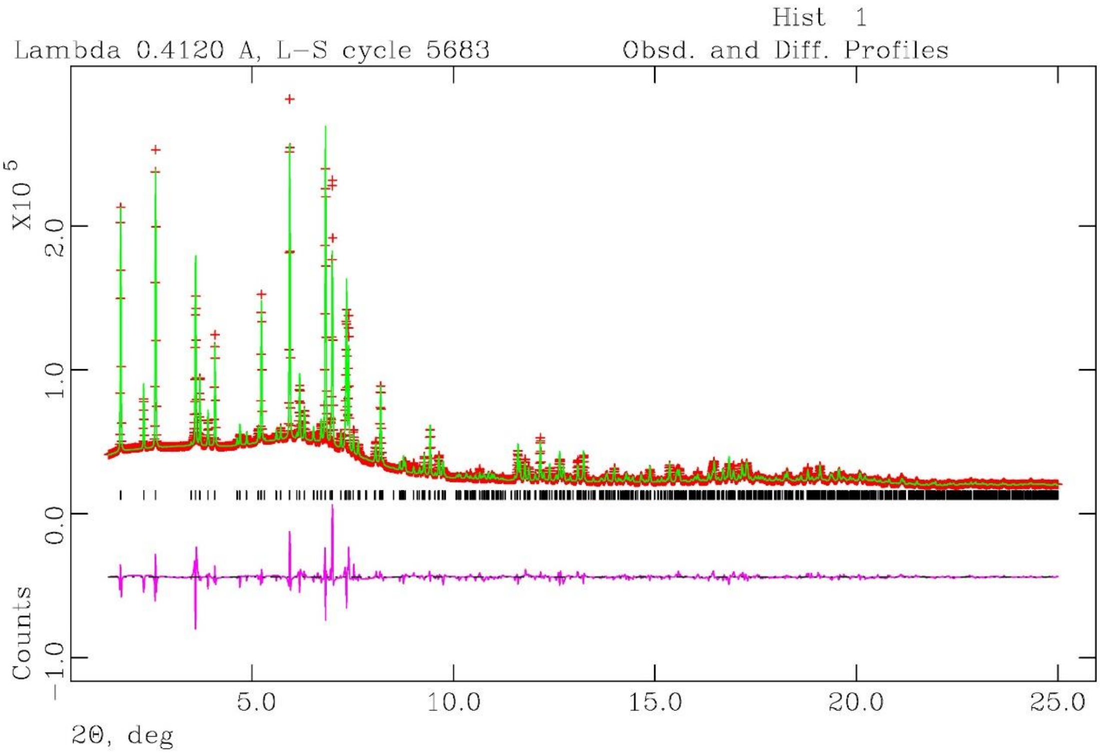

S2b:

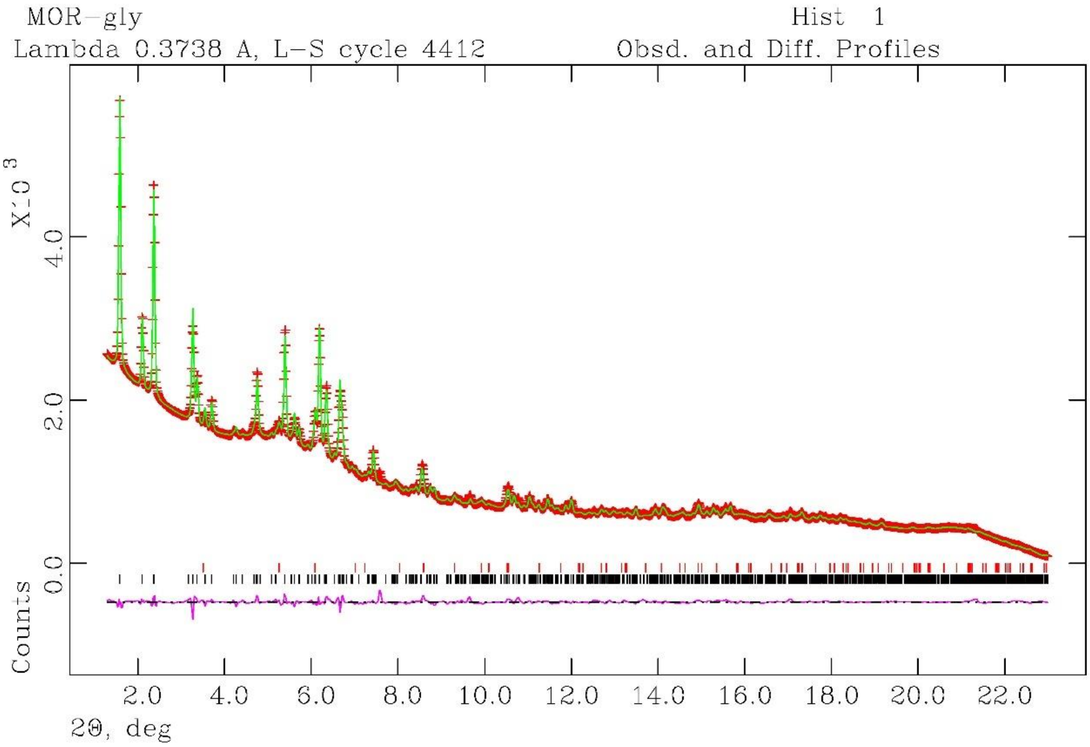
MOR–gly
Hist 1
Lambda 0.3738 A, L-S cycle 4412
Obsd. and Diff. Profiles
X10 3
Counts
0.0
2.0
4.0
2.0
4.0
6.0
8.0
10.0
12.0
14.0
16.0
18.0
20.0
22.0
2Θ, deg

S2c:

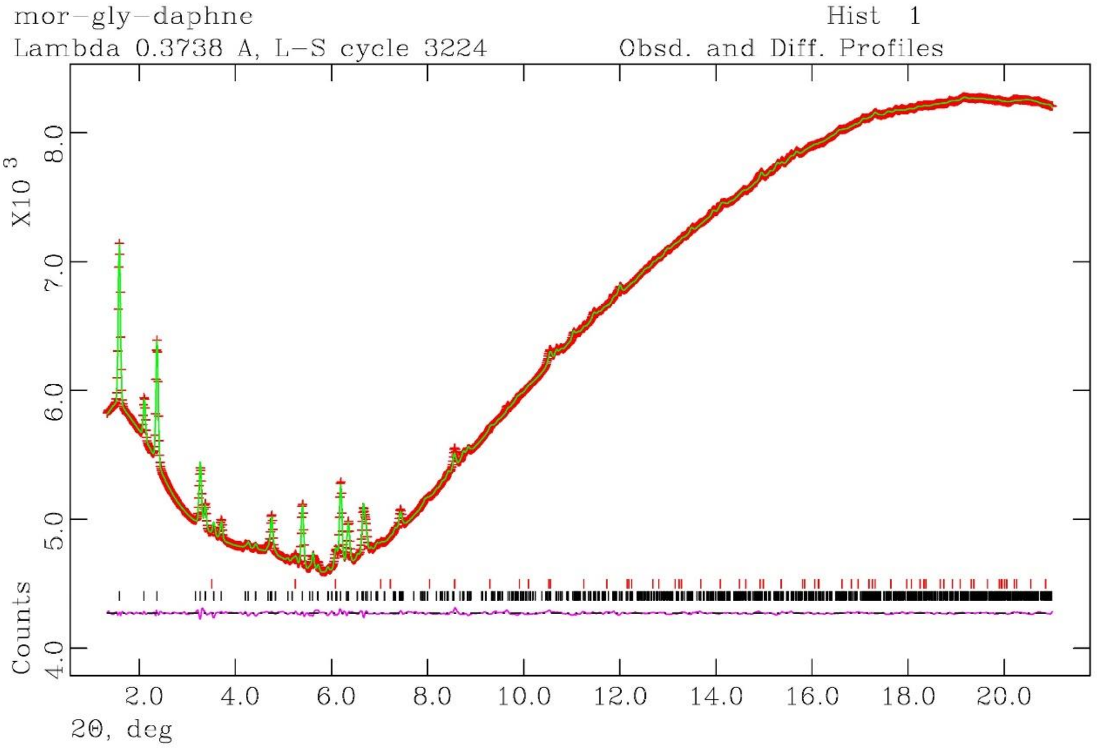
mor–gly–daphne
Hist 1
Lambda 0.3738 A, L-S cycle 3224
Obsd. and Diff. Profiles
X10 3
Counts
4.0
5.0
6.0
7.0
8.0
2.0
4.0
6.0
8.0
10.0
12.0
14.0
16.0
18.0
20.0
2Θ, deg

S2d:

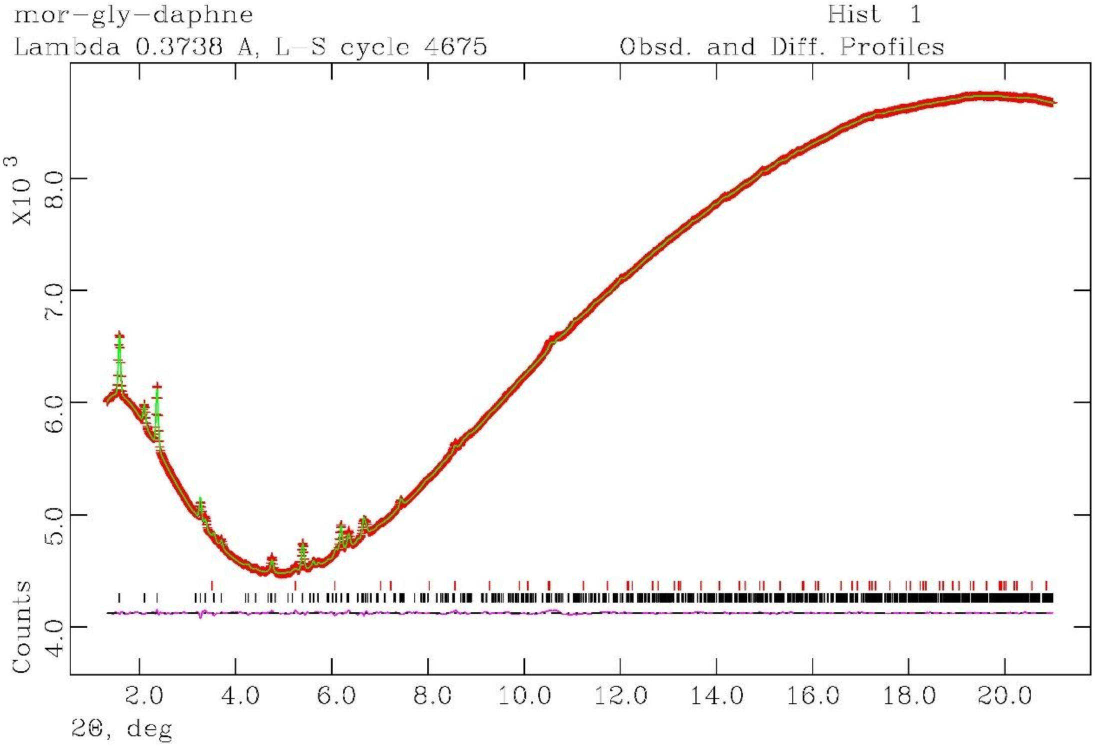
mor−gly−daphne
Hist 1
Lambda 0.3738 A, L−S cycle 4675
Obsd. and Diff. Profiles
X10 3
Counts
4.0
5.0
6.0
7.0
8.0
2.0
4.0
6.0
8.0
10.0
12.0
14.0
16.0
18.0
20.0
2Θ, deg

References

Alberti A., Davoli P. and Vezzalini G. (1986). The crystal structure refinement of a natural mordenite. *Zeitschrift für Kristallographie*, **175**, 249-256.

Anderson M.A. (2000). Removal of MTBE and other organic contaminants from water by sorption to high silica zeolites. *Environmental Science and Technology*, **34**, 725-727.

Anfray C., Dong B., Komaty S., Mintova S. and Valable S. (2017). Acute toxicity of silver free and encapsulated in nanosized zeolite for eukaryotic cells. *ACS Applied Materials & Interfaces*, **9**, 13849−13854.

Angell C. L. and Howell M. V. (1969). Infrared spectroscopic investigations of zeolites and adsorbed molecules. Part V. Carbon dioxide. *Canadian Journal of Chemistry*, **47**, 3831−3836.

Anzinelli P.R., Baú J.P.T., Valezi D.F., Canton L.C., Carneiro C.E.A., Di Mauro E., Da Costa A.C.S., Galante D., Braga A.H., Rodrigues F., Coronas J., Casado-Coterillo C., Zaia C.T.B.V and Zaia D.A.M. (2016). Adenine interaction with and adsorption on Fe-ZSM-5 zeolites: A prebiotic chemistry study using different techniques. *Microporous and Mesoporous Materials*, **226**, 493-504.

Arletti R., Fois E., Gigli L., Vezzalini G., Quartieri S. and Tabacchi G. (2017). Irreversible conversion of a water–ethanol solution into an organized two-dimensional network of alternating supramolecular units in a hydrophobic zeolite under pressure. *Angew. Chem. Int. Ed.,* **56**, 2105-2109.

Arletti R., Gigli L., Di Renzo F. and Quartieri S. (2016). Evidence for the formation of stable CO_2 hydrates in zeolite Na - Y: Structural characterization by synchrotron X- ray powder diffraction. *Microporous and Mesoporous Materials*, **228**, 248-255.

Bacakova L., Vandrovkova M., Kopova I. and Jirka I. (2018). Applications of zeolites in biotechnology and medicine – a review. *Biomaterials Science*, **6**, 974-989.

Balerna A. and Mobilio S. (2015). Introduction to synchrotron radiation. In Synchrotron radiation: Basics, methods and applications. (Mobilio S. and Boscherini F. ed.). *Springer*, 3-28.

Barnett J.D., Block S., Piermarini G.J. (1973). An optical fluorescence system for quantitative pressure measurement in the diamond-anvil cell. *Review of Scientific Instrumen*ts, **44**, 1-9.

Barrer R.M. (1978). Cation-exchange equilibria in zeolites and feldspathoids. In: natural Zeolites: occurrence, properties and use (Sand L.B., Mumpton F.A., Eds). Pergamon Press, New York (USA), pp. 385-395.

Baú J.P.T., Carneiro C.E.A., De Souza I.G.Jr., De Souza C.M.D., Da Costa A.C.S., Di Mauro E., Zaia C.T.B.V, Coronas J., Casado C., De Santana H. and Zaia D.A.M. (2012). Adsorption of adenine and thymine on zeolites: FT-IR and EPR spectroscopy and X-ray diffractometry and SEM study. *Origins of Life and Evolution of Biospheres*, **42**, 19-29.

Baur W.H. (1964). On the cation and water position in faujasite. *The American Mineralogist*, **49**, 697-704.

Baerlocher C., McCusker L.B. and Olson D.H. (2001). Atlas of zeolite framework types. Fifth revised edition. Elsevier Science, New York (USA).

Bein T. and Mintova S. (2005). Advanced application of zeolites. In: zeolites and ordered mesoporous materials: progress and prospects (Čejka J., van Bekkum H. ed.), Studies in Surface and Science Catalysis, **157**, 263-288.

Bergerhoff G., Baur W.H. and Nowacki W. (1956). Zur kristallstruktur der mineralien der chabazit-und der faujasitgruppe. *Experientia*, **12**, 418-419.

Bernal J.D. (1951). *The Physical basis of life* (Routledge & Paul, London).

Bertrand M., Van der Gaast S., Vilas F., Hörz F., Haynes G., Chabin A., Brack A. and Westall F. (2009). The fate of amino acids during simulated meteoritic impact. *Astrobiology*, **9**, 943-951.

Bertsch L. and Habgood H. W. (1963). An infrared spectroscopic study of the adsorption of water and carbon dioxide by linde molecular sieve X1. *Journal of Physical Chemistry*, **67**, 1621−1628.

Bish D.L. and Carey J.W. (2001). Thermal behavior of natural zeolites. In: Natural zeolites: occurrence, properties, applications (Bish D.L., Ming D.W.). *Reviews in Mineralogy and Geochemistry*, **45**, 403-452.

Blauwhoff P.M.M., Gosselink J.W., Kieffer E.P., Sie S.T. and Stork W.H.J. (1999). Zeolites as catalysts in industrial processes. In: Catalysis and zeolites, fundamentals and applications (Weitkamp J. and Puppe L.). pp. 198-326.

Bonenfant D., Kharoune M., Niquette P., Mimeault M. and Hausler R. (2008) Advances in principal factors influencing carbon dioxide adsorption on zeolites. *Science and Technology of Advanced Materials*, **9**, 013007-013013.

Brandani F. and Ruthven D. M. (2004). The Effect of Water on the Adsorption of CO_2 and C_3H_8 on Type X Zeolites. *Industrial & Engineering Chemistry Research*, **43**, 8339−8344.

Brunner G.O. and Meier W.M. (1989). Framework density distribution of zeolite-type tetrahedral nets. *Nature*, **337**, 146-147.

Busca G. (2017). Acidity and basicity of zeolites: A fundamental approach. *Microporous and Mesoporous Materials*, **254**, 3−16.

Calzaferri G. (2012). Nanochannels: hosts for the supramolecular organization of molecules and complexes. *Langmuir*, **28**, 15, 6216-6231.

Calzaferri G. and Lutkouskaya K. (2008). Mimicking the antenna system of green plant. *Photochemical & photobiological sciences*, **8**, 879-910.

Carneiro C.E.A., De Santana H., Casado C., Coronas J. and Zaia D.A.M. (2011). Adsorption of amino acids (Ala, Cys, His, Met) on zeolites: Fourier transform infrared and raman spectroscopy investigations. *Astrobiology*, **11**, 409-418.

Carrea G., Colonna S., Kelly D.R., Lazcano A., Ottolina G. and Roberts S. M. (2005). Polyamino acids as synthetic enzime: mechanism, applications and relevance to prebiotic catalysis. *Trends in Biotechnology*, **23**, 507-513.

Čejka J., Centi G., Perez-Pariente J. and Roth W.J. (2012). Zeolite-based materials for novel catalytic applications: opportunities, perspective and open problems. *Catalysis today*, **179**, 2-15.

Cheah W.-K., Ishikawa K., Othman R., Yeoh F.-Y. (2017). Nanoporous biomaterials for uremic toxin adsorption in artificial kidney systems: A review. *Journal of biomedical materials research B: applied biomaterials,* **105B**, 1232-1240.

Cheam T.C. and Krimm S. (1984). Vibrational analysis of crystalline diketopiperazine-I. Raman and I.R. spectra. *Spectrochimica Acta*, **40A**, 6, 481-501.

Chiku H., Matsui M., Murakami S., Kiyozumi Y., Mizukami F. and Sakaguchi K. (2003). Zeolites as new chromatographic carriers for proteins--easy recovery of proteins adsorbed on zeolites by polyethylene glycol. *Analytical Biochemistry*, **318**, 80-85.

Choi S., Drese J.H., and Jones C.W. (2009). Adsorbent materials for carbon dioxide capture from large anthropogenic point sources. *ChemSusChem*, **2**, 796-854.

Coin I., Beyermann M. and Bienert M. (2007). Solid-phase peptide synthesis: from standard procedures to the synthesis of difficult sequences. *Nature Protocols*, **2**, 3247–3256.

Colella C., de' Gennaro M. and Aiello R. (2001). Use of zeolitic tuff in the building industry. In: Natural zeolites: occurrence, properties, applications (Bish D.L., Ming D.W.). *Reviews in Mineralogy and Geochemistry*, **45**, 551-588.

Confalonieri G., Ryzhikov A., Arletti R., Nouali H., Quartieri S., Daou T.J. and Patarin J. (2018). Intrusion−Extrusion of electrolyte aqueous solutions in pure silica chabazite by in situ high pressure synchrotron X-ray powder diffraction. *The Journal of Physical Chemistry C*, **122**, 28001-28012.

Constable D.J.C., Dunn P.J., Hayler J.D., Humphrey G.R., Leazar J.L., Linderman R.J., Lorenz K., Manley J., Pearlman B.A., Wells A., Zaks A. and Zhang T.Y. (2007). Key green chemistry research areas-a perspective from pharmaceutical manufacturers. *Green Chemistry*, **9**, 411-420.

Coombs D.S., Alberti A., Armbruster T., Artioli G., Colella C., Galli E., Grice J.D., Liebau F., Mandarino J.A., Minato H., Nickel E.H., Passaglia E., Peacor D.R., Quartieri S., Rinaldi R., Ross M., Sheppard R.A., Tillmanns E., Vezzalini G. (1997). Recommended nomenclature for zeolite minerals: report of the subcommittee on zeolites of the International Mineralogical Association, Commission on New Minerals and Mineral Names. *The Canadian Mineralogist*, **35**, 1571-1606.

Corma A. (1989). Application of zeolites in fluid catalytic cracking and related processes. *Zeolites: Facts, Figures, Future*. P. A. Jacobs and R. A. van Santen (Editors), pp 49-67.

Corma A. and Fornes V. (2002). Delaminated zeolites: an effective support for enzymes. *Advanced materials*, **14**,1,71-74.

Corma A. and Martinez A. (1999). Catalysis on porous solids. In: Handbook of Porous Solids (Schuth F., Sing K.S.W. and J. Weitkamp, Eds). Wiley-VCH, Weinheim, vol. **5**, 2825-2922.

Corma A., Planellas J., Sánchez-Marin J. and Tomás F. (1985). The Role of different types of acid site in the cracking of alkanes on zeolite catalysts. *Journal of catalysis*, **93**, 30-37.

Cruciani G. (2006). Zeolites upon heating: factors governing their thermal stability and structural changes. *Journal of Physics and Chemistry of Solids*, **67**, 1973-1994.

Cundy C.S. (2005). Synthesis of zeolites and zeotypes. In: zeolites and ordered mesoporous materials: progress and prospects (Čejka J., van Bekkum H. ed.), Studies in Surface and Science Catalysis, **157**, 65-90.

Cundy C.S. and Cox P.A. (2003). The hydrothermal synthesis of zeolites: History and development from the earliest days to the present time. *Chemical Reviews*, **103**, 663-701.

Cundy C.S. and Cox P.A. (2005). The Hydrothermal Synthesis of Zeolites: precursors, intermediates and reaction mechanism. *Microporous and mesoporous materials*, **82**, 1-78.

Davis M.E. (2002). Ordered porous materials for emerging applications. *Nature*, **417**, 813-821.

Dempsey E., Kühl G.H. and Olson D.H. (1969). Variation of the lattice parameter with aluminum content in synthetic sodium faujasites. Evidence for ordering of the framework ions. *The Journal of Physical Chemistry*, **73**, 2, 387-390.

Di Renzo F. and Fajula F. (2005). Introduction to molecular sieves: trends of evolution of the zeolite community. In: zeolites and ordered mesoporous materials: progress and prospects (Čejka J., van Bekkum H. ed.), Studies in Surface and Science Catalysis, **157**, 1-12.

Dyer A. and Keir D. (1984). Nuclear waste treatment by zeolites, *Zeolites,* **4**, 215-217.

Erastova V., Degiacomi M.T., Fraser D.G. and Greenwell H.C. (2017). Mineral surface chemistry control for origin of prebiotic peptides. *Nature communications*, **8**, 2033.

Eroglu N., Emekci M. and Athanassiou C.G. (2017). Applications of natural zeolites on agriculture and food production. *Journal of the Science of Food and Agriculture*, **97**, 3487-3499.

Eroshenko V., Regis R.-C., Soulard M. and Patarin J. (2001). Energetics: A new field of applications for hydrophobic zeolites. *Journal of the American Chemical Society,* **123**, 33, 8129-8130.

Flanagan D.M. (2019). Zeolites (annual publications). U.S. Geological Survey, mineral commodity summaries.

Fletcher R.E., Ling S. and Slater B. (2017). *Chemical Science,* **8**, 7483-7491.

Forman R.A., Piermarini G., Barnett J. and Block S. (1972). Pressure measurement made by the utilization of ruby sharp-line luminescence. *Science,* **176**, 284-285.

Frising T. and Leflaive P. (2008). Extraframework cation distributions in X and Y faujasite zeolites: A review. *Microporous and Mesoporous Materials*, **114**, 27-63.

Fuchida S., H. Masuda and Shinoda K. (2014). Peptide formation mechanism on montmorillonite under thermal conditions. *Origins of Life and Evolution of Biosph*eres, **44**, 13-28.

Furukawa Y., Otake T., Ishiguro T., Nakazawa H. and Kakegawa T. (2012). Abiotic formation of valine peptides under conditions of high temperature and high pressure. *Origins of Life and Evolution of Biospheres,* **42**, 519-531.

Galvano F., Piva A., Ritieni A. and Galvano G. (2001). Dietary strategies to counteract the effects of mycotoxins: a review. *Journal of Food Protection*, **64**, 1, 120-131.

Gatta G.D. and Lee Y. (2006). On the elastic behaviour of zeolite mordenite: a synchrotron powder diffraction study. *Phys. Chem. Minerals*, **32**, 726-732.

Gatta G.D. and Lee Y. (2014). Zeolites at high pressure: A review. *Mineralogical Magazine*, **78**, 267-291.

Gatta G.D., Lotti P. and Tabacchi G. (2018). The effect of pressure on open-framework silicates: elastic behaviour and crystal-fluid interaction. *Phys. Chem. Minerals*, **45**(2), 115-138.

Georgieva V., Anfray C., Retoux R., Valtchev V., Valable S. and Mintova S. (2016). Iron loaded EMT nanosized zeolite with high affinity toward CO_2 and NO. *Microporous and mesoporous materials*, **232**, 256-263.

Georgieva V., Retoux R., Ruaux V., Valtchev V. and Mintova S. (2018). Detection of CO_2 and O_2 by iron loaded LTL zeolite films. *Frontiers of Chemical Science and Engineering*, **12**, 94−102.

Gilliams R.J. and Jia T.Z. (2018). Mineral surface-templated self-assembling systems: case studies from nanoscience and surface science towards origins of life research. *Life*, **8**, 10-29.

Gilson J.-P., Marie O., Mintova S., Valtchev V. (2011). Emerging Applications of Zeolites. In: Zeolites and ordered porous materials: fundamentals and applications (Martinéz C., Pérez-Pariente J. Eds) 3rd FEZA School book. 245-300.

Gottardi G. (1989). The genesis of zeolites. *European Journal of Mineralogy*, **1**, 479-487.

Gottardi G. and Galli E. (1985). Natural zeolites. Minerals and rocks series. Springer, Berlin (DE).

Grand J., Awala H. and Mintova S. (2016). Mechanism of zeolites crystal growth: new findings and open questions. *Cryst.Eng.Comm.*, **18**, 650-664.

Greco A., Maggini L., De Cola L., De Marco R. and Gentilucci L. (2015). Diagnostic implementation of fast and selective integrin-mediated adhesion of cancer cells on functionalized zeolite L monolayers. *Bioconjugate Chem*., **26**, 9, 1873-1878.

Grégoire B., Greenwell H.C., Fraser D.G. (2018). Peptide formation on layered mineral surfaces: The key role of brucite-like minerals on the enhanced formation of alanine dipeptides. *ACS Earth Space Chemistry*, **2**, 852-862.

Hamidi F., Bengueddach A., Di Renzo F. and Fajula F. (2003). Control of crystal size and morphology of mordenite. *Catalysis Letters,* **87**, 149-152.

Hay R.L. and Sheppard R.A. (2001). Occurrence of zeolites in sedimentary rocks: an overview. In: Natural zeolites: occurrence, properties, applications (Bish D.L., Ming D.W.). *Reviews in mineralogy and geochemistry,* **45**, 217-234.

Hazen R.M. (2005). Genesis: The scientific quest for life's origin. Book: Joseph Henry Press. Washington, DC.

Huang M., Lv S. and Zhou C. (2013). Thermal decomposition kinetics of glycine in nitrogen atmosphere. *Thermochimica Acta,* **552**, 60-64.

Jacobs P. A., van Cauwelaert F. H., Vansant E. F. and Uytterhoeven J. B. (1973). Surface probing of synthetic faujasites by adsorption of carbon dioxide. Part 1.-Infra-red study of carbon dioxide adsorbed on Na-Ca-Y and Na-Mg-Y zeolites. *Journal of the Chemical Society, Faraday Trans., 1,* **69**, 1056−1068.

Julbe A. and Drobek M. (2014). Zeolite X: Type. Springer-Verlag Berlin Heidelberg, *Encyclopedia of Membranes* (Drioli E. and Giorno L. eds).

Kalló D. (2001). Applications of natural zeolites in water and wastewater treatment. In: Natural zeolites: occurrence, properties, applications (Bish D.L., Ming D.W.). *Reviews in mineralogy and geochemistry,* **45**, 519-550.

Kato M., Itabashi K., Matsumoto A. and Tsutsumi K. (2003). Characteristics of MOR-framework zeolites synthesized in fluoride-containing media and related ordered distribution of Al atoms in the framework. *Journal of Physical Chemistry B,* **107**, 1788-1797.

Khodaverdi E., Honarmandi R., Alibolandi M., Baygi R.R., Hadizadeh F. and Zahuri G. (2014). Evaluation of synthetic zeolites as oral delivery vehicle for anti-inflammatory drugs. *Iranian journal of basic medical sciences*, **17**, 337-343.

Kim G.J. and Ahn W.S. (1991). Direct synthesis and characterization of high-SiO_2-content mordenites. *Zeolites*, **11**, 745-750.

Klotz S., Chervin J.-C., Munsch P. and Le Marchand G. (2009). Hydrostatic limits of 11 pressure transmitting media. *Journal of Physics D: Applied Physics*, **42**, 075413-075420.

Komaty S., Anfray C., Zaarour M., Awala H., Ruaux V., Valable S. and Mintova S. (2018). A facile route toward the increase of oxygen content in nanosized zeolite by insertion of cerium and fluorinated compounds. *Molecules,* **23**, 37−40.

Krohn J.E. and Tsapatsis M. (2006). Phenylalanine and arginine adsorption in zeolites X, Y, and β. *Langmuir,* **22**, 9350-9356.

Lambert J-F. (2008). Adsorption and polymerization of amino acids on mineral surfaces: A review. *Origins of Life and Evolution of Biospheres*, **38**, 211-242.

Larson A.C. and Von Dreele R.B. (1994). General structure analysis system “GSAS”; *Los Alamos national laboratory reports.* LAUR, 86-748.

Le Bail A. (2005). Whole powder pattern decomposition methods and applications: A retrospection. *Powder Diffraction,* **20**, 316-326.

Lee J.S., Kim J.H., Kim J.T., Suh, J.K., Lee J.M. and Lee C.H. (2002). Adsorption equilibria of CO_2 on zeolite 13X and zeolite X/activated carbon composite. *Journal of Chemical Engineering Data*, **47**, 1237-1242.

Lercher J.A. and Jentys A. (2002). Application of microporous solids as catalysts. In: Handbook of Porous Solids (Schuth F., Sing K.S.W. and J. Weitkamp, Eds). Wiley-VCH, Weinheim, vol. **2**, 1097-1155.

Liebau F. (1983). Zeolites and clathrasils – two distinct classes of framework silicates. *Zeolites*, **3**, 191-193.

Lu C., Bai H., Wu B., Su F. and Hwang J.F. (2008). Comparative study of CO_2 capture by carbon nanotubes, activated carbons, and zeolites. *Energy Fuels*, **22**, 3050-3056.

Lu L., Samarasekera C. and Yeow J.T.W. (2015). Creatinine adsorption capacity of electrospun polyacrylonitrile (PAN)-zeolite nanofiber membranes for potential artificial kidney applications. *Journal of applied polymer science*, **132,** 42418-42426.

Łukasik N. and Wagner-Wysiecka E. (2014). A review of amide bond formation in microwave organic synthesis. *Current Organic Synthesis*, **11**, 592-604.

Lülf H., Devaux A., Prasetyanto A., De Cola L., Torres T. and Bottari G. (2013). Porous nanomaterials for biomedical applications. *Wiley*, **22**, 487-507.

Mao H.K., Xu J. and Bell P.M. (1986). Calibration of the ruby pressure gauge to 800 kbar under quasi-hydrostatic conditions. *Journal of geophysical research*, **91**, 4673-4676.

Martra G., Deiana C., Sakhno Y., Barberis I., Fabbiani M., Pazzi M. and Vincenti M. (2014). The formation and self-assembly of long prebiotic oligomers produced by the condensation of unactivated amino acids on oxide surfaces. *Angewandte Chemie Internal Edition*, **53**, 4671-4674.

Martucci A., Cruciani G., Alberti A., Ritter C., Ciambelli P. and Rapacciuolo M. (2000). Location of Brønsted sites in D-mordenites by neutron powder diffraction. *Microporous and mesoporous materials*, **35-36**, 405-412.

Martucci A., Pasti L., Nassi M., Alberti A., Arletti A., Bagatin R., Vignola R. and Sticca R. (2012). Adsorption mechanism of 1,2-dichloroethane into an organophilic zeolite mordenite: a combined diffractometric and gas chromatographic study. *Microporous and mesoporous materials*, **151**, 358-367.

Martucci A., Sacerdoti M., Cruciani G., Dalconi C. (2003). In situ time resolved synchrotron powder diffraction study of mordenite. *European Journal of Mineralogy*, **15**, 485-493.

Maurin G., Llewellyn P.L. and Bell R.G. (2005). Adsorption mechanism of carbon dioxide in faujasites: grand canonical Monte Carlo simulations and microcalorimetry measurements. *Journal of Physical Chemistry B*, **109**, 33, 16084-16091.

Meier W.M. (1961). The crystal structure of mordenite (ptilolite). *Zeitschrift für Kristallographie,* **115**, 439-450.

Meier W.M., Olson D.H. (1978). Atlas of zeolite structure types. Structure commission of the international zeolite association.

Melchior M.T., Vaughan D.E.W. and Jacobson A. (1982). *Journal of American Chemical society,* **104**, 4859-4864.

Meteš A., Kovačević D., Vujević D. and Papić S. (2004). The role of zeolites in wastewater treatment of printing inks. *Water research,* **38**, 3373-3381.

Miller S.L. (1953). A production of amino acids under possible primitive Earth conditions. *Science*, **117**, 528-529.

Mintova S., Gilson J.-P. and Valtchev V. (2013). Advances in nanosized zeolites. *Nanoscale*, **5**, 6693-6703.

Mintova S., Jaber M. and Valtchev, V. (2015). Nanosized microporous crystals: emerging applications. *Chemical Society Reviews*, **44**, 7207-7233.

Mintova S., Grand. And Valtchev V. (2016). Nanosized zeolites: Quo Vadis? *Comptes Rendus Chimie*, **19**, 183-191.

Morris R.E. and Wheatley P.S. (2008). Gas storage in nanoporous materials. *Angewandte Chemie*, **47**, 4966-4981.

Mortier W.J. (1982). Compilation of extraframework sites in zeolites. *Butterworth Scientific Ldt.,* **54**.

Munsch S., Hartmann M. and Ernst S. (2001). Adsorption and separation of amino acids from aqueous solutions on zeolites. *Chemical Communications*, 1978-1979.

Ohara S., Kakegawa T. and Nakazawa H. (2007). Pressure effects on abiotic polymerization of glycine. *Origins of Life and Evolution of Biospheres*, **37**, 215-223.

Olson D. H. (1970). Reinvestigation of the crystal structure of the zeolite hydrated NaX. *Journal of Physical Chemistry*, **74**, 2758−2764.

Olson D.H. (1995). The crystal structure of dehydrated NaX. *Zeolites,* **15**, 439-443.

Osmanlioglu A.E. (2006). Treatment of radioactive liquid waste by sorption on natural zeolite in Turkey. *Journal of Hazardous Materials*, **B137**, 332-335.

Otake T., Taniguchi T., Furukawa Y., Kawamura F., Nakazawa H. and Kakegawa T. (2011). Stability of amino acids and their oligomerization under high-pressure conditions: implications for prebiotic chemistry. *Astrobiology*, **11**, 799-813.

Pabalan R.T. and Bertetti F.P. (2001). Cation-Exchange properties of natural zeolites. In: Natural zeolites: occurrence, properties, applications (Bish D.L., Ming D.W.). *Reviews in mineralogy and geochemistry*, **45**, 453-518.

Passaglia E. (1975). The crystal chemistry of mordenites. *Contributions to mineralogy and petrology*, **50**, 1, 65-77.

Passaglia E. and Sheppard R.A. (2001). The crystal chemistry of zeolites. In: Natural zeolites: occurrence, properties, applications (Bish D.L., Ming D.W.). *Reviews in mineralogy and geochemistry*, **45**, 69-116.

Pattabiraman V.R. and Bode J.B. (2011). Rethinking amide bond synthesis. *Nature*, **480**, 471-479.

Pécsi-Donáth É. (1968). Some contributions to the knowledge of zeolites. *Acta Mineralogica-Petrografica,* **18**, 127-141.

Plant D.F., Maurin G., Jobic H. and Llewellyn P.L. (2006). Molecular dynamics simulation of the cation motion upon adsorption of CO_2 in faujasite zeolite systems. *Journal of Physical Chemistry B*, **110**, 29, 14372-14378.

Platas-Iglesias C., Vander Elst L., Zhou W., Muller R.N., Geraldes C.F.G.C., Maschmeyer and Peters J.A. (2002). Zeolite GdNaY nanoparticles with very high relaxivity for application as contrast agents in magnetic resonance imaging. *Chemistry A European Journal,* 8, **22**, 5121-5131.

Polisi M., Grand J., Arletti R., Barrier N., Komaty S., Zaarour M., Mintova S., and Vezzalini G. (2019) CO_2 Adsorption/desorption in FAU zeolite nanocrystals: in situ synchrotron X-ray powder diffraction and in situ Fourier transform infrared spectroscopic study. *J. Phys. Chem. C,* **123**, 2361-2369.

Popyk A. and Eroshenko V. (2014). Current status and perspectives of thermomolecular engine developments. *International Journal of Thermodynamics,* **17**, 1, 33-41.

Pourshahrestani S., Zeimaran E., Djordjevic I., Kadri N. A. and. Towler M. R. (2016). Inorganic hemostats: The state-of-the-art and recent advances. *Materials Science and Engineering C,* **58**, 1255-1268.

Prescher C. and Prakapenka V.B. (2015). DIOPTAS: a program for reduction of two-dimensional X-ray diffraction data and data exploration. *High pressure research,* **35**, 223-230.

Proquitté H., Rüdiger M., Wauer R.R. and Schmalisch G. (2004). Measurements of evaporated perfluorocarbon during partial liquid ventilation by a zeolite absorber. *Artificial cells, blood substitutes, and biotechnology,* **32**, 3, 375-386.

Quartieri S., Arletti R., Vezzalini G., Di Renzo F. and Dmitriev V. (2012). Elastic behavior of MFI-type zeolites: 3 – compressibility of silicalite and mutinaite. *J. Solid State Chemistry,* **191**, 201-212.

Rajagopalan K., Peters A.W., Edwards G.C. (1986). Influence of zeolite particle size on selectivity during fluid catalytic cracking. *Applied catalysis,* **23**, 69-80.

Richard J., León Cid S., Rouquette J., van der Lee A., Bernard S. and Haines J. (2016). Pressure-induced insertion of ammonia borane in the siliceous zeolite, silicalite-1F. *J. Phys. Chem. C,* **120**, 9334–9340.

Rimola A., Ugliengo P. and Sodupe M. (2009). Formation versus hydrolysis of the peptide bond from a quantum-mechanical viewpoint: the role of mineral surfaces and implications for the origin of life. *International Journal of Molecular Sciences,* **10**, 746-760.

Rimoli M.G., Rabaioli M.R., Melisi D., Curcio A., Mondello S., Mirabelli R. and Abignete E. (2008). *Journal of biomedical materials research*, **87A**, 156-164.

Sakaguchi K., Matsui M. and Mizukami F. (2005). Applications of zeolite inorganic composites in biotechnology: current state and perspectives. *Applied Microbiology Biotechnology*, **67**, 306-311.

Sakhno Y., Battistella A., Mezzetti A., Jaber M., Georgelin T., Michot L. and Lambert J-F. (2019). One step up the ladder of prebiotic complexity: formation of nonrandom linear polypeptides from binary systems of amino acids on silica. *Chemistry A European Journal*, **25**, 1275-1285.

Santoro M., Gorelli F.A., Bini R., Haines J., Van der Lee A. (2013). High-pressure synthesis of a polyethylene/zeolite nano-composite material. *Nature Communications*, **4**, 1557-1562.

Santoro M., Scelta D., Dziubek K., Ceppatelli M., Gorelli F.A., Bini R., Garbarino G, Thibaud J-M., Di Renzo F., Cambon O., Hermet P., Rouquette J., van der Lee A., Haines J. (2016). Synthesis of 1D polymer/zeolite nanocomposites under high pressure. *Chem. Mater.*, **28**, 4065-4071.

Shanker U., Bhushan B., Bhattacharjee G. and Kamaluddin. (2012). Oligomerization of glycine and alanine catalyzed by iron oxides: Implications for prebiotic chemistry. *Origins of Life and Evolution of Biosph*eres, **42**, 31-45.

Simmonds P.G., Medley E.E., Ratcliff Jr. and Shulman G.P. (1972). Thermal decomposition of aliphatic monoamino-monocarboxylic acids. *Analytical chemistry*, **44**, 12, 2060-2066.

Simoncic P. and Armbruster T. (2004). Peculiarity and defect structure of the natural and synthetic zeolite mordenite: A single-crystal X-ray study. *American Mineralogist*, **89**, 421-431.

Sircar S., Myers A.L. (2003). Gas separation by zeolites. *Handbook of zeolite science and technology*, **22**.

Siriwardane R.V., Shen M.S. and Fisher E.P. (2005). Adsorption of CO_2 on zeolites at moderate temperatures. *Energy & Fuels*, **19**, 1153-1159.

Siriwardane R.V., Shen M.-S., Fisher E.P. and Poston J.A. (2001). Adsorption of CO_2 on molecular sieves and activated carbon. *Energy & Fuels*, **15**, 279-284.

Smith J.V. (1963). Structural classification of zeolites. *Mineral Soc. Am. Spec*., **1**, 281-290.

Smith J.V. (1984). Definition of a zeolite. *Zeolites*, **4**, 309-310.

Smith J.V. (1998). Biochemical evolution. I. Polymerization on internal, organophilic silica surfaces of dealuminated zeolites and feldspars. *Proceedings of the National Academy of Sciences of USA*, **95**, 3370-3375.

Smith J.V., Arnold F.P.Jr, Parsons I. and Lee M.R. (1999). Biochemical evolution III: Polymerization on organophilic silica-rich surfaces, crystal-chemical modeling, formation of first cells, and geological clues. *Proceedings of the National Academy of Sciences of USA*, **96**, 3479-3485.

Soldatkin O. O., Shelyakina M. K., Arkhypova V. N., Soy E., Kirdeciler S. K., Ozansoy Kasap B., Lagarde F., Jaffrezic-Renault N., Akata Kurç B., Soldatkin A. P. and Dzyadevych S. V. (2015). Nano- and microsized zeolites as a perspective material for potentiometric biosensors creation. *Nanoscale Res. Lett*., 10, 59.

Su H., Kim H.-S., Seo S.-M., Ko S.-O., Suh J.-M., Kim G.- H., Lim W.-T. (2012). Location of Na^+ ions in fully dehydrated Na^+-saturated zeolite Y (FAU, Si/Al = 1.56). *Bulletin of the Korean Chemical Society*, **33**, 2785−2788.

Sugahara H. and Mimura K. (2015). Peptide synthesis triggered by comet impacts: A possible method for peptide delivery to the early Earth and icy satellites. *Icarus*, **257**, 103-112.

Takaishi T., Kato M. and Itabashi K. (1995). Determination of the ordered distribution of aluminum atoms in a zeolitic framework. Part II. *Zeolites*, **15**, 21-32.

Thompson P., Cox D. E. and Hastings J. B. (1987). Rietveld refinement of Debye-Scherrer synchrotron X-Ray data from Al_2O_3. *Journal of Applied Crystallography*, **20**, 79−83.

Titus E., Kalkar A.K. and Gaikar V.G. (2003). Equilibrium studies of adsorption of amino acids on NaZSM-5 zeolite. *Colloids and Surfaces A*, 223, 55-61.

Toby B.H. (2001). EXPGUI, a graphical user interface for GSAS. *Journal of applied crystallography,* **34**, 210-213.

Toby B.H. (2006). R factors in Rietveld analysis: How good is good enough? *Powder diffraction,* **21**, 1, 67-70.

Townsend R.P. and Coker E.N. (2001). Ion exchange in zeolites. *Studies in surface science and catalysis,* **137**, 467-524.

Valeur E. and Bradley M. (2009). Amide bond formation: beyond the myth of coupling reagents. *Chemical Society Reviews,* **38**, 606-631.

Van Reeuwijk L.P. (1974). The thermal dehydration of natural zeolites (Wageningen H. and Zonen B.V., Eds).

Vermeiren W., Gilson J.-P. (2009). Impact of zeolites on the petroleum and petrochemical industry. *Top. Catal.,* **52**, 1131-1161.

Wang S. and Peng Y. (2010). Natural zeolites as effective adsorbents in water and wastewater treatment. *Chemical Engineering Journal,* **156**, 11-24.

Wheatley P.S., Butler A.R., Crane M.S., Fox S., Xiao B., Rossi A.G., Megson I.L., Morris R.E. (2006). NO-releasing zeolites and their antithrombotic properties. *J. Am. Chem. Soc.,* **128**, 502-509.

Wong-Ng W., Kaduk J.A., Huang Q., Espinal L., Li L., Burress J.W. (2013). Investigation of NaY Zeolite with adsorbed CO_2 by neutron powder diffraction. *Microporous and Mesoporous Matererials,* **172**, 95-104.

Yang H., Xu Z., Fan M., Gupta R., Slimane R.B., Bland A.E. and Wright I. (2008). Progress in carbon dioxide separation and capture: a review. *Journal of Environmental Sciences*, **20**, 14-27.

Young R.A. (1993). The Rietveld method. IUCr Monographs on Crystallography 5. *Oxford University Press.*

Yu Y., Xiong G., Li C. and Xiao F.-S. (2001). Characterization of aluminosilicate zeolites by UV Raman spectroscopy. *Microporous and Mesoporous Materials*, **46**, 23-34.

Zhai Q.-Z., Qiu S., Xiao F.-S., Zhang Z.-T., Shao C.-L. and Han Y. (2000). Preparation, characterization, and optical properties of the host-guest nanocomposite material zeolite-silver iodide. *Materials Research Bulletin*, **35**, 59-73.

Zukal A., Mayerová J. and Kubu M. (2010). Adsorption of carbon dioxide on high-silica zeolites with different framework topology. *Topics in Catalysis*, **53**, 1361-1366.